MECHANICAL BEHAVIOR OF GAS METAL ARC WELDS AND LITHIUM-ION BATTERY MODULE SPECIMENS

by

Catherine M. Amodeo

A dissertation submitted in partial fulfillment
of the requirements for the degree of
Doctor of Philosophy
(Mechanical Engineering)
in the University of Michigan
2015

Doctoral Committee:

Professor Jwo Pan, Chair
Professor Elijah Kannatey-Asibu
Professor Wei Lu
Professor Jason McCormick

Dedication

To my family, friends, and colleagues who have supported and encouraged me throughout this process.

Acknowledgements

I would like to express my sincere appreciation and gratitude to my advisor Professor Jwo Pan for his guidance, encouragement, support and unlimited patience throughout this research work. His intellectual support at various stages of this work has been invaluable in enabling me to carry this work to completion. I would like to thank my doctoral committee Professor Elijah Kannatey-Asibu, Professor Wei Lu, and Professor Jason McCormick for their guidance and valuable suggestions. I also thank the academic support staff at the Department of Mechanical Engineering for their invaluable assistance at various stages.

I am very grateful to Professor Jwo Pan's research group, especially Dr. Jaewon Lee, Dr. William Lai, and Dr. Md Yusuf Ali. Dr. Jaewon Lee's research on the modeling of failure modes of laser welds in which he adopted the Gurson model to simulate the necking/shear failure of the load carrying sheets under tensile dominant loading conditions provided valuable background without which chapter 2 may not have been possible. I would like to thank Dr. William Lai for his work in examining the grain structures near the fracture surfaces of the gas metal arc weld specimens and for providing optical microscope images of the fracture surfaces for chapter 2. Also, chapter 4 would not have been possible without the experimental results provided from Dr. Lai's research. The helpful discussions with Dr. Md Yusuf Ali regarding chapter 4 are very much appreciated. I also express my thanks and well wishes to Dr. Van-Xuan Tran, Dr.

Kamran Asim, Dr. Kulthilda Sripichai, Dr. Teresa Franklin, Seung Hoon Hong, Katherine Avery, Nikhil Kotasthane, and Shin-Jang Sung.

I would like to express my special thanks and gratitude to W. Randy Tighe, Director Product Engineering and J. David Kotre, Chief Engineer of Johnson Controls who encouraged me to persist through to the completion of my degree. Their encouragement and generous support throughout this process was above and beyond their duties and are very much appreciated. I would also like to thank Mark Harris, Principal Engineer of Johnson Controls for his help in performing the experiments for chapter 2. I am very grateful to Johnson Controls for providing financial support to complete the academic and research work.

Finally, I would like to thank my family and friends for all of their support and encouragement which has made this dissertation possible.

Table of Contents

List of Figures

List of Tables

Chapter 1
Introduction

This dissertation consists of two parts. The first part is related to a study of the failure mechanisms of gas metal arc welds. Chapters 2 and 3 constitute the first part of the dissertation. The second part of the dissertation is related to the development of a computational model for simulations of representative volume element (RVE) specimens of lithium-ion battery modules under in-plane constrained compression. Chapter 4 constitutes the second part of the dissertation. All of the chapters were prepared as independent papers.

1.1. Part 1: Failure of gas metal arc welds in lap-shear specimens

For the automotive industry, the performance of discontinuous gas metal arc welded joints is of significant interest. By minimizing the length of the discontinuous welds, significant cost savings can be gained due to reduced cycle time and reduced usage of equipment and consumables. However, improperly sized welds can result in the loss of structural integrity near the welds in service.

In chapter 2, the failure modes of gas metal arc welds in single lap-shear specimens of high strength low alloy (HSLA) steel are investigated. The effects of weld geometries and the mechanical properties of discontinuous gas metal arc welded joints of

HSLA340 steel on the failure modes of notched lap-shear specimens are investigated under quasi-static loading conditions. For lack of further information, the residual stresses due to the welding process are not considered in this investigation. Notched lap-shear specimens were cut from the middle portions of the wide lap-shear specimens of various weld lengths. Quasi-static tests were conducted in order to determine the failure modes of the welds. Three-dimensional finite element analyses were also conducted with consideration of micro void nucleation and growth. The locations of the higher void volume fractions from the finite element analyses are compared to the failure locations observed in experiments. Further finite element analyses were conducted in order to understand the effects of the weld geometry and the mechanical properties of the weld on the load-displacement responses and the predicted failure locations of the lap-shear joints. Finally, conclusions are made.

In chapter 3, the mode I and mode II stress intensity factor solutions for the pre-existing cracks near gas metal arc welds in lap-shear specimens are investigated by the analytical stress intensity factor solutions and by finite element analyses. Analytical stress intensity factor solutions for the welds in lap-shear specimens with idealized weld geometries were derived based on the beam bending theory. Two-dimensional, plane strain finite element analyses were carried out in order to obtain the computational stress intensity factor solutions for the realistic and idealized weld geometries. The computational solutions are compared with the analytical solutions based on the beam bending theory. Further finite element analyses were carried out in order to obtain the computational stress intensity factor solutions for the realistic weld geometries with dissimilar sheet thicknesses. In addition, the distribution of the stress intensity factor

solutions for continuous idealized welds and discontinuous idealized welds were obtained by three-dimensional finite element analyses. Finally, some conclusions are made.

1.2. Part 2: Development of a computational model for simulations of representative volume element specimens of lithium-ion battery modules

Lithium-ion batteries have been considered as the solution for electric vehicles for the automotive industry due to their lightweight and high energy density. For automotive applications, an understanding of the mechanical performance of lithium-ion batteries is of great importance for crashworthiness analyses. Computational models are important tools for the efficient and cost-effective design of battery cells and modules.

In chapter 4, a computational model is developed for simulations of representative volume element (RVE) specimens of lithium-ion battery modules under in-plane constrained compression tests. The computational results from the model under quasi-static and dynamic loading conditions are compared to those from experiments. An additional finite element analysis is performed in order to validate the results of the model under quasi-static loading using the explicit solver. A further finite element analysis is performed in order to investigate whether the computational time of the model under dynamic loading conditions could be reduced further. Lastly, a finite element analysis is performed in order to determine if the increase in the nominal stress at which buckling begins in the heat dissipater under the dynamic loading conditions is due to the different buckling modes observed in the results of the finite element analyses of module

RVE specimens under quasi-static loading conditions and under dynamic loading conditions. Finally some conclusions are made.

Chapter 2
Failure Modes of Gas Metal Arc Welds in Lap-Shear Specimens of High Strength Low Alloy (HSLA) Steel

2.1. Introduction

Recently, many investigations on the strength of gas metal arc welded joints have been conducted. Investigators have reported failure locations near weld roots and near weld toes under quasi-static and cyclic loading conditions. For example, Yan et al. [1] conducted experiments to examine the performance of gas metal arc weld joints under quasi-static and cyclic loading conditions. Experiments were performed on single lap-shear and double lap-shear specimens of HSLA350, DP600, DP965, M900, and M1300. Most non-martensitic specimens tested under quasi-static loading conditions failed near the weld root while most martensitic specimens failed near the weld toe. The failure mode of the non-martensitic specimens under cyclic loading conditions was mainly near the weld toe under low load levels but mainly near the weld root under higher load levels. The failure mode of the martensitic specimens under cyclic loading conditions was mainly near the weld toe under low load levels but the specimens exhibited both failure modes under high load cyclic loading conditions. Feng et al. [2] investigated the influence of HAZ softening on the quasi-static and fatigue performance of HSLA590, DP, martensitic, and boron steels in single lap-shear specimens. The failure mode under quasi-static loading conditions was observed near the weld root. Both failure modes,

near the weld root and near the weld toe, were observed in the specimens under cyclic loading conditions. Joaquin et al. [3,4] studied single lap-shear joints between coated and uncoated mild steel and DP600 sheets under quasi-static and cyclic loading conditions. Failure under quasi-static loading conditions was observed mainly near the weld root whereas under cyclic loading conditions failure was observed near the weld toe and near the weld root.

Koganti et al. [5] investigated the effects of different material configurations on the fatigue and quasi-static strength of single lap-shear joints of DP600 and boron steels. The failure mode under quasi-static loading conditions was observed near the weld toe when the bottom sheet was the DP600 steel sheet and near the weld root when the top sheet was the DP600 steel sheet. The failure mode under cyclic loading conditions was observed near the weld toe when the bottom sheet was the boron steel sheet and near the weld root when the top sheet was the boron steel sheet. Koganti et al. [6] studied DP780 single lap-shear joints under quasi-static and cyclic loading conditions. Their results indicated that the weld geometry did not affect the quasi-static strength of the joints but played an important role in the high-cycle fatigue life and the failure locations of the joints. Angotti et al. [7] studied DP780 coach peel joints under quasi-static and cyclic loading conditions. Their results showed that the weld power setting and the gap between the top and bottom sheets affected the quasi-static strength and the fatigue life of the joints. Kapustka et al. [8] investigated the effects of manufacturing variations on the quasi-static and dynamic strengths of DP780, DP980, and TRIP780 single lap-shear and butt weld joints. They reported the failure of the lap-shear specimens near the weld root. Bonnen et al. [9] examined the fatigue lives of SAE1008, HSLA420, DP590, DP600,

DP780, TRIP780, boron, and DQSK steels using single lap-shear, double lap-shear, start-stop, butt weld, and perch mount specimens. The failure modes of the lap-shear specimens under quasi-static loading conditions were mainly near the weld toe. The failures observed in the double lap-shear specimens under cyclic loading conditions were near the weld toe. The failure mode of the single lap-shear specimens under cyclic loading conditions was near the weld toe under low load levels but near the weld root under higher load levels. In certain cases, under quasi-static and cyclic loading conditions, the lap-shear specimens failed in the base metal, away from the weld region. The main fracture locations observed in recent investigations of lap-shear specimens under quasi-static and dynamic loading conditions and under cyclic loading conditions are summarized in Tables 2.1 and 2.2, respectively.

For the automotive industry, the performance of discontinuous gas metal arc welded joints is of significant interest. By minimizing the length of the discontinuous welds, significant cost savings can be gained due to reduced cycle time and reduced usage of equipment and consumables. However, improperly sized welds can result in the loss of structural integrity near the welds in service. In order to examine the weld strengths of the discontinuous welds, wide lap-shear specimens of HSLA340 steel sheets with various weld lengths were made. The specimens have a width of 60 mm, thicknesses of 1.5 mm, 2.0 mm, and 2.5 mm and weld lengths of 10 mm to 40 mm. Some of these specimens are shown in Figure 2.1(a). Quasi-static tests of the wide lap-shear specimens were carried out under displacement controlled conditions. The normalized weld strengths (per weld length) for specimens of various thicknesses are plotted in Figure 2.1(b). The figure shows an increase in the normalized weld strength in

general as the weld length decreases. However, the reason for the effect of the length of the discontinuous welds on the weld strength is not clear. In this investigation, as the first step, the end effects of the discontinuous welds are excluded and the failure at the mid-sections of the welds is studied.

In this chapter, the effects of weld geometries and the mechanical properties of discontinuous gas metal arc welded joints of HSLA340 steel on the failure modes of notched lap-shear specimens are investigated under quasi-static loading conditions. For lack of further information, the residual stresses due to the welding process are not considered in this investigation. Notched lap-shear specimens were cut from the middle portions of the wide lap-shear specimens of various weld lengths. Quasi-static tests were conducted in order to determine the failure modes of the welds. Three-dimensional finite element analyses were also conducted with consideration of micro void nucleation and growth. The locations of the higher void volume fractions from the finite element analyses are compared to the failure locations observed in experiments. Further finite element analyses were conducted in order to understand the effects of the weld geometry and the mechanical properties of the weld on the load-displacement responses and the predicted failure locations of the lap-shear joints.

2.2. Experiments

2.2.1. Un-notched lap-shear specimens

In this investigation, lap-shear specimens of HSLA steel sheets with a thickness of 2.0 mm were robot welded together using the gas metal arc weld process. A filler

metal of ER70S-6 with 0.035 inch wire diameter was used. The short circuit metal transfer mode was used with 75% argon and 25% carbon dioxide shielding gas. The weld travel speed was 55 cm/min and the power settings were 125 A and 22.5 V. No heat treatment was carried out after the welding process. The grade of the steel sheets was SAE J2340 340XF. The Type X in the material specification refers to HSLA steels. The Sub Type F in the material specification denotes that the steel is sulfide inclusion controlled. This specification is used for steels which will be used in unexposed applications and which will undergo forming operations [10]. The chemical composition of the steel sheets was measured using spectrochemical analysis. This test was conducted using a Leco SA-2000 Surface Analyzer. The chemical composition is given in Table 2.3.

60 mm wide sheet specimens with the weld lengths varying from 10 mm to 40 mm were made as shown in Figure 2.1. Un-notched lap-shear specimens were then machined from the middle portions of the wide welded specimens using a CNC milling machine. Figure 2.2(a) shows a schematic of an un-notched lap-shear specimen. The weld zone is schematically indicated as the shaded area in the figure. The weld root and weld toe are labeled in the figure. As shown in the figure, the specimen has a width w of 15 mm and a length l of 30 mm. The specimen has a thickness t of 2.0 mm. Two doublers were used for aligning the load application through the center of the specimen. The loading direction is indicated by two bold arrows on the right and left sides of the specimen.

2.2.2. Quasi-static test of the un-notched lap-shear specimens

Quasi-static tests of the un-notched lap-shear specimens were carried out under displacement controlled conditions. These tests were conducted using an Instron testing machine at a constant cross-head speed of 25 mm/min. Three specimens, cut from welded sheets with the weld lengths of 30 mm, 35 mm, and 40 mm, were tested. An extensometer, with an initial gauge length of 2 inches, was used to measure the change in length of each specimen. The extensometer was centered on the test specimen. As referring to Figure 2.2(a), the right end of the bottom sheet of the lap-shear specimen was trimmed in order to avoid interference with the extensometer. Doublers were included within the grips to align the load application through the interfacial plane of the two sheets of the specimen. The failure location of an un-notched specimen cut from a wide specimen with the weld length of 35 mm is shown in Figure 2.3. The failure occurred in the base metal, away from the weld region. The necking/shear failure mechanism of the base metal sheet occurred before the failure near the weld could take place due to the higher yield strengths of the weld metal and the heat affected zone.

2.2.3. Notched lap-shear specimens

In order to investigate the failure mechanism in the vicinity of the welds, and to avoid the failure of the specimen due to the necking of the specimen sheets far away from the welds, notched specimens were machined from the middle portions of the wide welded specimens using a CNC milling machine. Figure 2.2(b) shows a schematic of a notched lap-shear specimen. The weld zone is schematically indicated as the shaded area

in the figure. The weld root and weld toe are labeled in the figure. As shown in the figure, the specimen has a width w of 15 mm outside of the central portion. The specimen has a length c of 13 mm for the central notched portion and a length d of 25 mm outside of the notch portion. The specimen has a minimum width b of 6 mm at the center of the notch. The radius of the notch is 7 mm. The specimen has a thickness t of 2.0 mm. Two doublers were used for aligning the load application through the interfacial plane of the two sheets of the specimen. The loading direction is indicated by two bold arrows on the right and left sides of the specimen. Figure 2.4 shows a close-up view near the weld in a notched lap-shear specimen.

2.2.4. Quasi-static tests of notched lap-shear specimens

Quasi-static tests of the notched lap-shear specimens were carried out under displacement controlled conditions. These tests were conducted using an Instron testing machine at a constant cross-head speed of 25 mm/min. The test set up is shown in Figure 2.5. Seven specimens, cut from wide lap-shear specimens of different weld lengths, were tested. An extensometer, with an initial gauge length of 2 inches, was used to measure the change in length of each specimen. The extensometer was centered on the test specimen. As referring to Figure 2.5, the top end of the left sheet of the lap-shear specimen was trimmed in order to avoid interference with the extensometer. Doublers were included within the grips to align the load through the interfacial plane of the two sheets of the specimen.

Test results are summarized in Table 2.4. The specimens are labeled with a specimen number followed by the length of the discontinuous weld on the wide lap shear specimen from which the notched specimen was cut. The welded specimens exhibited two competing failure locations. The specimens machined from wide lap-shear specimens with shorter weld lengths failed near the weld root. Figure 2.6(a) shows a side view of the failed specimen S1-10 near the failure location. The specimens machined from wide lap-shear specimens with longer weld lengths failed near the weld toe. Figure 2.6(b) shows a side view of the failed specimen S5-30 near the failure location. The necking failure mode can be observed at both failure locations. The average maximum loads obtained from the specimens that failed near the weld root and from those that failed near the weld toe were 8.36 kN and 8.29 kN, respectively.

2.2.5. Failure mechanism of notched lap-shear specimens

In order to study the failure modes in the failed specimens, the failure surfaces of the separated sheets were examined under a scanning electron microscope. A scanning electron micrograph of the failure surface from specimen S2-15 is shown in Figure 2.7. The micrograph was taken of the failure surface on the separated sheet side on the right of the specimen, as similarly shown for the failed specimen S1-10 in Figure 2.6(a). Two micrographs showing close-up views of the failure surface are also shown in the figure. The micrographs show dimpled fracture surfaces due to micro void nucleation and growth.

A scanning electron micrograph of the failure surface from specimen S6-30 is shown in Figure 2.8. The micrograph was taken of the failure surface on the separated sheet side on the left of the specimen, as similarly shown for the failed specimen S5-30 in Figure 2.6(b). Two micrographs showing close-up views of the failure surface are also shown in the figure. Again, the micrographs show dimpled fracture surfaces due to micro void nucleation and growth. The dimples on both fracture surfaces are elongated in shape, characteristic of ductile fracture resulting from shear loading [11,12].

As shown in the close-up views, the failure surface of specimen S6-30 exhibits a larger number of dimples per unit area when compared to that of the fracture surface from the specimen S2-15. The larger number of dimples suggests that the failure of specimen S6-30, which failed near the weld toe, was more ductile when compared to the failure of specimen S2-15, which failed near the weld root [13,14]. The grain structures near the fracture surfaces were examined under an optical microscope in order to understand the difference in ductility exhibited by the failure surfaces. It is concluded that the failure path of specimen S2-15 includes the heat affected zone while the failure path for specimen S6-30 is through the base metal.

2.2.6. Weld geometry and micro-hardness of welded joints

The variation of the cross sectional geometry was studied at the mid-section of the weld. Micrographs of the cross sections of seven weld specimens with weld lengths of 10 mm, 15 mm, 20 mm, 25 mm, 30 mm, 35 mm, and 40 mm are shown in Figures 2.9(a)

through (g). The variation of the shape of the weld nugget, the penetration into the bottom sheet, and the gap between the top and bottom sheets are shown.

Micro-hardness tests were carried out in order to understand the Vickers hardness values in the weld region for specimens with short and long welds. Three specimens with different weld lengths were sectioned at the mid-sections of the welds. The specimens were cross sectioned, mounted, polished, and lightly etched to better visualize the heat affected zone and base metal boundaries. 2% nital solution was used as the etchant. Micro-hardness indentations were made with a 500 grams load and the indentations were carried out at an interval of about 350 μm. Results of the micro-hardness tests are shown in Figure 2.10(a). The figure shows that the hardness in the heat affected zone and the weld metal becomes higher as the weld length becomes smaller. The figure also shows the trend in the size of the heat affected zone. The heat affected zone in the 10 mm weld extends past the toe of the weld as labeled A in the figure. The heat affected zone in the 40 mm weld does not reach the toe of the weld as labeled B in the figure. These trends in hardness and heat affected zone size were examined on two additional specimens, a 10 mm weld specimen and a 40 mm weld specimen. For these two additional specimens, micro-hardness indentations were carried out at an interval of about 200 μm. As shown in Figure 2.10 (b), the specimens exhibit similar results. The 10 mm weld specimen has a higher hardness in the heat affected zone and the weld metal and, unlike the 40 mm weld specimen, the heat affected zone extends past the toe of the weld.

2.3. Finite element model

2.3.1. Finite element method

Finite element analyses, based on the initial weld geometries, were carried out in this study in order to identify the influences of the weld geometry as well as the plastic behavior near the weld on the failure modes of the welds in lap-shear specimens. Since the notched specimens are used to study the failure mechanism in the vicinity of the welds, three-dimensional finite element models were developed. Figure 2.11 shows a top view and a side view of a finite element model of a notched lap-shear specimen where the dark shaded region represents the weld metal. The Cartesian coordinate system is also shown in the figure. As shown in the figure, the left end of the model at X = 0 and Y = 0 is fixed and the displacement of the right end of the model at Y = 0 is applied in the X direction. In order to reduce the computational time, only a half of the specimen is modeled with the symmetry conditions applied at the mid-section of the weld at Z = 0. Second-order, continuum, hexahedral elements (C3D20) are used in the models. The element size near the weld is about 150 μm. Computations were performed using the commercial finite element code ABAQUS Standard v6.11 [15, 16, 17].

In order to identify the plastic behavior near and in short welds and long welds, two finite element models were developed. The size and cross sectional shape of the weld metal and the size and shape of the heat affected zones were designed to match the micrographs of the cross sections for the 10 mm weld and the 40 mm weld shown in Figure 2.10(a). The location of the notch along the length of the specimen, in the X direction, was centered near the geometric center of the weld metal.

The base metal, the heat affected zone, and the weld metal can be identified based on their distinct grain structures and corresponding micro-hardness values. Figure 2.12 shows an optical micrograph of the etched cross section of a 10 mm weld specimen. Based on the grain structures and the micro-hardness measurements shown in Figure 2.10(a), the heat affected zone is sectioned into three distinct zones marked as HAZ 1, HAZ 2, and HAZ 3 in the figure. Figure 2.13 shows an optical micrograph of the etched cross section of a 40 mm weld specimen. Based on the grain structures and the micro-hardness measurements shown in Figure 2.10(a), the heat affected zone is sectioned into two distinct zones marked as HAZ 1 and HAZ 2 in the figure. The finite element meshes near the weld for the short weld model, based on the micrograph shown in Figure 2.12, and for the long weld model, based on the micrograph shown in Figure 2.13, are shown in Figures 2.14(a) and 2.14(b) with the different material sections, respectively.

2.3.2. Material stress-strain curves

In order to obtain the stress-strain behavior of the base metal for use in the finite element models, tensile tests were performed according to the ASTM standard for a rectangular, subsized specimen [18]. Three representative sheet specimens were tested. The HSLA sheets were cut into 100 mm long dog bone specimens. The reduced section of each specimen had a gauge length of 30 mm and a width of 6 mm. The dog bone profile was machined using a CNC milling machine. The tests were carried out using an automated Instron tensile testing machine. An extensometer with a one inch gauge length was used to automatically record the extension in the uniform gauge section. The cross-

head speed was maintained at 12.7 mm/min throughout the tests. The engineering stress-strain curves for the base metal from the three representative sheet specimens are shown in Figure 2.15.

A finite element model replicating the tensile tests was developed using the same element type and mesh density as described above for the lap-shear specimens. Figure 2.16 shows the finite element model of the tensile specimen under a tensile test. The Cartesian coordinate system is also shown in the figure. As shown in the figure, the bottom end of the model is fixed and the displacement of the top end of the model is applied in the Y direction. The finite element analysis of the tensile test was used to verify the material properties of the base metal prior to running the finite element analyses of the welded specimens.

The initial part of the tensile stress-strain curve of the base metal in the finite element models is modeled as elastic with the elastic modulus E. When the stress is larger than the initial yield stress σ_0, the tensile true stress-strain curve of the base metal is fitted to the experimental tensile true stress-strain curve up to the true stress corresponding to the ultimate stress. When the nominal stress is larger than the ultimate stress, the tensile true stress-strain curve is fitted by a power-law relation as

$$\sigma = K\varepsilon^n \tag{2.1}$$

where σ represents the true stress, ε is the true strain, K represents the strength coefficient and n represents the hardening exponent. For the base metal, σ_0 and E are determined as 368 MPa and 207 GPa, respectively, from the experimental data. Here, K and n are determined as 800 MPa and 0.21, respectively, to fit to the experimental

stress-strain curves. Figure 2.15 shows the engineering stress-strain curves for the base metal from three representative sheet specimens and the resulting curve from the finite element analysis.

Since it is difficult to determine the tensile stress-plastic strain curves of the weld metal and the heat affected zones, the tensile stress-plastic strain curves for the weld metal and the heat affected zones have been estimated by scaling the tensile stress of the base metal proportional to the corresponding hardness values measured by the indentation tests for a given plastic strain [19]. The values of the Vickers hardness and the scaled initial yield stress are listed in Table 2.5(a) for the short weld model and Table 2.5(b) for the long weld model. Figures 2.17(a) and 2.17(b) show the tensile stresses as functions of the plastic strain for the base metal, the heat affected zones and the weld metal used in the short weld and long weld finite element models, respectively. These tensile stress-plastic strain curves were used as the effective stress-plastic strain curves in the finite element analyses. The residual stresses due to the welding process are not accounted for in the models.

2.3.3. Gurson's yield function

Since the experimental results indicate that the failure of the welds is of a ductile nature, the finite element analyses were carried out with consideration of void nucleation and growth. Gurson [20] developed a yield function for porous materials, based on the experimental data in Gurland [21], where the matrices are modeled by the Mises yield function, to account for the loss of stress carrying capacity due to microvoid nucleation

and growth. It should be noted that the Gurson model [20] was adopted to simulate the necking/shear failure of the load carrying sheets near laser welds in lap-shear specimens of HSLA steel [19]. The load carrying sheets near the laser welds in lap-shear specimens of Lee et al. [19] and the gas metal arc welds in our lap-shear specimens are both under tensile dominant loading conditions.

The Gurson yield function Φ is expressed as [20,22].

$$\Phi = \left(\frac{\Sigma_e}{\sigma_M} \right)^2 + 2q_1 f \cosh\left(q_2 \frac{3\Sigma_m}{2\sigma_M} \right) - 1 - q_3 f^2 = 0 \tag{2.2}$$

where Σ_e is the macroscopic tensile effective stress based on the Mises yield function, Σ_m is the macroscopic mean stress, σ_M is the matrix flow stress, and f is the void volume fraction. Here, q_1, q_2 and q_3 are the fitting parameters which were introduced by Tvergaard [23]. In this investigation the values of q_1=1.5, q_2=1.0 and q_3=2.25 are taken in the finite element analyses.

The increase of void volume fraction arises from the nucleation of new voids and from the growth of the existing voids. For the increase rate of void volume fraction due to nucleation, we adopt the plastic strain controlled nucleation model suggested by Chu and Needleman [24]. The increase rate of void volume fraction due to growth can be obtained from the plastic incompressibility of the matrix material. Thus the increase rate of void volume fraction can be expressed as

$$\dot{f} = \dot{f}_{nucleation} + \dot{f}_{growth} = A\dot{\varepsilon}_M^p + (1-f)\dot{\eta}_{.k}^{k\,p} \tag{2.3}$$

where the first term on the right-hand side of the equation represents the plastic strain controlled void nucleation rate and the second term represents the void growth rate.

Here, $\dot{\varepsilon}_M^p$ is the matrix equivalent plastic strain rate, $\dot{\eta}_{.k}^{k\,p}$ represents the macroscopic dilatational plastic strain rate, and A is expressed as

$$A = \frac{f_N}{s\sqrt{2\pi}} \exp\left[-\frac{1}{2}\left(\frac{\varepsilon_M^p - \varepsilon_N}{s} \right)^2 \right] \text{ for } \dot{\varepsilon}_M^p > 0 . \tag{2.4}$$

Here, f_N is the volume fraction of void nucleating particles for the plastic strain controlled nucleation model, s is the standard deviation, and ε_N is the mean value of the normal distribution for the plastic strain controlled nucleation model.

A modification to the Gurson model to account for final material failure at a realistic value of the void volume fraction has been proposed by Tvergaard and Needleman [22]. In their investigation the void volume fraction for void coalescence is taken as 0.15 and the void volume fraction at final fracture is taken as 0.25. Although the modification has not been included in the finite element analyses in this study, the results of the finite element analyses are interpreted at an assumed critical void volume fraction of 0.22.

Without experimental data available for this HSLA steel, several analyses were run to determine the void nucleation parameters that result in realistic values of void volume fraction near the peak load for both the long weld and short weld models. Both models were run with the void nucleation parameter f_N varying between 0.002 and 0.3, ε_N varying between 0.3 and 0.5, and s varying between 0.1 and 0.15. In the computational results described in this study the void nucleation parameters f_N = 0.002, ε_N = 0.3, and s = 0.15 are assumed for all the material elements in the base metal, heat

affected zone, and weld metal in order to obtain some qualitative results on the void volume fraction distribution. The initial void volume fraction is taken to be zero and the tensile stress-strain curves for the different zones of the model are used as the matrix tensile stress-strain curves.

2.4. Results of the finite element analyses

2.4.1. Load-displacement response

In the following, the load-displacement responses of the tested notched lap-shear specimens are compared to those of the finite element analyses with and without the consideration of void nucleation and growth. The load-displacement curves obtained from the finite element analyses for the short weld model (10 mm weld) and the long weld model (40 mm weld) are plotted in Figures 2.18(a) and 2.18(b), respectively, with the experimental results. The initial response of the specimens from the finite element analyses with and without consideration of void nucleation and growth are equivalent. The results of the finite element analyses with consideration of void nucleation and growth exhibit softer behavior at large displacements where voids begin to nucleate and grow. In Figure 2.18(a), the experimental results for specimens S1-10, S2-15, and S3-20 are also plotted. In general, the results of the finite element analysis for the short weld model agree with the experimental results. In Figure 2.18(b), the experimental results for specimens S4-20, S5-30, S6-30, and S7-40 are also plotted. In general, the results of the finite element analysis for the long weld model agree with the experimental results. It should be mentioned that the sizes and shapes of the weld metal and the heat affected

zone can vary for a given weld length as shown in Figures 2.9 and 2.10 for the 10 mm, 25 mm and 40 mm welds. The variations can contribute to the scatter of the load-displacement curves when the results from the finite element analyses and experiments are compared.

A change in slope is evident in the plots at a displacement of about 0.06 mm for both the short weld and the long weld analyses. The displacement at which the change in slope occurs is corresponding to the displacement at which bending begins near the weld toe of the bottom sheet. The bending of the bottom sheet and the applied load are plotted as functions of the displacement in Figure 2.19(a). A method of quantifying the rotation of the bottom sheet is shown in Figure 2.19(b). The angle due to the displacement of the surface element near the weld toe is measured with respect to the top surface of the lower sheet along the X-Z plane where the displacement is fixed as shown in Figure 2.11(a).

2.4.2. Failure prediction

The failure modes of the lap-shear specimens are investigated by the finite element analyses with consideration of void nucleation and growth in all zones. The equivalent plastic strain distributions near the weld for the short weld model are shown in Figures 2.20(a) and 2.20(c). The maximum values in the scale bars in the figures were chosen in order to highlight the areas of the highest equivalent plastic strain. Figure 2.20(a) shows the equivalent plastic strain distribution at the mid-section of the specimen. The figure shows high equivalent plastic strains near the weld root in the middle portion of the upper sheet. An optical micrograph of the cross section near the weld of a failed

15 mm specimen is shown in Figure 2.20(b). Figure 2.20(b) shows that the shear direction of the failed specimen is consistent with the high shear strains shown in Figure 2.20(a). Figure 2.20(c) shows the equivalent plastic strain distribution near the weld on the top and outside surfaces of the specimen. This figure shows the location of the maximum equivalent plastic strain on the top and outside surfaces of the specimen near the notch surface in the heat affected zone near the boundary of the weld metal.

The distributions of the void volume fraction near the weld for the short weld model at the mid-section of the specimen and on the top and outside surfaces of the specimen are shown in Figures 2.21(a) and 2.21(b), respectively. The maximum values in the scale bars in the figures were chosen in order to highlight the areas of the highest void volume fraction. Figure 2.21(a) shows that the highest void volume fraction of 0.22 occurs in an element in the base metal near the boundary of the heat affected zone. The highest void volume fraction is near the middle portion of the upper sheet at the mid-section of the specimen where the hydrostatic stresses are the largest. This suggests that the initiation of ductile fracture due to void nucleation and growth should be observed near this location in the failed specimens. It is noted that this location differs from the location of the maximum equivalent plastic strain shown in Figure 2.20(c). Figure 2.21(b) shows material elements with large void volume fractions are also located near the location of high equivalent plastic strain. The void volume fraction in this area is as high as 0.17. Figure 2.21(b) also shows material elements with large void volume fractions near the weld toe. The location of the maximum void volume fraction is initially near the weld toe. As the displacement increases, and passes the displacement where the maximum load occurs, the location of maximum void volume fraction is near

the weld root. This change occurs at a void volume fraction of 0.20. Figure 2.6(a) and Figure 2.20(b) show a failed specimen and the cross section near the weld from specimens that were machined from wide lap-shear specimens with shorter weld lengths. These figures show that the failures occur near the weld root. The ductile necking failure mode exhibited by the failed specimens is also apparent at the location of the maximum void volume fraction in Figure 2.21(a).

The equivalent plastic strain distributions near the weld for the long weld model at the mid-section and on the top and outside surfaces of the specimen are shown in Figures 2.22(a) and 2.22(c), respectively. These figures show high equivalent plastic strains near the weld toe on the top surface of the specimen. Some high equivalent plastic strains are also seen near the weld root. The location of the maximum equivalent plastic strain is near the top of the specimen near the notch surface in the base metal near the boundary of the weld metal. An optical micrograph of the cross section of a failed 30 mm specimen is shown in Figure 2.22(b). Figure 2.22(b) shows that the shear direction of the failed specimen is consistent with the high equivalent plastic strains shown in Figure 2.22(a).

The distributions of the void volume fraction near the weld for the long weld model at the mid-section of the specimen and on the top and outside surfaces of the specimen are shown in Figures 2.23(a) and 2.23(b), respectively. A small area of high void volume fractions can be seen near the pre-existing crack tip between the upper and lower sheets near the root of the weld. A closer review of the results of the finite element analyses indicates that, for both long and short models, the equivalent plastic strain does not grow in this area of localized plastic deformation near the pre-existing crack tip once

necking begins in the specimen. Therefore, failure is not expected to initiate in this area. The material elements with the larger void volume fractions are located near the weld toe in the base metal near the boundary of the weld metal. A close examination of the results of the finite element analyses reveals that the location of the maximum void volume fraction is not at the specimen surface but slightly below. Needleman and Tvergaard [25] indicated failure initiation slightly below the notch surface of a D-notch specimen under plane strain loading conditions. They noted that the failure prediction is expected since the stress-free condition on the surface lowers the hydrostatic tensile stresses. Figure 2.6(b) and Figure 2.22(b) show a failed specimen and the cross section near the weld from specimens that were machined from wide lap-shear specimens with longer weld lengths. These figures show that the failure location of the tested specimens is consistent with the location of the maximum void volume fraction. The ductile necking/shear failure mode exhibited by the failed specimens is also apparent at the location of the maximum void volume fraction in Figure 2.23(a).

2.5. Discussions on material properties and weld geometry

2.5.1. Finite element analysis for a parametric study

Finite element analyses were conducted in order to understand the effects of the mechanical properties and the geometry of the weld metal and the heat affected zone on the load-displacement responses and the predicted failure locations of the lap-shear joints. In order to remove the influence of the weld metal size and shape in this parametric study, the two finite element models for the 10 mm weld and the 40 mm weld were

modified such that the cross sectional outer surface profile of the weld metal of the specimen was kept the same for both. The generic outer surface profile of the weld metal was designed to match the micrograph of the cross section shown in Figure 2.9(d) for the 25 mm weld. Since the 10 mm and the 40 mm welds have different inner profiles of the weld metal adjacent to the heat affected zone in the top sheet and different heat affected zones, a generic short weld model and a generic long weld model were developed. The finite element meshes near the weld for the generic short weld and the generic long weld models are shown in Figures 2.24(a) and 2.24(b), respectively. The generic short weld model and the generic long weld model have the inner profile of the weld metal adjacent to the heat affect zone in the top sheet and the heat affected zones designed to closely match those of the realistic 10 mm weld model and the realistic 40 mm weld model shown in Figures 2.14(a) and 2.14(b), respectively.

Based on the two generic short and long weld models, finite element analyses were carried out. The results indicate that the areas of the high equivalent plastic strains and the predicted failure locations due to high void volume fraction are consistent with the results from the realistic 10 mm and 40 mm weld models with the weld metal cross sectional shape designed to match the micrographs of the cross sections for the 10 mm and 40 mm welds as shown in Figure 2.10(a).

2.5.2. Effect of the material stress-strain curves

In order to understand the effect of the material stress-strain curves, a finite element analysis was conducted by assuming a homogeneous material behavior

throughout the generic short weld model using the material properties of the base metal. The load-displacement curve of the lap-shear specimen from the finite element analysis based on the homogeneous material behavior is shown in Figure 2.25 along with the load-displacement curve from the generic short weld model and the experimental results of the specimens with shorter weld lengths. The load-displacement curves are plotted up to displacements that will result in material elements reaching the assumed critical void volume fraction of 0.22. These points are marked with open circles on the load-displacement curves. The load-displacement curve from the homogeneous material model is lower than the one for the generic short weld model and does not agree with the experimental results. The load-displacement response is too compliant and the peak load does not fall within the range of the experimental data. Figure 2.26(a) shows the distribution of the void volume fraction near the weld at the mid-section of the specimen for the homogeneous material model. The homogeneous material model predicts the initiation of ductile fracture due to void nucleation and growth near the weld root near the top surface of the specimen at the mid-section.

In order to understand the effect of the material stress-strain curves in the heat affected zone, a finite element analysis was conducted without consideration of the heat affected zone. For the generic short weld model, the heat affected zone was assigned the effective stress-plastic strain curve of the base metal and the weld metal was assigned the effective stress-plastic strain curve of the weld metal from the short weld model. Figure 2.25 shows that the load-displacement curve from the finite element analysis without consideration of the heat affected zone is higher than the one with the homogeneous material behavior and is lower than the one from the generic short weld model. Figure

2.26(b) shows the distribution of the void volume fraction near the weld on the top and outside surfaces of the specimen for the model without consideration of the heat affected zone. The results of the model without consideration of the heat affected zone suggests that the initiation of ductile fracture due to void nucleation and growth should be near the weld root near the top surface of the specimen in the base metal near the boundary of the weld metal.

2.5.3. Effect of the geometric characteristics of the heat affected zone

The micro-hardness tests discussed in Section 2.2.6 showed the trend in the hardness in the heat affected zone and the weld metal and the trend in the size and shape of the heat affected zone as the weld length increases. In this section, in order to understand the effect of the geometric characteristics of the heat affected zone independently from the effects of the effective stress-plastic strain curves, the generic finite element models were modified. The generic short weld model shown in Figure 2.24(a), where the heat affected zone adjacent to the weld metal in the bottom sheet extends past the toe of the weld, was modified to match the heat affected zone of the long weld model in this area, where the heat affected zone does not extend past the toe of the weld. Also, the angled shape of the heat affected zone adjacent to the base metal in the top sheet was modified to match the straight shape of the heat affected zone of the long weld model in this area. The effective stress-plastic strain curves were kept unchanged from the generic short weld model. The finite element mesh near the weld for the generic

short weld model with the modified geometric characteristics of the heat affected zone is shown in Figure 2.27(a) with the different material sections.

Similarly, the generic long weld model shown in Figure 2.24(b), where the heat affected zone adjacent to the weld metal in the bottom sheet does not extend past the toe of the weld, was modified to match the heat affected zone of the short weld model in this area, where the heat affected zone does extend past the toe of the weld. Also, the straight shape of the heat affected zone adjacent to the base metal in the top sheet was modified to match the angled shape of the heat affected zone of the short weld model in this area. The effective stress-plastic strain curves were kept unchanged from the generic long weld model. The finite element mesh near the weld for the generic long weld model with the modified geometric characteristics of the heat affected zone is shown in Figure 2.27(b) with the different material sections.

Figures 2.28(a) and 2.28(b) show the load-displacement curves from the finite element analyses of the generic short and long weld models, respectively, with and without the modified heat affected zone geometries. These figures show that the load-displacement curves from the finite element analyses match well and are in good agreement with the experimental results. The displacement needed to reach the assumed critical void volume fraction (marked with an open circle) is much lower for the short weld with the modified heat affected zone, when compared to the more realistic generic short weld model. The displacement needed to reach the assumed critical void volume fraction (marked with an open circle) is more for the long weld model with the modified heat affected zone, when compared to the more realistic generic long weld model.

Figures 2.29(a) and 2.29(b) show the distributions of the void volume fraction near the weld at the mid-section of the specimen and on the top and outside surfaces of the specimen, respectively, from the generic short weld model with the modified heat affected zone geometry. These figures show that when the heat affected zone geometry is modified, the initiation of ductile fracture due to void nucleation and growth changes from near the weld root to near the weld toe. The location of the initiation of ductile fracture matches the fracture initiation location of the long weld model.

Figures 2.30(a) and 2.30(b) show the distributions of the void volume fraction near the weld at the mid-section of the specimen and on the top and outside surfaces of the specimen, respectively, from the generic long weld model with the modified heat affected zone geometry. These figures show that when the heat affected zone geometry is modified, the initiation of ductile fracture due to void nucleation and growth changes from near the weld toe to near the weld root. The location of the initiation of ductile fracture matches the fracture initiation location of the short weld model.

With these results from the finite element analyses, it is concluded that the geometric characteristics of the heat affected zone are key factors for the resulting failure locations. When the heat affected zone in the bottom sheet extends past the toe of the weld and the heat affected zone in the top sheet adjacent to the base metal has the angled shape, the necking/shear failure occurs near the weld root. Likewise, when the heat affected zone in the bottom sheet does not extend past the toe of the weld and the heat affected zone in the top sheet adjacent to the base metal has the straight shape, the necking/shear failure occurs near the weld toe. Further finite element analyses were conducted in order to understand the individual effects of these geometric characteristics.

The results of the finite element analyses showed that neither the modification to the length of the heat affected zone in the bottom sheet nor the modification to the shape of the heat affected zone in the top sheet individually will result in a change of the failure location. Instead, both modifications are necessary to result in a change in the failure location.

2.5.4. Effect of weld metal geometry

Koganti et al. [6] studied different weld geometries in DP780 single lap-shear joints under quasi-static and cyclic loading conditions. The experimental results indicated that welds with larger toe angles and less penetration show longer high-cycle fatigue lives and fail near the weld root while welds with smaller toe angles and larger penetrations fail near the weld toe. The quasi-static strength of the welds was found to be insensitive to weld geometry. A parametric study presented here can give some insight on the effect of toe angle and weld metal penetration on the quasi-static strength of the lap-shear joints.

In order to understand the effect of the weld metal penetration, the weld penetration was removed from the generic short weld and long weld models. Figures 2.31(a) and 2.31(b) show the modification made to the amount of weld penetration in the generic short weld and long weld finite element models, respectively. Although the weld penetration into the bottom sheet was seen in every weld specimen sectioned, the weld penetration was completely removed in these computations in order to highlight any effect on the load-displacement response or the failure location. In order to study to

effect of the weld penetration only, the heat affected zone near the weld toe was kept unchanged in the bottom sheet as shown in Figures 2.31(a) and 2.31(b) and the depth of the heat affected zones from the lower boundary of the weld metal follow the general trends of those in Figure 2.24. The results of the load-displacement curves from the finite element analyses indicate that the weld penetration has negligible effect on the load-displacement response, including the peak load. The results of the finite element analyses also show that the weld penetration does not affect the predicted failure location.

It should be mentioned that when the weld penetration is removed, the high stress-strain curves of the heat affected zone prevent large scale yielding between the weld toe and weld root. Lee et al [19] conducted a parametric study on the effects of the weld width on the plastic deformation mode in and near the laser welds in lap-shear specimens. They found that that high shear plastic strains can occur in the weld for a homogeneous material model when the weld width becomes small compared to the sheet thickness. However, when the 3-zone and 6-zone material models with consideration of higher stress-strain curves of the weld and heat affected zones were used, the computational results showed that the large plastic strains occur in the load carrying sheets near the weld, not in the weld.

In order to understand the effect of the weld toe angle, the weld toe angles in the generic finite element models were decreased from 150 degrees to 135 degrees. Figure 2.32 shows the finite element model without and with the modified toe angle. The dark regions in the figures represent the weld and the shaded regions in the figures indicate the extra weld region in the generic long weld model. The results of the load-displacement curves from the finite element analyses indicate that the toe angle has negligible effect on

the load-displacement curves, including the peak load. For the long weld model, in which the heat affected zone does not extend past the toe of the weld, the decreased toe angle produces a higher stress concentration at the toe of the weld and results in a reduced displacement at failure. The results of the finite element analyses also show that the toe angle does not affect the predicted failure locations.

Finally, it should be mention again that the sizes and shapes of the weld metal and the heat affected zone can vary for a given weld length as shown in Figures 2.9 and 2.10 for the 10 mm, 25 mm and 40 mm welds. As indicated in the results from the parametric study of the weld geometry and material stress-strain curve, as long as the stress-strain curves for the material elements in the finite element models are correlated to the hardness distribution in and near the weld with consideration of the geometric characteristics of the heat affected zones, the load-displacement curves and the failure locations from the finite element analyses agree with the experimental results.

2.6. Discussion and conclusions

The strengths and the fatigue lives of gas metal arc welded joints were investigated by many researchers. Investigators reported quasi-static and fatigue failure locations sometimes near the weld root and sometimes near the weld toe. In this study, the failure modes of gas metal arc welds in single lap-shear specimens of high strength low alloy (HSLA) steel are investigated. Notched lap-shear specimens of HSLA steel sheets with a thickness of 2.0 mm were robot welded together using the gas metal arc welding process. Quasi-static test results showed two failure locations for the welds.

The specimens cut from wide lap-shear specimens with shorter weld lengths failed near the weld root whereas the specimens cut from those with longer weld lengths failed near the weld toe. Scanning electron and optical microscope images of the failure surfaces and cross sections showed that the gas metal arc welds failed in a ductile necking/shear failure mode. Micro-hardness tests were conducted to provide an assessment of the mechanical properties of the base metal, the heat affected zone, and the weld metal. In order to understand the failure modes of short welds and long welds, two finite element models were developed. In these models, the size and shape of the heat affected zones were designed to match the micrographs of the cross sections for a 10 mm weld and a 40 mm weld. Three-dimensional finite element analyses were conducted with consideration of micro void nucleation and growth. The distributions of the void volume fraction near the welds shown from the finite element analyses are consistent with the failure modes observed in the experimental results.

Further finite element analyses were conducted in order to understand the effects of the geometric characteristics of the heat affected zone on the load-displacement responses and the predicted failure locations of the lap-shear joints. The results showed that the heat affected zones and the weld metal, with higher effective stress-plastic strain curves, significantly affects the load-displacement response and the predicted failure locations of the lap-shear specimens. The results also showed that the geometric characteristics of the heat affected zone have negligible effect on the load-displacement results; however, the geometric characteristics of the heat affected zone are key factors for the resulting failure locations. Finally, finite element analyses were conducted in order to understand the effect of the weld geometry. A parametric study was conducted

to give some insight on the effect of the weld metal penetration and the weld toe angle on the quasi-static strength of the lap-shear joints. The results indicate that the weld penetration and the weld toe angle have negligible effects on the load-displacement response and the predicted failure locations of the lap-shear specimens.

Acknowledgements

The support of this work by Johnson Controls Inc. is greatly appreciated. The encouragement and assistance of W. Randy Tighe, J. David Kotre, and Mark Harris of Johnson Controls is also greatly appreciated.

References

1. Yan, B., Lalam, S.H., Zhu, H., "Performance Evaluation of GMAW Welds for Four Advanced High Strength Steels," SAE Technical Paper 2005-01-0904, Warrendale, PA, 2005.

2. Feng, Z., Carpenter, J.A., Sklad, P.S., "Characterization of Thermo-Mechanical Behaviors of Advanced High Strength Steels (AHSS): Task 2 - Weldability and Performance Evaluations of AHSS Parts for Automotive Structures," FY 2006 Progress Report, Automotive Lightweighting Materials, pp i206-i218, 2006.

3. Joaquin, A., Elliott, N.A., Jiang, C., Rajan, V., Hartman, D., and Karas, C., "Gas Metal Arc Welding of Advanced High Strength Steel - Developments for Optimized Welding Control and Weld Quality," SAE Technical Paper 2006-01-0300, Warrendale, PA, 2006.

4. Joaquin, A., Elliott, N.A., Jiang, C., Rajan, V., Hartman, D., and Karas, C., "Gas Metal Arc Welding of Coated Advanced High Strength Steel (AHSS) - Developments for Improved Weld Quality," SAE Technical Paper 2007-01-1360, Warrendale, PA, 2007.

5. Koganti, R., Angotti, S., Joaquin, A., Jiang, C., Karas, C., "Effect of Materials Stack-ups and Microhardness Distribution on Fatigue Performance of DP600 and Boron Steel GMAW Lap Joint," SAE Technical Paper 2007-01-1356, Warrendale, PA, 2007.

6. Koganti, R., Angotti, S., Joaquin, A., Jiang C., "Effect of Weld Geometry and HAZ Softening on Fatigue Performance of DP780 GMAW Lap Joint," SAE Technical Paper 2007-01-0632, Warrendale, PA, 2007.

7. Angotti, S., Koganti, R., Joaquin, A., Jiang, C., "Static and Fatigue Performance of Fusion Welded Uncoated DP780 Coach Joints," SAE Technical Paper 2008-01-0695, Warrendale, PA, 2008.

8. Kapustka, N., Conrardy, C., Babu, S., Albright, C., "Effect of GMAW Process and Material Conditions of DP 780 and TRIP 780 Welds," Supplement to the Welding Journal, Vo. 87, pp. 135-s - 148-s, 2008.

9. Bonnen J.J.F., Mandapati, R., Kang, H., Iyengar, R.M., Khosrovaneh, A.K., Amaya, M. A., Citrin, K., Shih, H. C., "Durability of Advanced High Strength Steel Gas Metal Arc Welds," SAE Technical Paper 2009-01-0257, Warrendale, PA, 2009.

10. Categorization and Properties of Dent Resistant, High Strength, and Ultra High Strength Automotive Sheet Steel. SAE J2340. October, 1999.

11. Asim, K., Lee, J., Pan, J., “Failure Mode of Laser Welds in Lap-shear Specimens of High Strength Low Alloy (HSLA) Steel Sheets,” Fatigue and Fracture of Engineering Materials and Structures, Vol. 35, pp. 219-237, 2011.

12. Callister, W. D., "Materials Science and Engineering: An Introduction," 3rd ed. New York: John Wiley and Sons, Inc., pp. 182-187, 1985.

13. Vander Voort, G. F., “Visual Examination and Light Microscopy,” Fractography, Vol. 12, ASM Handbook, ASM International, 1987, pp 91–165, in ASM Handbooks Online, http://www.asmmaterials.info ASM International, 2002.

14. Becker, W. T., McGarry, D., “Mechanisms and Appearances of Ductile and Brittle Fracture in Metals,” Failure Analysis and Prevention, Vol. 11, pp 587-626, in ASM Handbooks Online, http://www.asmmaterials.info ASM International, 2002.

15. "ABAQUS 6.11 Analysis User's Manual," Dassault Systèmes Simulia Corp., Providence, RI, 2011.

16. "ABAQUS 6.11 Keywords Reference Manual," Dassault Systèmes Simulia Corp., Providence, RI, 2011.

17. "ABAQUS 6.11 Theory Manual," Dassault Systèmes Simulia Corp., Providence, RI, 2011.

18. ASTM Standard E8/E8M, 2008, "Standard Test Methods for Tension Testing of Metallic Materials," ASTM International, West Conshohocken, PA, 2008, 10.1520/E0008_E0008M-08, www.astm.org.

19. Lee, J., Asim, K., Pan, J., “Modeling of Failure Mode of Laser Welds in Lap-Shear Specimens of HSLA Steel Sheets,” Engineering Fracture Mechanics, Vol. 78, pp. 374-396, 2011.

20. Gurson, A. L., "Continuum Theory of Ductile Rupture by Void Nucleation and Growth: Part 1 – Yield Criteria and Flow Rules for Porous Ductile Media", Journal of Engineering Materials and Technology, Vol. 99, pp. 2-55, 1977.

21. Gurland, J., "Observations on Fracture of Cementite Particles in a Spheroidized 1.05% C Steel Deformed at Room Temperature," Acta Metallurgica, Vol. 20, pp. 735-741, 1972.

22. Tvergaard, V., Needleman, A., "Analysis of the Cup-Cone Fracture in a Round Tensile Bar," Acta Metallurgica, Vol. 32, pp. 157-169, 1984.

23. Tvergaard, V., "Influence of Voids on Shear Band Instabilities under Plane Strain Conditions," International Journal of Fracture, Vol. 17, pp. 389-407, 1981.

24. Chu, C. C., Needleman, A., “Void Nucleation Effects in Biaxially Stretched Sheets.,” Journal of Engineering Materials and Technology, Vol. 102, pp. 249–256, 1980.

25. Needleman, A., Tvergaard, V., “An Analysis of Ductile Rupture in Notched Bars,” Journal of the Mechanics and Physics of Solids, Vol. 32, pp. 461-490, 1984.

Table 2.1. The main fracture locations observed in recent investigations of lap-shear specimens under quasi-static and dynamic loading conditions

Material	Loading Conditions	Joint Type	Main Fracture Location	Ref.
SAE1008	Quasi-static	Double and single lap shear	Not reported	9
HSLA350	Quasi-static	Single lap shear	Weld root	1
HSLA420	Quasi-static	Double and single lap shear	Weld toe	9
HSLA590	Quasi-static	Single lap shear	Weld root	2
DP590	Quasi-static	Double and single lap shear	Weld toe	9
DP600	Quasi-static	Single lap shear	Weld root	1
DP600	Quasi-static	Single lap shear	Weld root	2
DP600	Quasi-static	Double and single lap shear	Weld toe	9
DP780	Quasi-static	Single lap shear	Weld root	2
DP780	Quasi-static	Single lap shear	Weld root	8
DP780	Dynamic	Single lap shear	Weld root	8
DP780	Quasi-static	Double and single lap shear	Weld toe	9
DP965	Quasi-static	Single lap shear	Weld root	1
DP980	Quasi-static	Single lap shear	Weld root	2
DP980	Quasi-static	Single lap shear	Weld root	8
DP980	Dynamic	Single lap shear	Weld root	8
M900	Quasi-static	Double and single lap shear	Weld toe	1
M1300	Quasi-static	Single lap shear	Weld toe	1
TRIP780	Quasi-static	Single lap shear	Weld root	8
TRIP780	Dynamic	Single lap shear	Weld root	8
TRIP780	Quasi-static	Double and single lap shear	Weld toe	9
Boron Steel	Quasi-static	Single lap shear	Weld root	2
Boron Steel	Quasi-static	Double and single lap shear	Weld toe	9
DQSK	Quasi-static	Double and single lap shear	Not reported	9
Top mild steel to bottom DP600	Quasi-static	Single lap shear	Weld root	3.4
Top DP600 to bottom boron steel	Quasi-static	Single lap shear	Weld root	5
Top boron steel to bottom DP600	Quasi-static	Single lap shear	Weld toe	5

Table 2.2. The main fracture locations observed in recent investigations of lap-shear specimens under cyclic loading conditions

Material	Joint Type	Main Fracture Location	Ref.
SAE1008	Single lap shear	Changes with load level	9
SAE1008	Double lap shear	Not reported	9
HSLA350	Single lap shear	Changes with load level	1
HSLA420	Single lap shear	Changes with load level	9
HSLA420	Double lap shear	Not reported	9
HSLA590	Single lap shear	Not reported for all specimens	2
DP590	Single lap shear	Changes with load level	9
DP590	Double lap shear	Weld toe	9
DP600	Single lap shear	Changes with load level	1
DP600	Single lap shear	Not reported for all specimens	2
DP600	Single lap shear	Changes with load level	9
DP600	Double lap shear	Not reported	9
DP780	Single lap shear	Not reported for all specimens	2
DP780	Single lap shear	Both failure locations	6
DP780	Double lap shear	Weld toe	9
DP980	Single lap shear	Not reported for all specimens	2
DP965	Single lap shear	Changes with load level	1
M130	Single lap shear	Not reported for all specimens	2
M220	Single lap shear	Not reported for all specimens	2
M900	Double and single lap shear	Changes with load level	1
M1300	Single lap shear	Changes with load level	1
TRIP780	Double lap shear	Weld toe	9
Boron Steel	Single lap shear	Not reported for all specimens	2
Boron Steel	Single lap shear	Changes with load level	9
Boron Steel	Double lap shear	Not reported	9
DQSK	Double lap shear	Weld toe	9
Top mild steel to bottom DP600	Single lap shear	Both failure locations	3,4
Top DP600 to bottom boron steel	Single lap shear	Weld toe	5
Top boron steel to bottom DP600	Single lap shear	Weld root	5
Top DP595 to bottom SAE1008	Double lap shear	Weld toe	9
Top DP600 to bottom SAE1008	Double lap shear	Weld toe	9
Top TRIP780 to bottom SAE1008	Double lap shear	Weld toe	9
Top DP780 to bottom SAE1008	Double lap shear	Weld toe	9

Table 2.3. Chemical composition (wt %) of the SAE J2340 340XF steel sheets

C	Mn	Si	P	S	Cr	Ni	Mo
0.055	0.563	0.028	0.008	0.0045	0.014	0.014	0.002
Cu	V	Al	Ti	Nb	B	Pb	Mg
0.0172	0.001	0.046	0.001	0.0187	0	0.0013	0.0003

Table 2.4. Summary of results of the quasi-static tests

Specimen	Peak Load (N)	Fracture Location
S1-10	8262	Weld Root
S2-15	8943	Weld Root
S3-20	7889	Weld Root
S4-20	8723	Weld Toe
S5-30	7993	Weld Toe
S6-30	8247	Weld Toe
S7-40	8214	Weld Toe

Table 2.5. The hardness values from indentation tests and the scaled initial yield stresses for the base metal, heat affected zones and weld metal for (a) the short weld model and (b) the long weld model.

(a) Short weld model

	Base metal	HAZ 1	HAZ 2	HAZ 3	Weld metal
Vickers hardness	160	170	179	208	304
Yield stress σ_0 (MPa)	368	390	412	478	699

(b) Long weld model

	Base metal	HAZ 1	HAZ 2	Weld metal
Vickers hardness	160	170	179	232
Yield stress σ_0 (MPa)	368	390	412	534

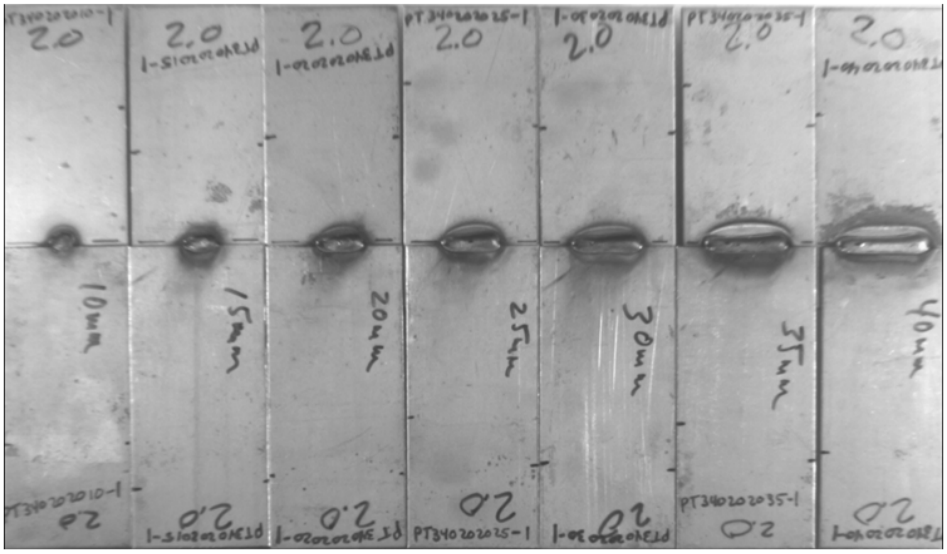

(a)

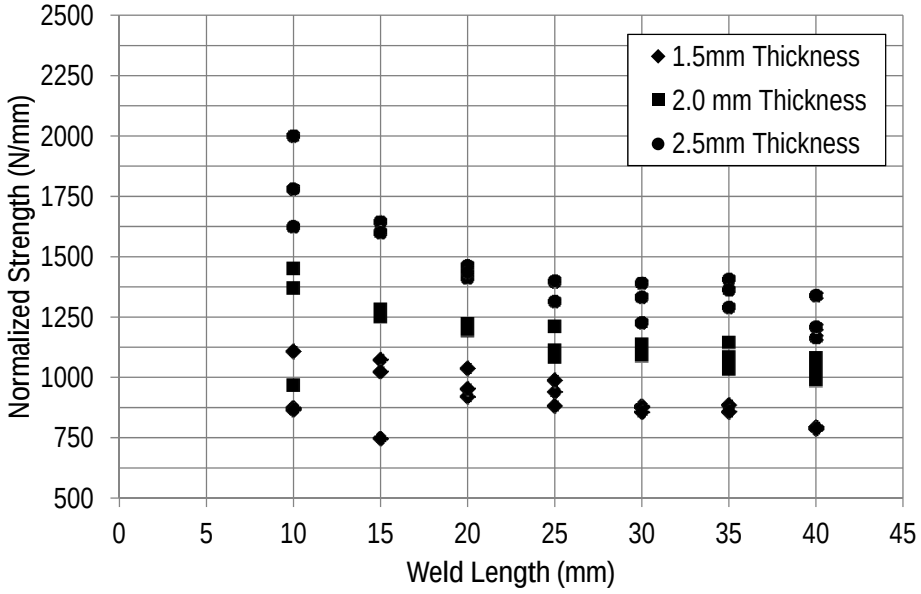

(b)

Figure 2.1. (a) Wide lap-shear specimens with the weld length varying from 10 mm to 40 mm. (b) The normalized weld strengths (per weld length) for specimens of various thicknesses.

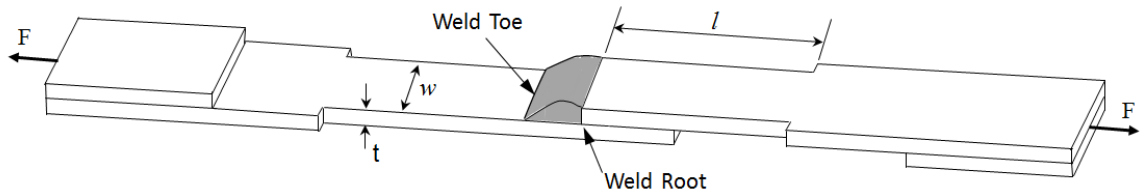

(a)

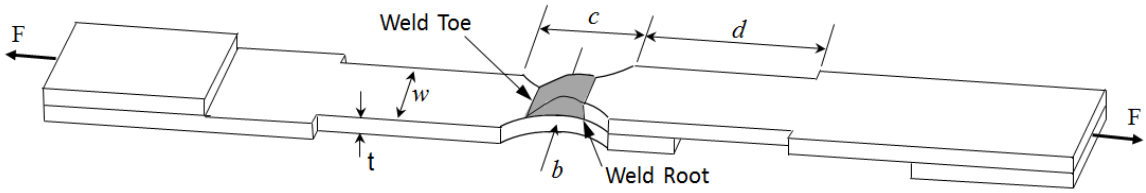

(b)

Figure 2.2. A schematic of (a) an un-notched lap-shear specimen and (b) a notched lap-shear specimen.

Figure 2.3. The failure location of an un-notched lap-shear specimen. The failure occurred in the base metal, away from the weld region.

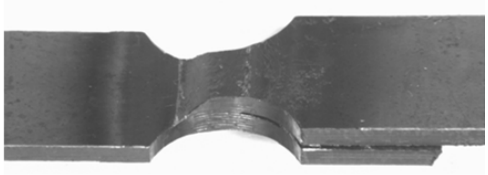

Figure 2.4. A close-up view near the weld of a notched lap-shear specimen.

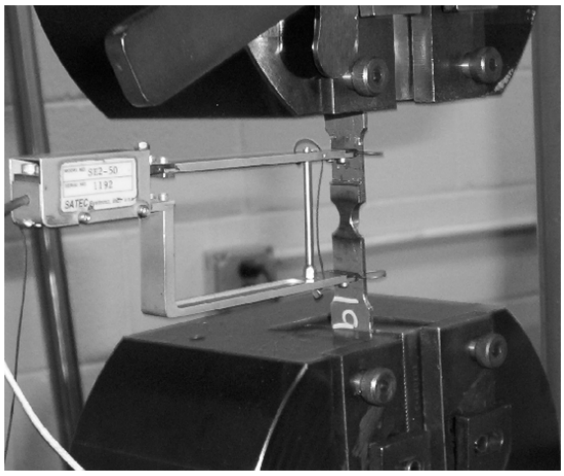

Figure 2.5. The test setup for notched lap-shear specimens.

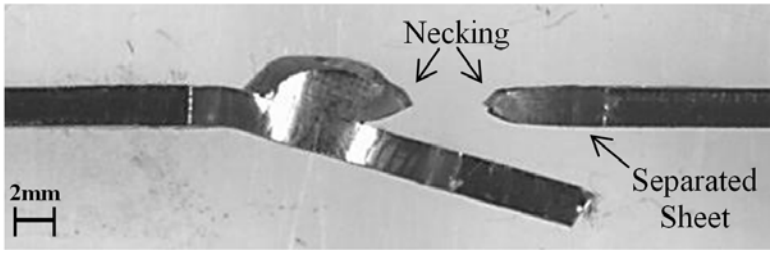

(a)

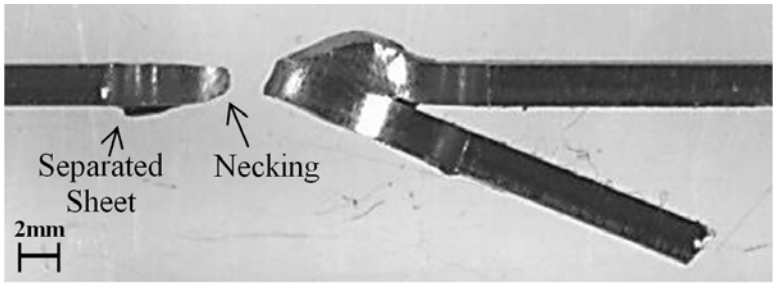

(b)

Figure 2.6. (a) A failed specimen machined from a wide specimen with a weld length of 10 mm and (b) a failed specimen machined from a wide specimen with a weld length of 30 mm.

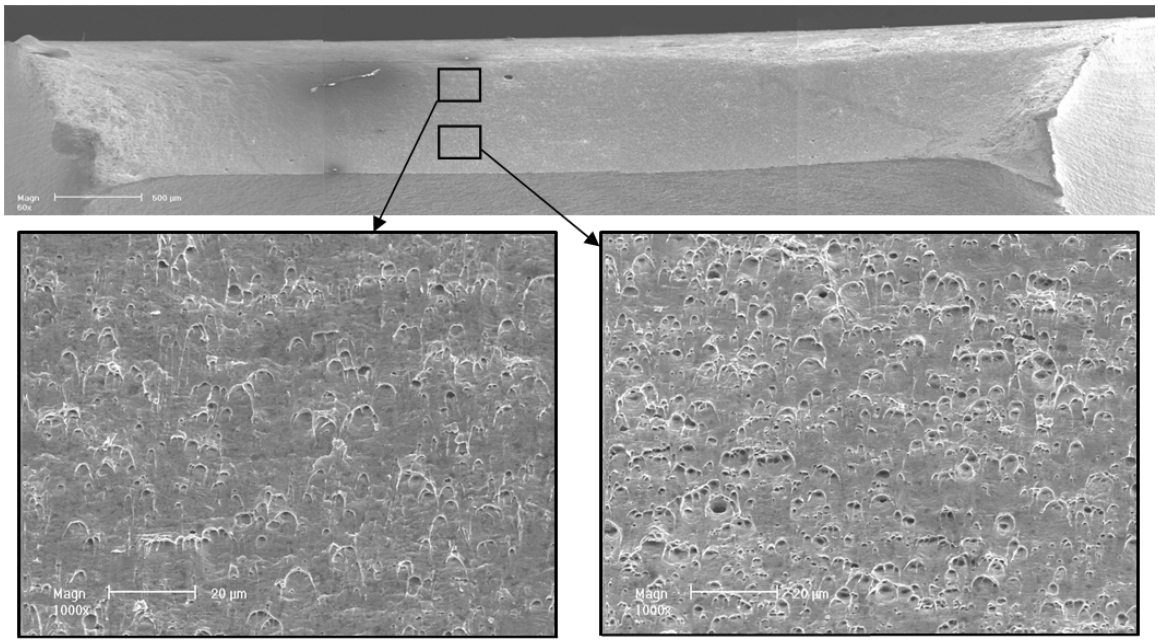

Figure 2.7. A scanning electron micrograph and close-up views of the failure surface from a specimen machined from a wide specimen with a weld length of 15 mm.

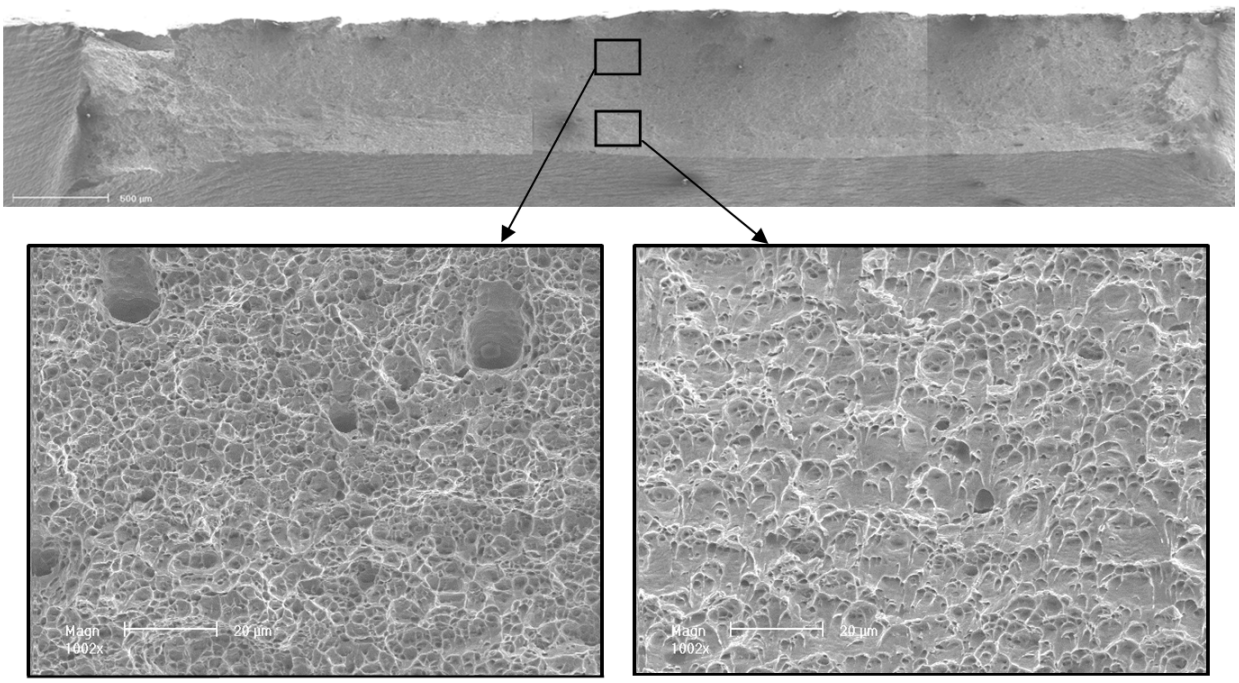

Figure 2.8. A scanning electron micrograph and close-up views of the failure surface from a specimen machined from a wide specimen with a weld length of 30 mm.

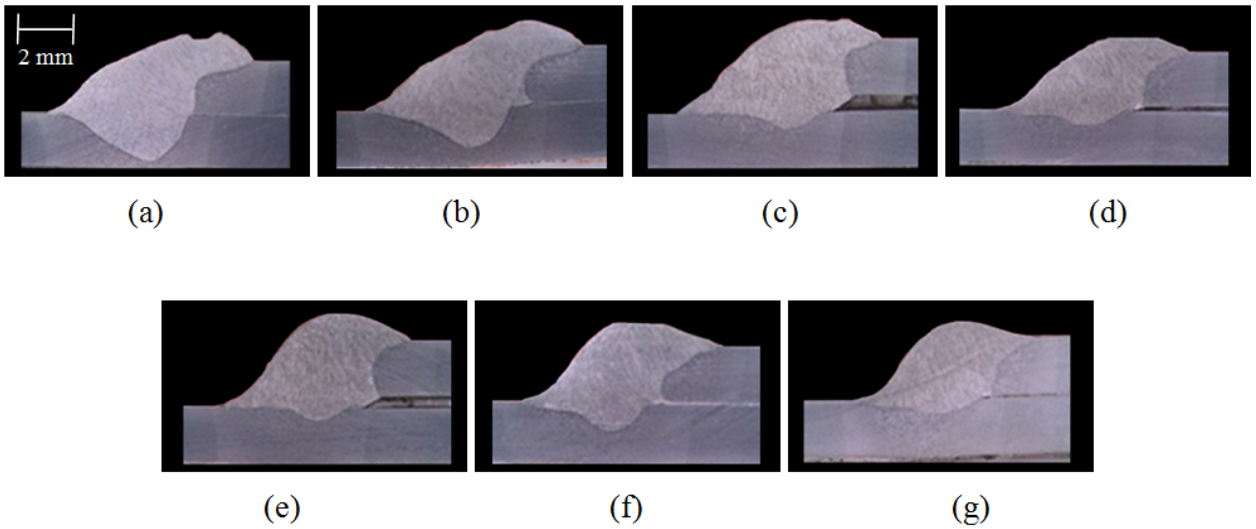

Figure 2.9. Micrographs of the cross sections of seven weld specimens with weld lengths of (a) 10 mm, (b) 15 mm, (c) 20 mm, (d) 25 mm, (e) 30 mm, (f) 35 mm, and (g) 40 mm.

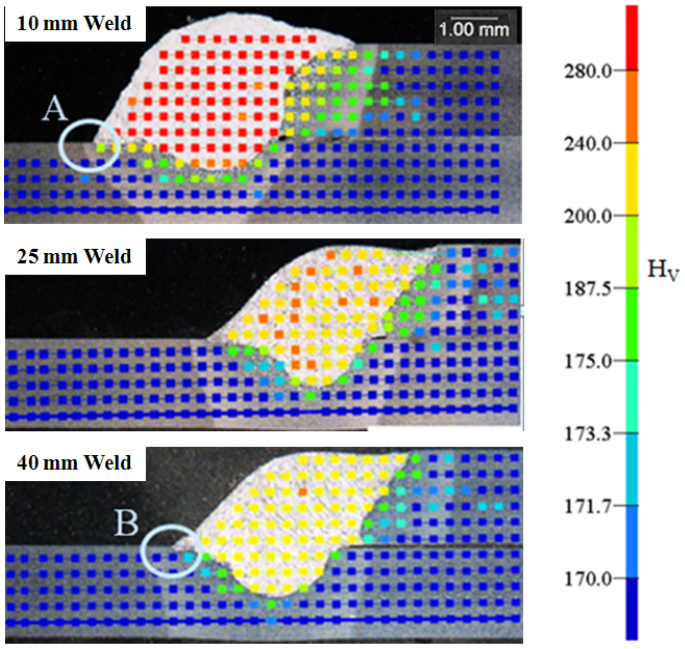

(a)

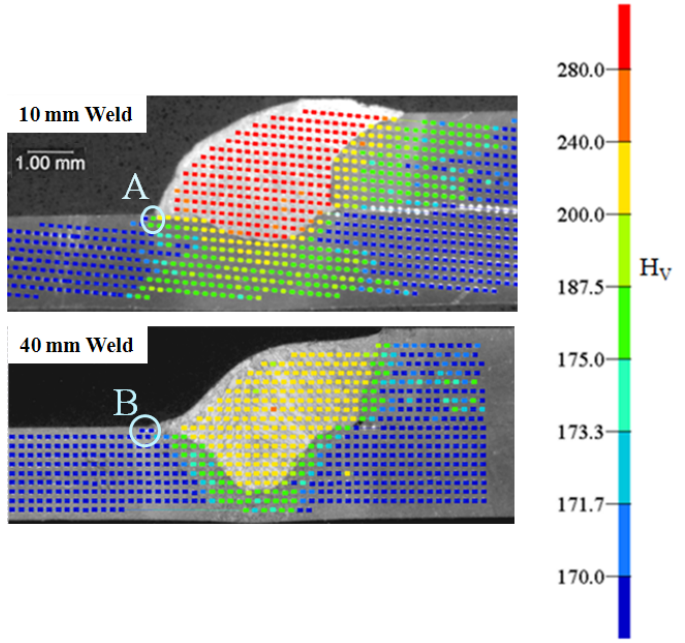

(b)

Figure 2.10. The Vickers hardness values in the weld region for specimens with short and long welds. The indentations were carried out at an interval of about (a) 350 μm and (b) 200 μm.

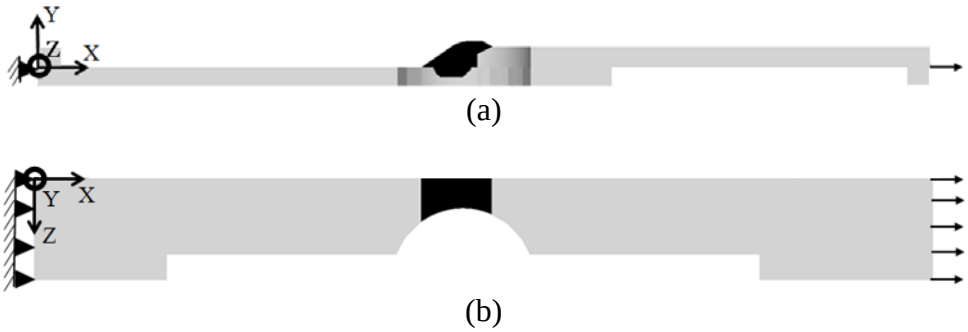

Figure 2.11. (a) The top view and (b) the side view of a finite element model of a notched lap-shear specimen.

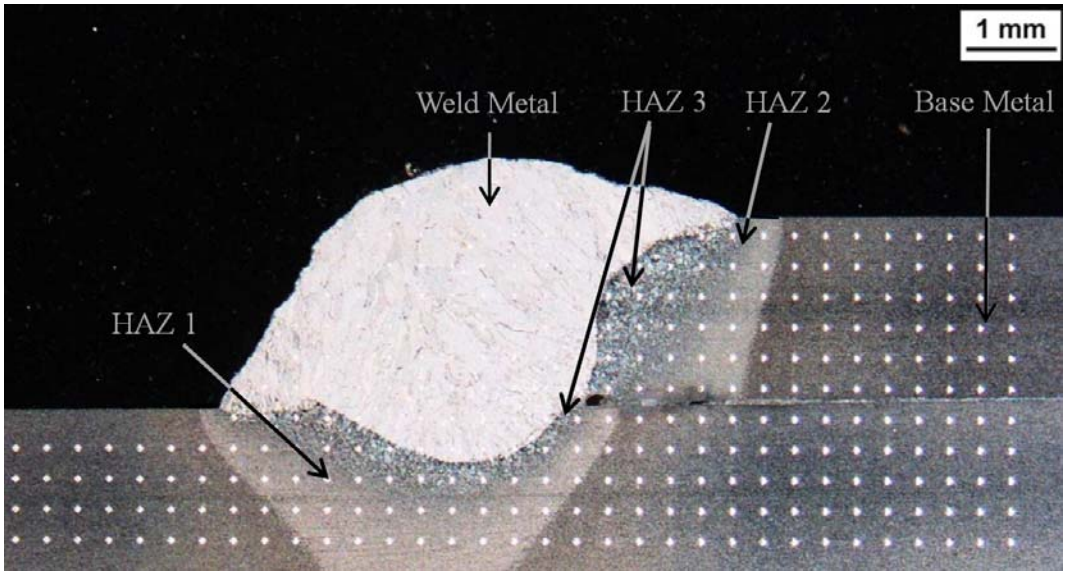

Figure 2.12. An optical micrograph of the cross section of a 10 mm weld specimen.

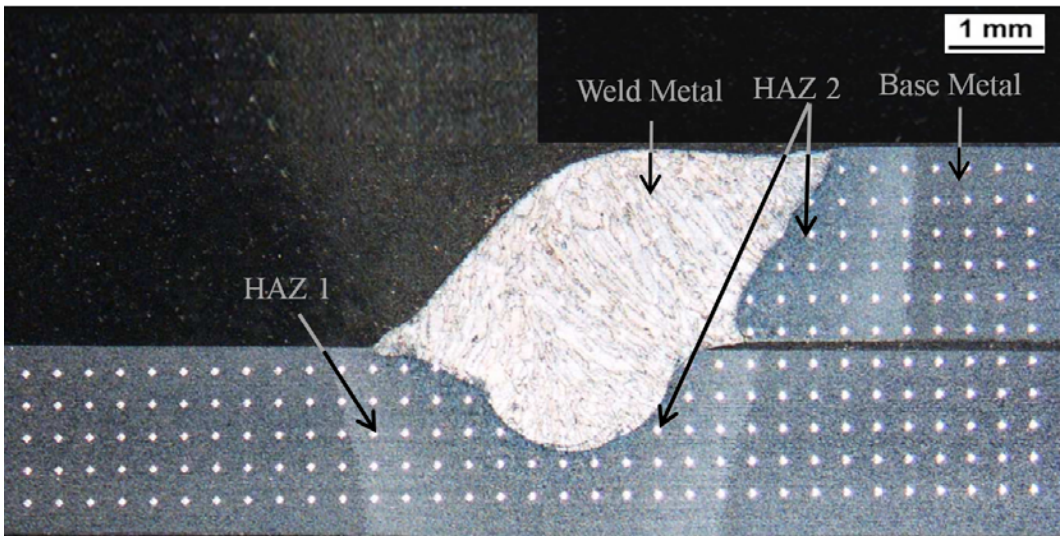

Figure 2.13. An optical micrograph of the cross section of a 40 mm weld specimen.

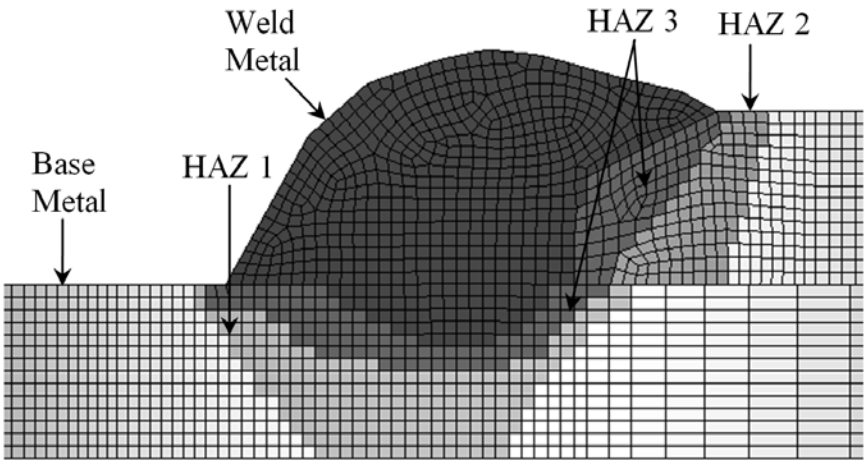

(a)

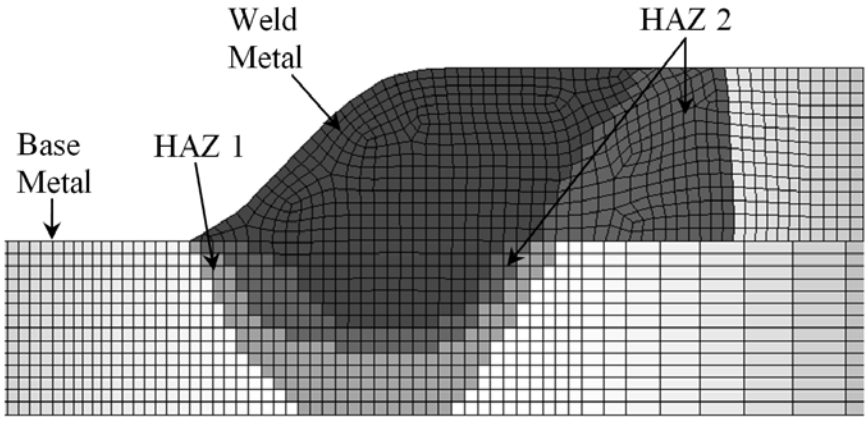

(b)

Figure 2.14. The finite element meshes near the weld for (a) the short weld model and (b) the long weld model with the different material sections.

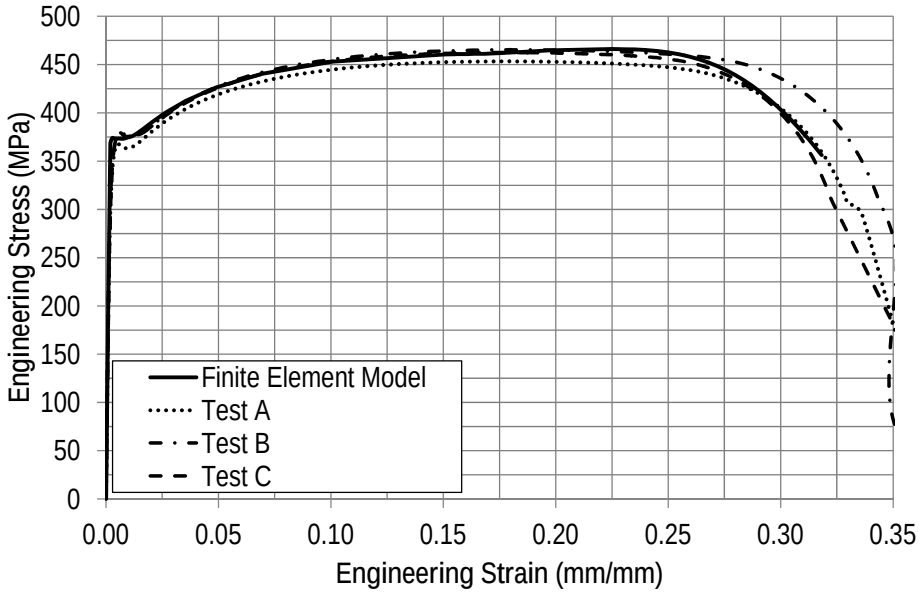

Figure 2.15. The engineering stress-strain curves for the base metal from three representative sheet specimens and the resulting curve from the finite element analysis.

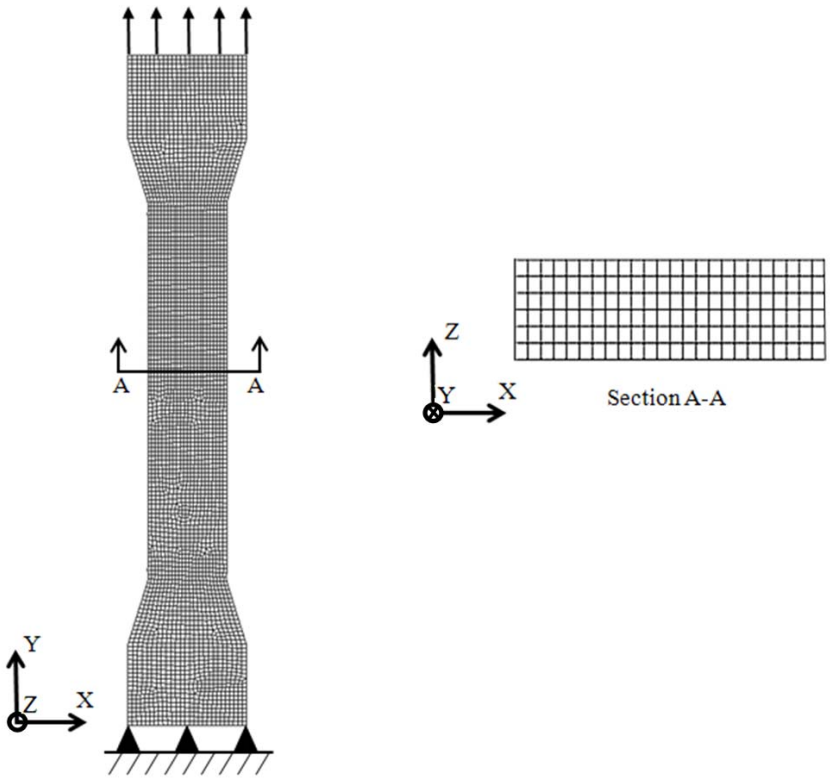

Figure 2.16. A finite element model of the tensile specimen.

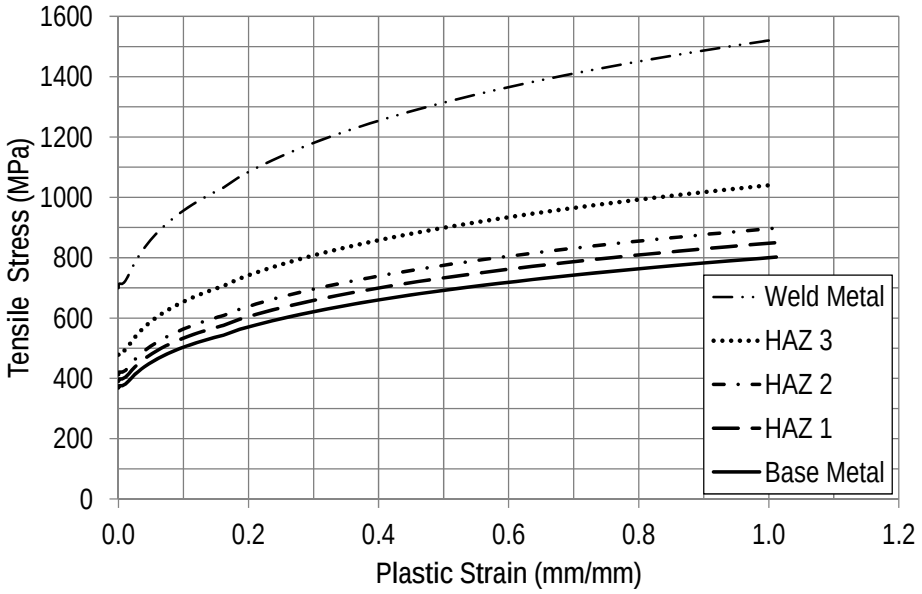

(a)

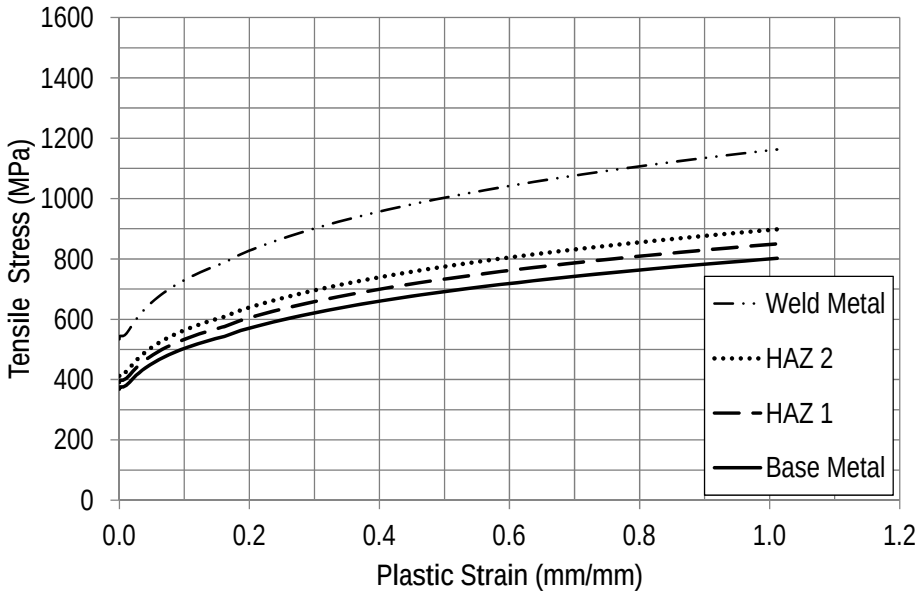

(b)

Figure 2.17. The tensile stresses as functions of the plastic strain for the base metal, the heat affected zones, and the weld metal used in (a) the short weld and (b) the long weld finite element models.

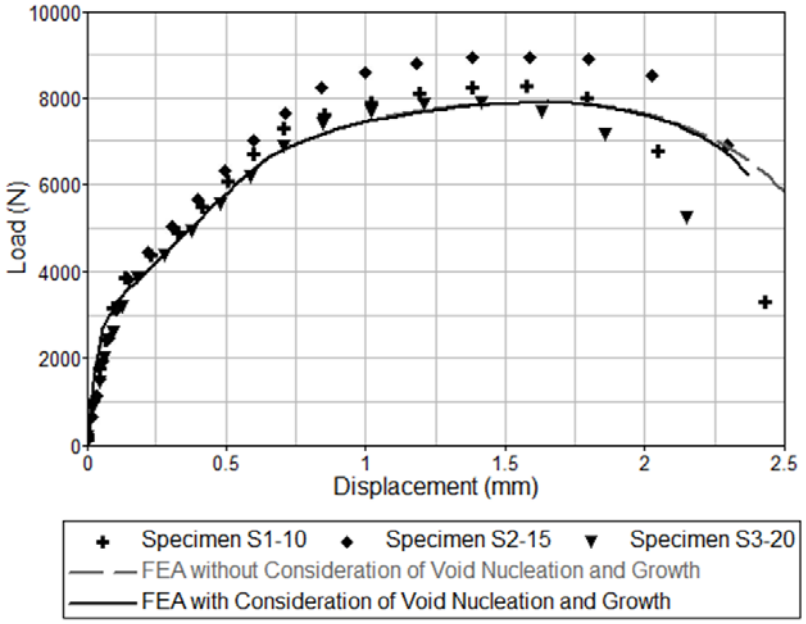

(a)

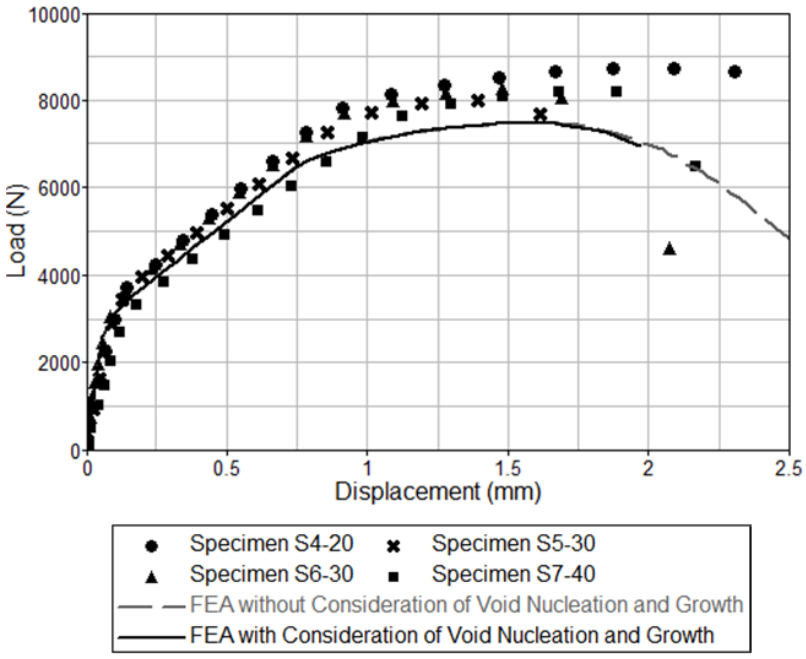

(b)

Figure 2.18. The load-displacement curves of the tested lap-shear specimens compared to those of the finite element analyses, with and without the consideration of void nucleation and growth for (a) the short weld model and (b) the long weld model.

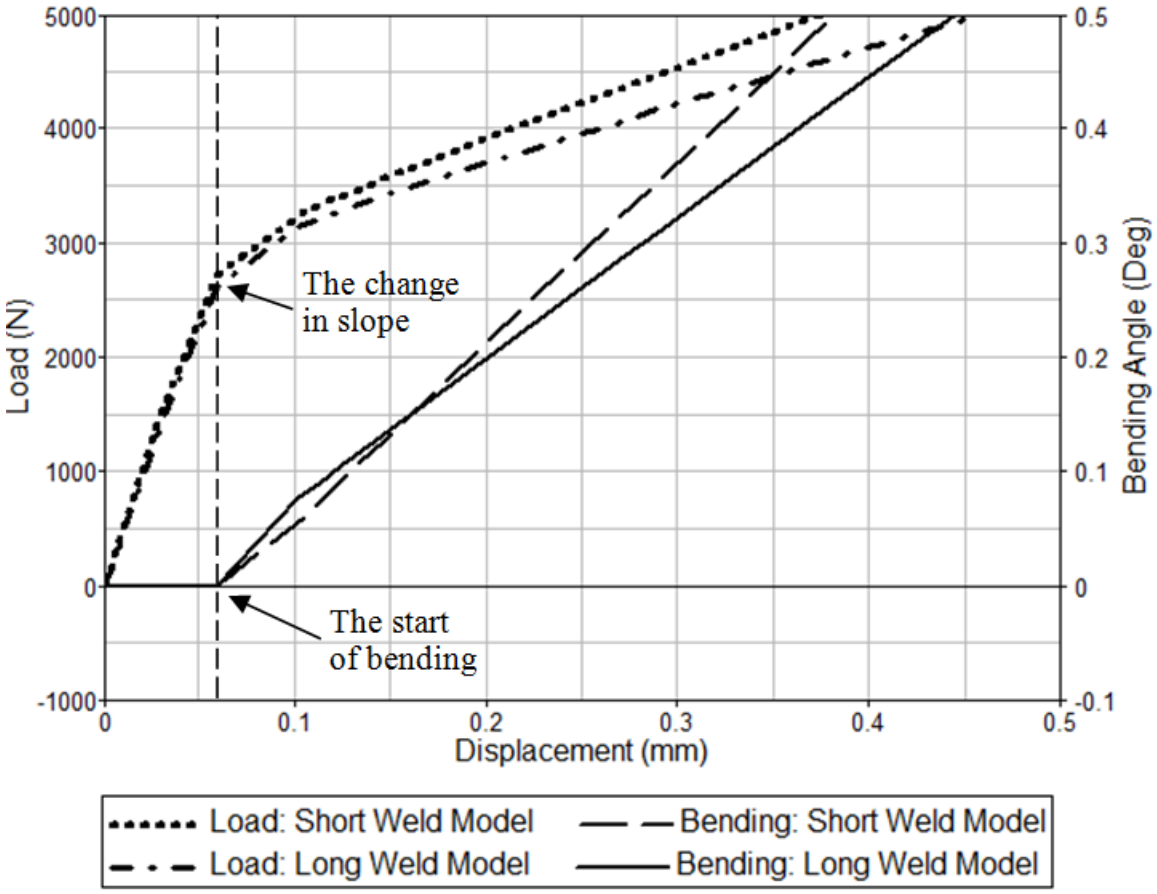

(a)

(b)

Figure 2.19. (a) The applied load and the bending of the bottom sheet plotted as functions of the displacement. (b) A method of quantifying the rotation of the bottom sheet.

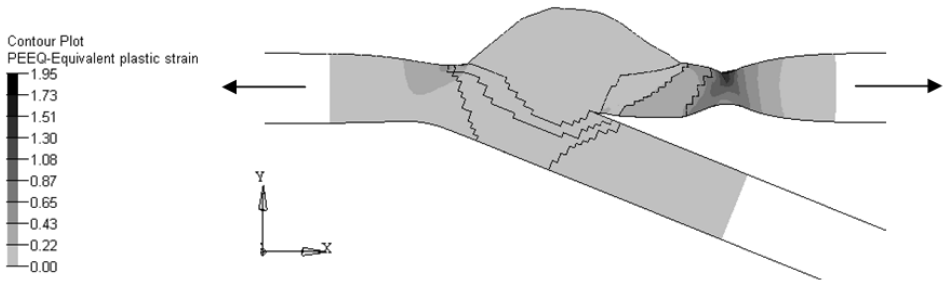

(a)

(b)

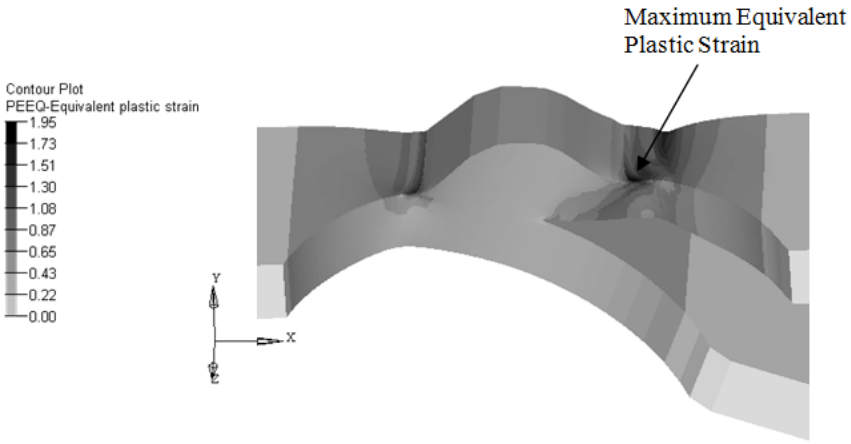

(c)

Figure 2.20. (a) The equivalent plastic strain distribution near the weld for the short weld model at the mid-section of the specimen. (b) An optical micrograph of the cross section near the weld of a failed 15 mm specimen. (c) The equivalent plastic strain distribution near the weld for the short weld model on the top and outside surfaces of the specimen.

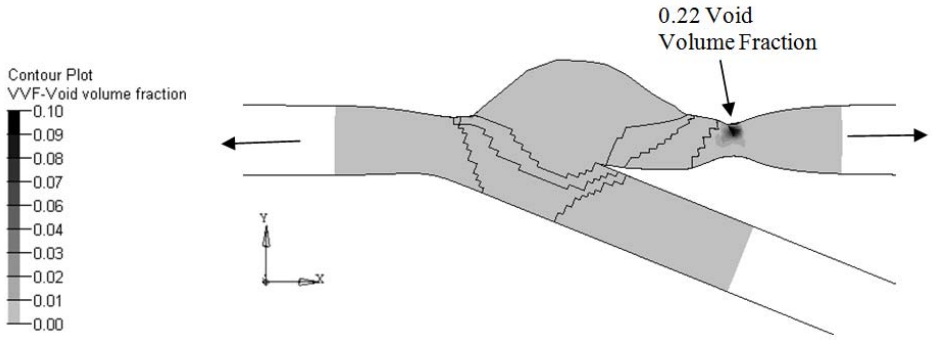

(a)

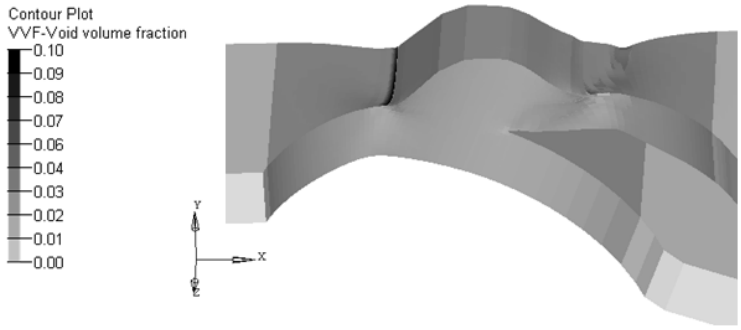

(b)

Figure 2.21. The distributions of the void volume fraction near the weld for the short weld model at (a) the mid-section of the specimen and on (b) the top and outside surfaces of the specimen.

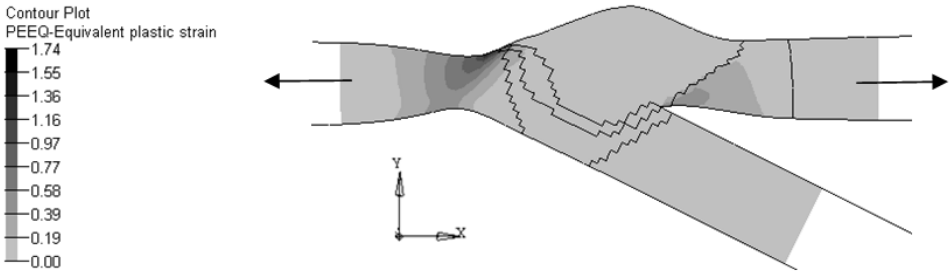

(a)

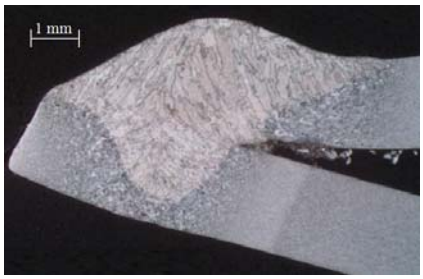

(b)

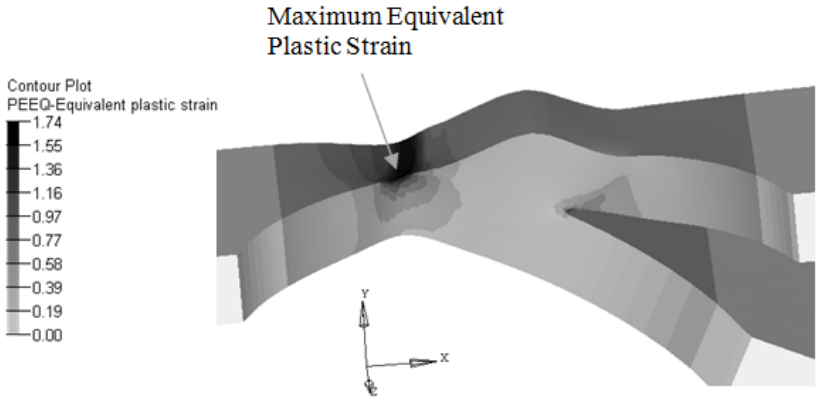

(c)

Figure 2.22. (a) The equivalent plastic strain distribution near the weld for the long weld model at the mid-section of the specimen. (b) An optical micrograph of the cross section near the weld of a failed 30 mm specimen. (c) The equivalent plastic strain distribution near the weld for the long weld model on the top and outside surfaces of the specimen.

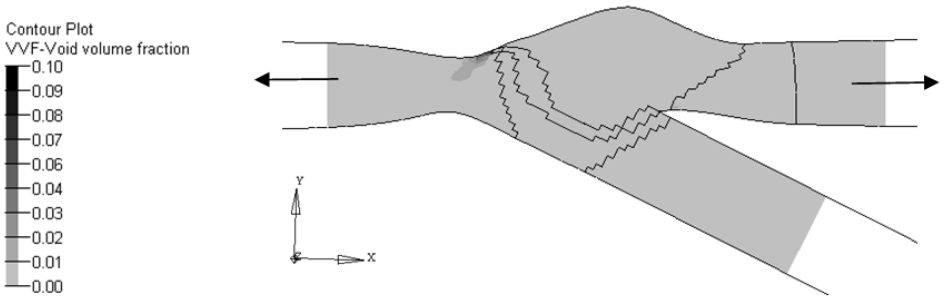

(a)

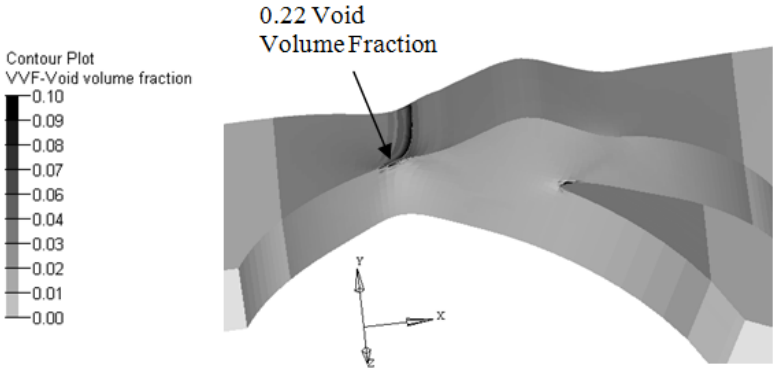

(b)

Figure 2.23. The distributions of the void volume fraction near the weld for the long weld model at (a) the mid-section of the specimen and on (b) the top and outside surfaces of the specimen.

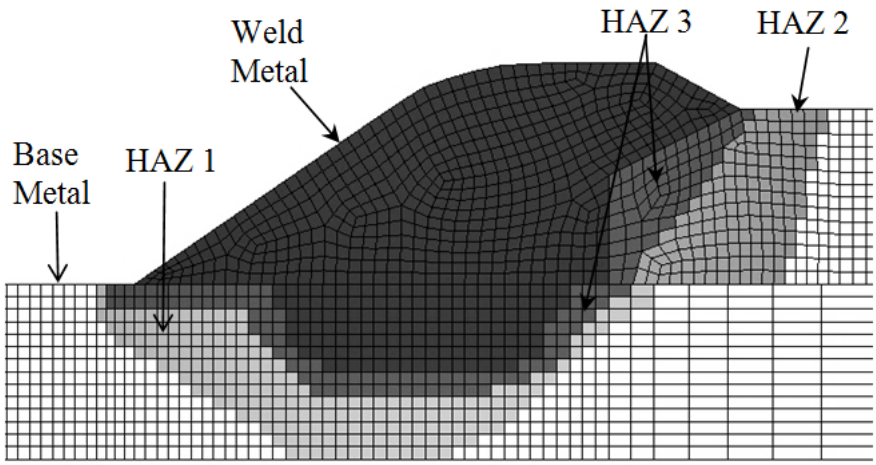

(a)

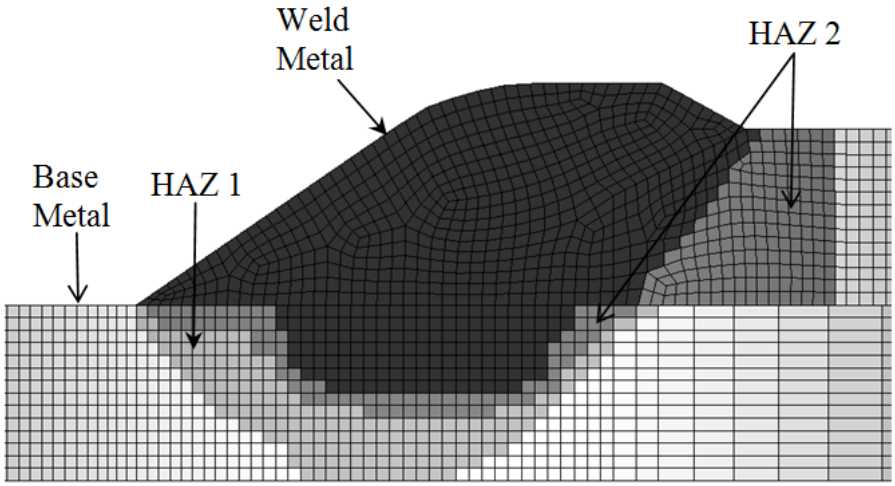

(b)

Figure 2.24. The finite element meshes near the weld for (a) the generic short weld model and (b) the generic long weld model with the different material sections.

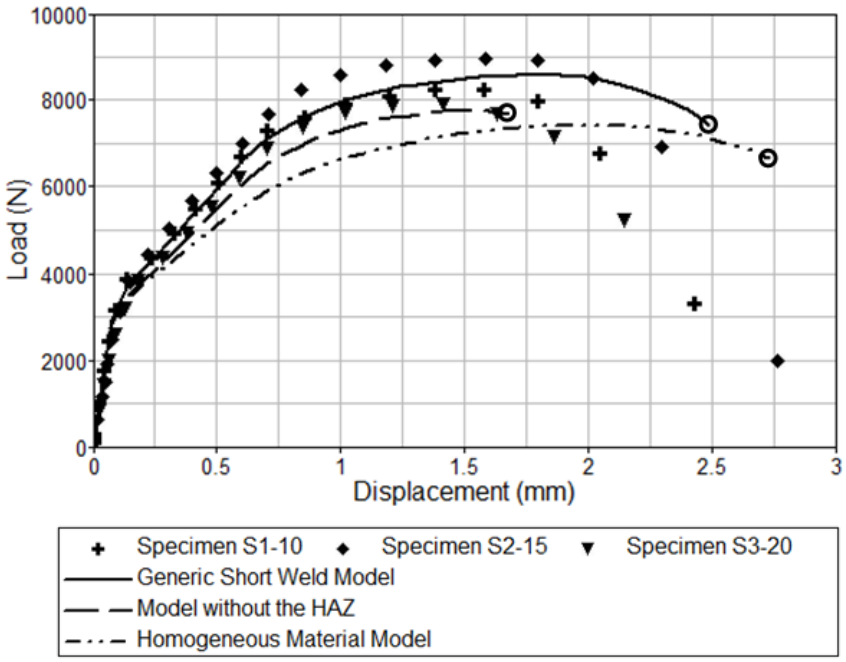

Figure 2.25. The load-displacement curves from the finite element analyses based on the generic short weld model, the homogeneous material model, and the model without the heat affected zone.

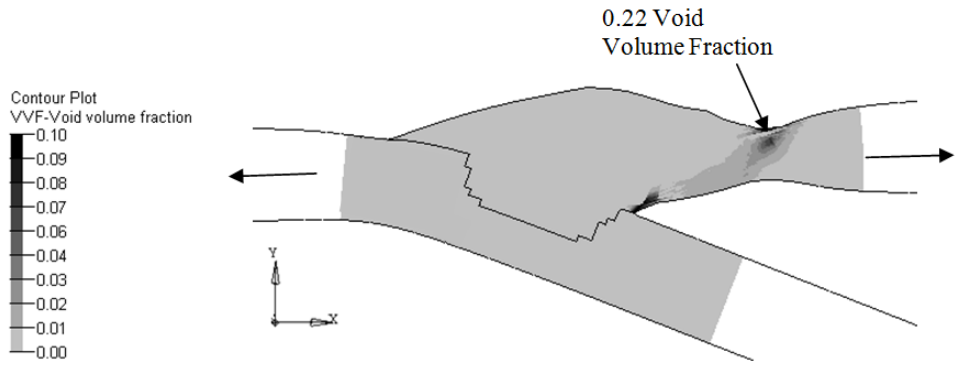

(a)

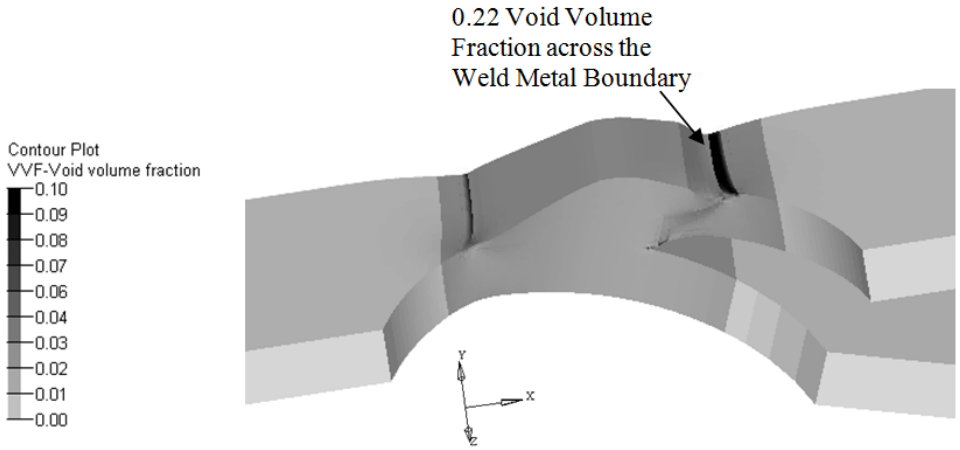

(b)

Figure 2.26. The distributions of the void volume fraction near the weld at (a) the mid-section of the specimen for the homogeneous material model and on (b) the top and outside surfaces of the specimen for the model without consideration of the heat affected zone.

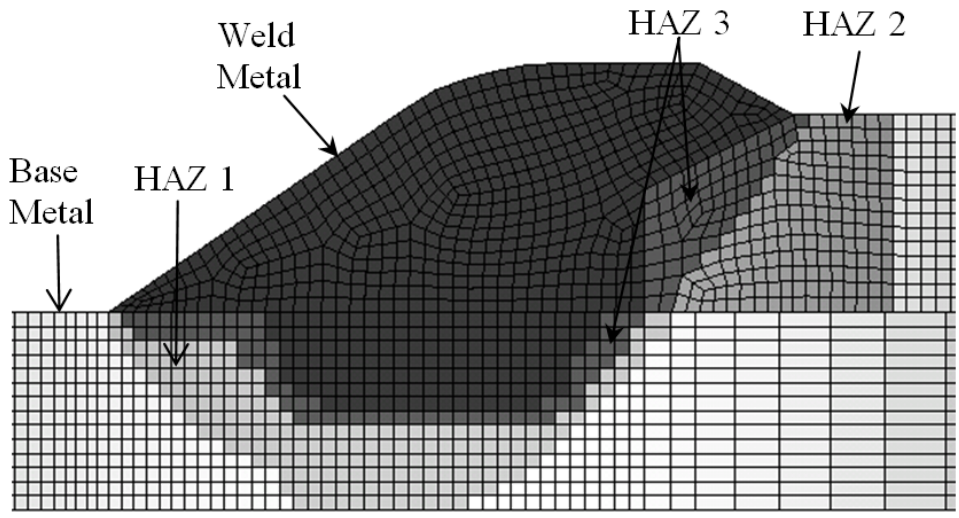

(a)

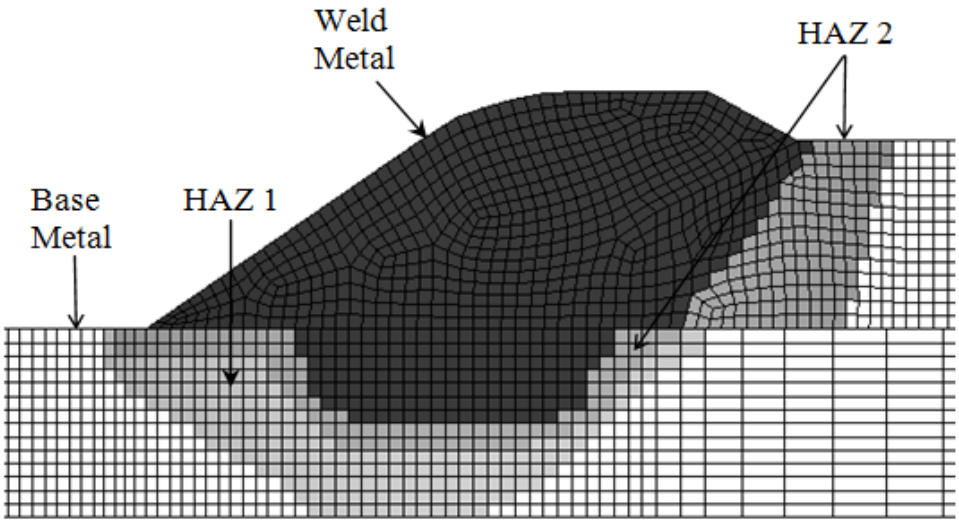

(b)

Figure 2.27. (a) The finite element mesh near the weld for the generic short weld model with the modified heat affected zone. (b) The finite element mesh near the weld for the generic long weld model with the modified heat affected zone.

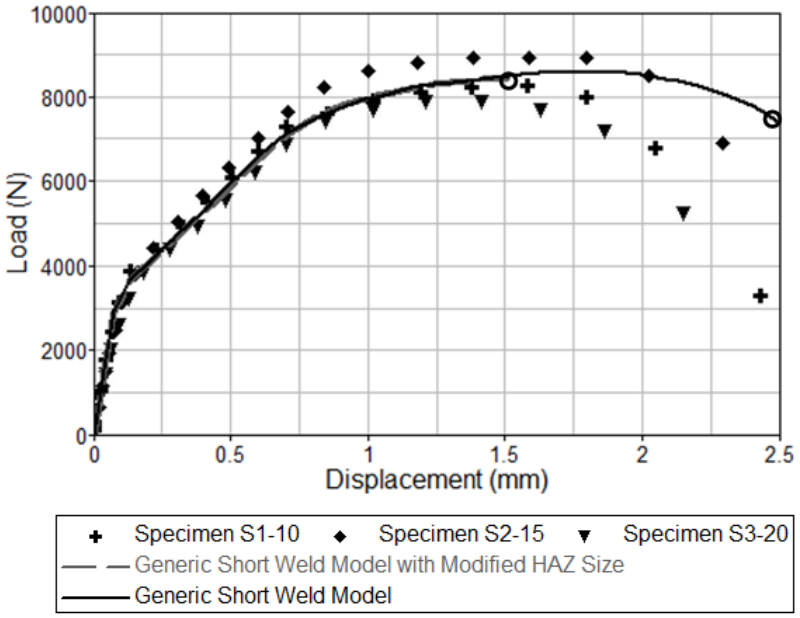

(a)

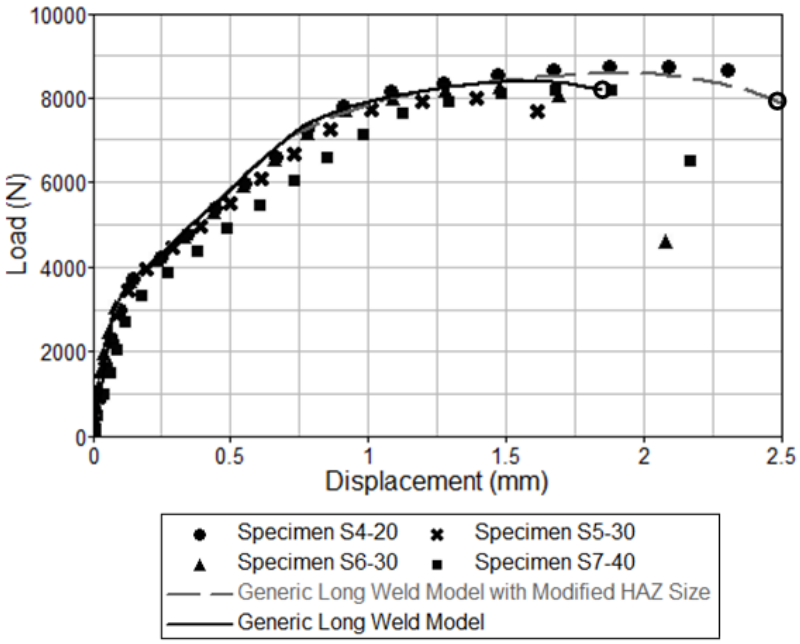

(b)

Figure 2.28. The load-displacement curves from the finite element analyses of the models with and without the modified heat affected zone geometry for (a) the generic short weld model and (b) the generic long weld model.

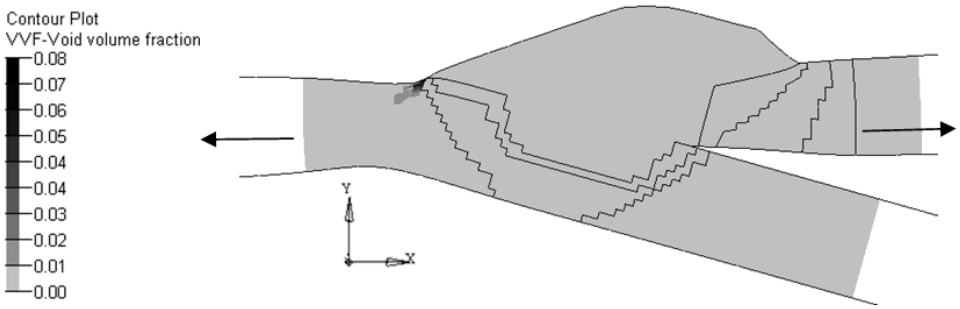

(a)

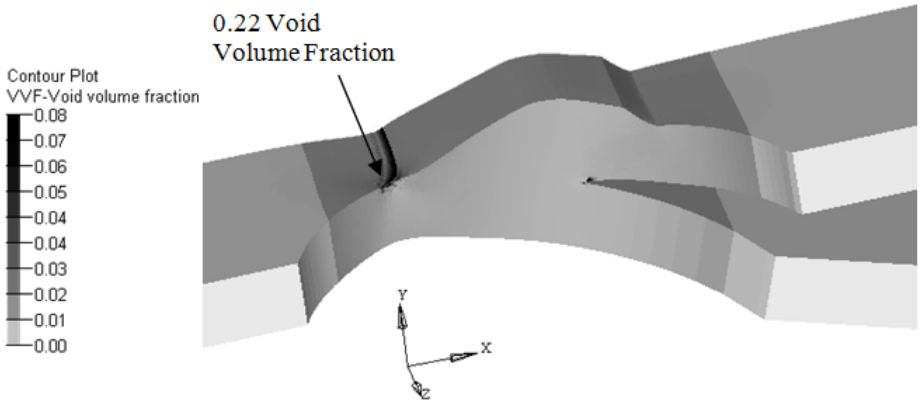

(b)

Figure 2.29. The distributions of the void volume fraction near the weld at (a) the mid-section of the specimen and on (b) the top and outside surfaces of the specimen for the generic short weld model with the modified heat affected zone geometry.

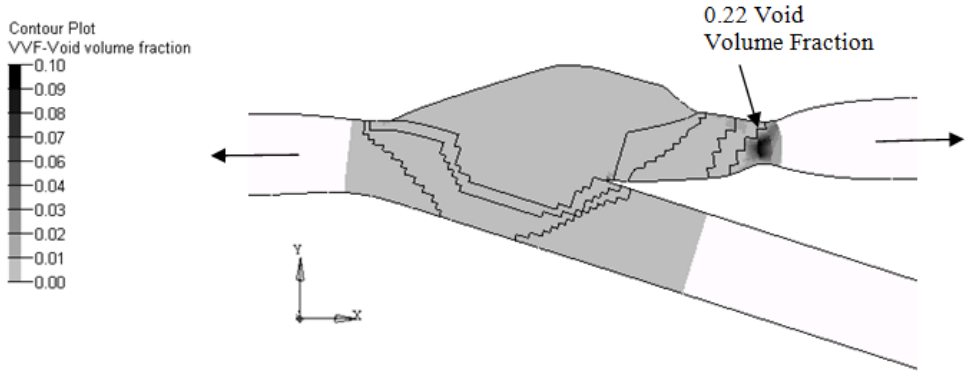

(a)

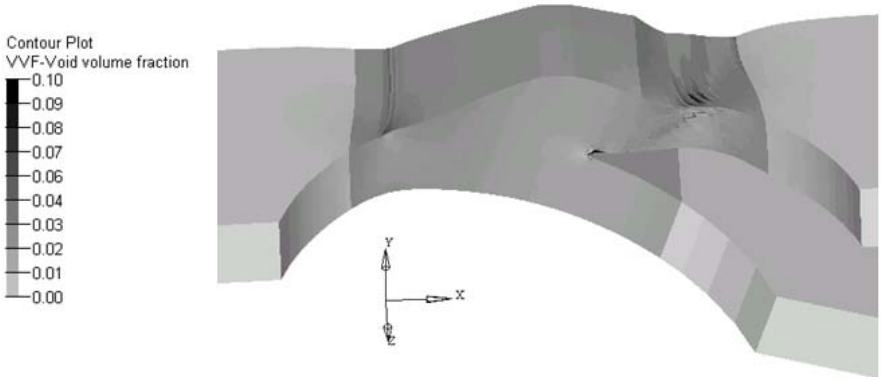

(b)

Figure 2.30. The distributions of the void volume fraction near the weld at (a) the mid-section of the specimen and on (b) the top and outside surfaces of the specimen for the generic long weld model with the modified heat affected zone geometry.

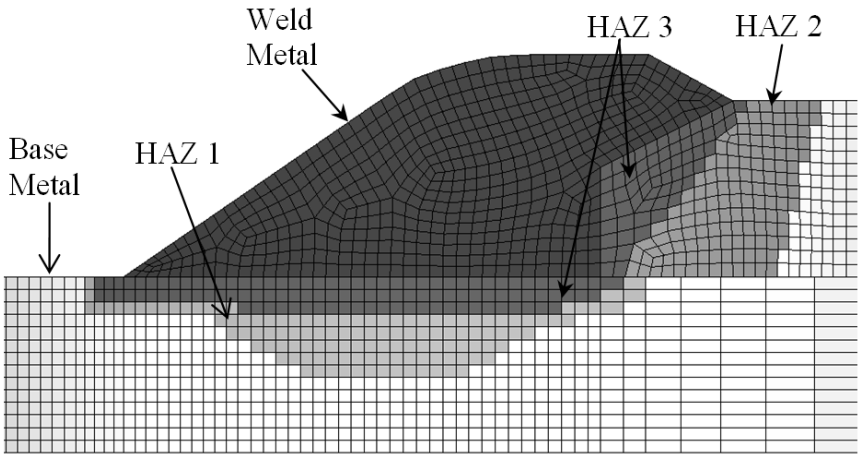

(a)

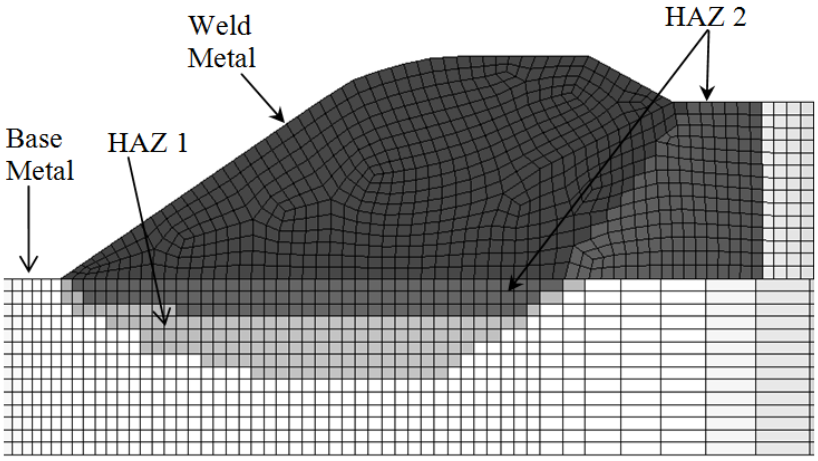

(b)

Figure 2.31. The modification made to the amount of weld penetration for (a) the generic short weld model and (b) the generic long weld model.

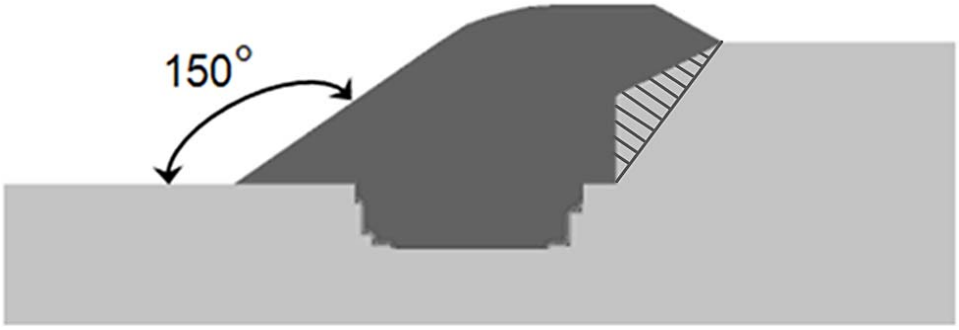

(a)

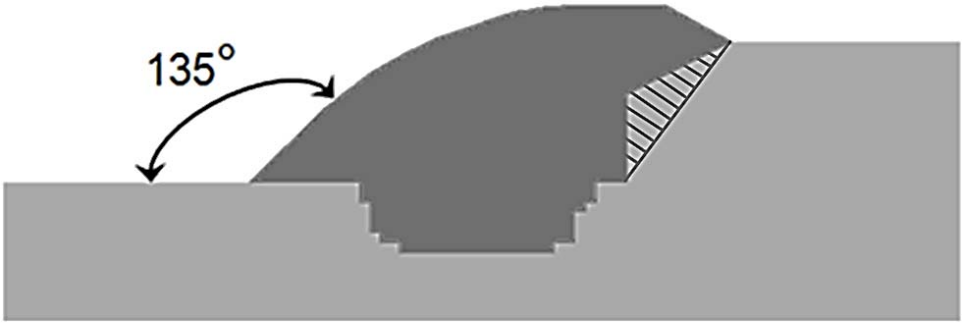

(b)

Figure 2.32. The generic finite element models with (a) the unmodified toe angle and (b) with the modified toe angle.

Chapter 3
Analytical and Computational Stress Intensity Factor Solutions for Gas Metal Arc Welds in Lap-Shear Specimens

3.1. Introduction

Recently, many investigations on quasi-static and fatigue strengths of gas metal arc welded joints have been conducted. Investigators have reported failure locations near weld roots and near weld toes under quasi-static and cyclic loading conditions [1-11]. In most investigations, the end effects of the discontinuous welds were excluded and the failures at the mid-sections of the welds were studied. Bonnen et al. [10] included the weld ends in some single lap-shear specimens in order to understand the effects of the weld ends on the cyclic loading performance. Under cyclic loading conditions, the failure mode of the single lap-shear specimens with the weld ends excluded was mainly near the weld toe under low load levels and mainly near the weld root under higher load levels. However, the failure mode of the single lap-shear discontinuous weld specimens with the weld ends included was mainly due to fatigue crack propagation from the pre-existing crack at the interfacial plane of the two sheets near the root of the weld through the weld throat.

Weld geometry is one of the key factors affecting the cyclic loading performance of gas metal arc weld joints [7]. Niu and Glinka [12] investigated the effect of weld geometry on the stress intensity factor solutions for welded T-butt joints under a variety

of loading conditions. Nguyen and Wahab [13] examined the effect of weld geometry and residual stresses on the fatigue life of butt welded joints based on the stress intensity factor solutions. Feng et al. [11] developed a fatigue life prediction model with the consideration of the crack initiation life at the weld toe, which was estimated using the notch strain approach, and the crack propagation life at the weld toe based on the stress intensity factor solution for cracks. Cerit et al. [14] investigated the effects of the weld geometry on the stress intensity factor solutions in cylindrical fillet-welded joints.

In this chapter, the mode I and mode II stress intensity factor solutions for the pre-existing cracks near gas metal arc welds in lap-shear specimens are investigated. Analytical stress intensity factor solutions for the welds in lap-shear specimens with idealized weld geometries were derived based on the beam bending theory. Two-dimensional, plane strain finite element analyses were carried out in order to obtain the computational stress intensity factor solutions for the realistic and idealized weld geometries. The computational solutions are compared with the analytical solutions based on the beam bending theory. Further finite element analyses were carried out in order to obtain the computational stress intensity factor solutions for the realistic weld geometries with dissimilar sheet thicknesses. In addition, the distribution of the stress intensity factor solutions for continuous idealized welds and discontinuous idealized welds were obtained by three-dimensional finite element analyses.

3.2. Specimens

The lap-shear specimens examined in Amodeo et al. [1] are studied in this investigation. Lap-shear specimens of HSLA steel sheets with a thickness t of 2.0 mm were robot welded together using the gas metal arc welding process. 60 mm wide sheet specimens with the weld lengths varying from 10 mm to 40 mm were made. The welds were centered on the sheets. Some of these specimens are shown in Figure 3.1.

For the finite element analyses in this investigation, the cross sectional geometry of the weld metal used to represent a realistic weld was designed to match the micrograph of the cross section of a specimen with a weld length of 25 mm as shown in Figure 3.2. The specimen has the sheet thickness of 2.0 mm. The pre-existing crack tip at the interfacial plane of the two sheets near the root of the weld is labeled in the figure.

3.3. Analytical stress intensity factor solutions

The elastic beam bending theory is adopted here in order to derive the analytical stress intensity factor solutions for welds with an idealized geometry as in Sripichai et al. [15]. A schematic of a lap-shear specimen near a realistic weld is shown in Figure 3.3(a) where the shaded area represents the weld metal. Both the upper and lower sheets have the same thickness t. The weld width is represented by w in the figure. The geometry of the weld shown in Figure 3.3(a) is idealized to a square shape that represents two joined beams as shown in Figure 3.3(b). The protrusion and shape of the weld metal, as shown in Figure 3.3(a), are not considered in the derivation of the analytical solutions in this study. As shown in Figures 3.3(a) and 3.3(b), F/b represents the lap-shear force per

unit weld length applied along the interfacial surface. The weld metal is assumed to have the same elastic properties as those of the base metal.

For linear elastic materials, the stress intensity factor solutions can be derived from the elastic energy release rate G. Under plane strain conditions, the relationship between the elastic energy release rate and the stress intensity factors can be expressed as

$$G = \frac{K_I^2 + K_{II}^2}{E'} \tag{3.1}$$

where $E' = E/(1-\nu^2)$. Here, E is Young's modulus and ν is Poisson's ratio.

For linear elastic materials under displacement controlled conditions, the decrease of the potential energy, $d\Pi$, of the system can be expressed as

$$-d\Pi = dU \tag{3.2}$$

where dU is the increase of the elastic strain energy of the system. The energy release rate is the decrease of the potential energy per unit crack extension. Therefore, for any crack extension, da, the energy release rate G can be expressed as

$$G = \frac{-d\Pi}{da} \tag{3.3}$$

Combining equations (3.1), (3.2) and (3.3) gives

$$\frac{dU}{da} = \frac{K_I^2 + K_{II}^2}{E'} \tag{3.4}$$

Figure 3.4(a) shows a schematic of a lap-shear specimen near the idealized weld. The lap-shear load can be represented by the equivalent load shown in Figure 3.4(b). As in Sripichai et al. [15], the equivalent lap-shear load shown in Figure 3.4(b) can be decomposed into four different loads. Figures 3.4(c-f) schematically show the four decomposed loads: counter bending (Figure 3.4(c)), central bending (Figure 3.4(d)),

tension loading (Figure 3.4(e)), and in-plane shear loading (Figure 3.4(f)). Here the weld width w is assumed to be much larger than the sheet thickness t.

Three types of loading conditions shown in Figures 3.4(c), 3.4(d), and 3.4(f) give different opening and shear modes of the crack. The counter bending loading condition gives mode I (opening mode) loading to the crack while the central bending and in-plane shear loading conditions give mode II (in-plane shear mode) loading to the crack. Thus, the K_I solution can be derived from the two beams under counter bending conditions (Figure 3.4(c)), while the K_{II} solution can be derived from the two beams under central bending and in-plane shear loading conditions (Figures 3.4(d) and 3.4(f)). Note that the tension load (Figure 3.4(e)) does not give any stress intensity factor to the crack.

Figure 3.4(c) shows the two-beam model under counter bending. The bending moments per unit width, $Ft/4b$, are applied at the far right ends of the beams. For the counter bending, the increase of the elastic strain energy can be expressed as

$$dU = \frac{3}{4}\frac{F^2}{E'b^2t}da \tag{3.5}$$

Combining equations (3.4) and (3.5) with $K_{II} = 0$ gives the K_I solution under counter bending conditions as

$$K_I^C = \frac{\sqrt{3}}{2}\frac{F}{b\sqrt{t}} \tag{3.6}$$

Figure 3.4(d) shows the two-beam model under central bending. The bending moments per unit width, $Ft/4b$, are applied at the far right ends of the beams. These bending moments cause a bending moment per unit width, $Ft/2b$, at the far left end of the two beam model. The increase of the elastic strain energy can be expressed as

$$dU = \left(\frac{3}{4} \frac{F^2}{E'b^2t} - \frac{3}{16} \frac{F^2}{E'b^2t} \right) da \tag{3.7}$$

Combining equations (3.4) and (3.7) with $K_I = 0$ gives the K_{II} solution under central bending as

$$K_{II}^{CB} = \frac{3}{4} \frac{F}{b\sqrt{t}} \tag{3.8}$$

Figure 3.4(f) shows the two-beam model under in-plane shear. The membrane forces per unit width, $F/2b$, are applied at the far right ends of the beams. These forces cause a bending moment per unit width, $Ft/2b$, at the far left end of the two beam model. The increase of the elastic strain energy can be expressed as

$$dU = \left(\frac{1}{4} \frac{F^2}{E'b^2t} - \frac{3}{16} \frac{F^2}{E'b^2t} \right) da \tag{3.9}$$

Combining equations (3.4) and (3.9) with $K_I = 0$ gives the K_{II} solution under in-plane shear as

$$K_{II}^{S} = \frac{1}{4} \frac{F}{b\sqrt{t}} \tag{3.10}$$

With the superposition principle of linear elasticity, the analytical stress intensity factor solutions for the lap-shear specimen can be expressed as

$$K_I = \frac{\sqrt{3}}{2} \frac{F}{b\sqrt{t}} \tag{3.11}$$

and

$$K_{II} = \frac{F}{b\sqrt{t}} \tag{3.12}$$

3.4. Finite element analysis

Two-dimensional, plane strain finite element analyses were carried out in order to obtain the computational stress intensity factor solutions for the pre-existing cracks between the upper and lower sheets near the roots of the welds with realistic weld geometries. Figure 3.5(a) shows a schematic of a two-dimensional finite element model of a lap-shear specimen. The specimen has the upper sheet thickness t_u, lower sheet thickness t_l, overlap length g, weld width w, weld height h, and weld toe angle, θ. For analyses in which both the upper sheet and the lower sheet have the same thickness no subscript is used and the sheet thickness is denoted as t. The coordinate system is shown in the figure. The left edge has a fixed displacement condition at the upper surface while the right edge has a concentrated force per unit width, F/b, applied at the lower surface in the +x direction.

Computations are performed using the commercial finite element code ABAQUS Standard v611 [16]. The weld metal, heat affected zone, and base metal are assumed to be linear elastic with Young's modulus E = 207 GPa and Poisson's ratio ν = 0.3. Second-order, continuum, plane strain elements (CPE8) are used in the models. Figure 3.6(a) shows the mesh near the weld. The element size near the weld is about 150 μm. Figure 3.6(b) shows the mesh near the pre-existing crack tip near the root of the weld. A finer mesh is used near the pre-existing crack tip with the element size of 10 μm closest to the crack tip.

The two-dimensional plane strain finite element model has the overlap length g = 13.4 mm, the weld width w = 5.29 mm, the weld height h = 0.53 mm, and the toe angle

θ = 145°. In order to obtain the stress intensity factor solutions for various realistic weld geometries, the sheet thickness in the finite element model was varied while keeping the overlap length, the weld width, the weld height, and the weld toe angle constant. Figure 3.7 shows the meshes near the welds for the finite element models for the specimens with the 1.5 mm, 2.0 mm, and 2.5 mm sheet thicknesses for both the upper and lower sheets.

For comparison, finite element analyses were carried out in order to obtain the computational stress intensity factor solutions for the idealized welds. A schematic of a two-dimensional finite element model of a weld with idealized weld geometry is shown in Figure 3.5(b). Here, the weld toe angle is 90° and the weld height is 0. The remaining parameters are kept the same as in the finite element models of the welds with the realistic weld geometries.

3.5. Computational stress intensity factor solutions

Table 3.1 shows the normalized computational stress intensity factor solutions, $\overline{K}_I$ and $\overline{K}_{II}$, for the idealized and realistic weld geometries with equal upper and lower sheet thickness t. All solutions shown in the table are normalized by the K_{II} solution based on the beam bending theory in equation (12). As shown in Table 3.1, the normalized computational solutions for the idealized geometry match the analytical solutions for the given ratios of w/t well. The $\overline{K}_I$ and $\overline{K}_{II}$ solutions for the larger sheet thicknesses deviate slightly from the analytical solutions due to the lower value of w/t. The analytical solutions are derived from beam bending theory with the assumption that the weld width is much larger than the sheet thickness. These results support Sripichai et

al. [1515] who showed for laser welds when $w/t \geq 4$, the computational $\overline{K}_I$ solution is equal to the analytical solution and when $w/t \geq 2$, the computational $\overline{K}_{II}$ solution is equal to the analytical solution.

The normalized computational stress intensity factor solutions for the realistic weld geometry can be compared with the solutions for the idealized weld geometry. Table 3.1 shows the weld geometry effect on the stress intensity factors solutions. The computational results indicate that the idealized geometry with a toe angle of 90° and with no weld height over estimates the stress intensity factor solutions. Table 3.1 also shows small variation in the stress intensity factor solutions for the different ratios of w/t investigated in this study.

The values for the normalized equivalent stress intensity factor, $\overline{K}_e$ are calculated from the mode I and mode II stress intensity factor solutions in Table 3.1. The equivalent stress intensity factor under mixed mode loading conditions, K_e, can be defined as

$$K_e = \sqrt{K_I^{\,2} + K_{II}^{\,2}} \tag{3.13}$$

The normalized equivalent stress intensity factor solution can be used for estimation of fatigue lives in a fatigue crack growth model under mixed mode loading conditions (Asim et al. [17]).

Additional finite element analyses were carried out in order to obtain the computational stress intensity factor solutions for realistic welds with dissimilar sheet thicknesses. Lai et al. [18] presented the stress intensity factor solutions between two similar and dissimilar sheets with different thicknesses under plane strain conditions for ultrasonic welds. As presented in [18], the stress intensity factor solutions for welds

joining sheets of identical materials with dissimilar sheet thicknesses can be written in the normalized forms as

$$\overline{K}_{I}^{d} = k_I(\delta)\frac{F}{b\sqrt{t_u}} \tag{3.14}$$

$$\overline{K}_{II}^{d} = k_{II}(\delta)\frac{F}{b\sqrt{t_u}} \tag{3.15}$$

and

$$\overline{K}_{e}^{d} = k_e(\delta)\frac{F}{b\sqrt{t_u}} \tag{3.16}$$

where k_I, k_{II}, and k_e are the dimensionless geometric functions for a given δ. Here, δ is the ratio of the upper sheet thickness to the lower sheet thickness as

$$\delta = t_u / t_l \tag{3.17}$$

In this investigation, the thickness ratios modeled ranged from 0.2 to 5.0. The upper sheet thickness t_u is kept at 2.0 mm for the different thickness ratios. The selection of the geometries appears to be reasonable for δ less than 1. However, for completeness several values of δ larger than 1 are selected. Since there is only a small variation in the stress intensity factor solutions with the different ratios of w/t, the weld width w is kept at 5.29 mm for the different thickness ratios.

Figure 3.8 shows the dimensionless geometric functions k_I, k_{II}, and k_e as functions of the thickness ratio δ from the finite element analyses. As shown in the figure, the thickness ratio δ can have significant effects on the stress intensity factor solutions and their mode mixities. It should be noted that, the normalized equivalent stress intensity factor solution can be used for estimation of fatigue lives in a fatigue

crack growth model under mixed mode loading conditions for gas metal arc welds with dissimilar sheet thicknesses.

3.6. Discussions

The results of the two-dimensional finite element analyses show that the weld geometry and the thickness ratio can have significant effects on the stress intensity factors solutions. The computational results indicate that for the idealized weld geometry the analytical stress intensity factor solutions overestimates the solutions for the realistic weld geometry. The stress intensity factor solutions for realistic welds presented in this chapter can be used in engineering application under mixed mode loading conditions. When the sheet thickness is large, the necking mechanism as examined by Asim et al. [17] and Amodeo et al. [11] will not be the dominant failure mechanism. The fracture toughness of the HAZ or weld metal can be reached prior to necking. As indicated by Bonnen et al. [10] for discontinuous welds under cyclic loading, the crack initiation can occur at the pre-existing crack tip and, consequently, the stress intensity factor solutions can be used to estimate the fatigue lives.

Three-dimensional finite element analyses were conducted in order to investigate the trends in the stress intensity factor solutions for a continuous weld specimen and for a discontinuous weld specimen. The mesh density used in the model was kept the same as that from the two-dimensional plane strain finite element model with the idealized weld geometry and the sheet thickness of 2.0 mm. First-order, continuum, hexahedral elements (C3D8) were used. The weld length was modeled as 22.5 mm for the

continuous weld specimen. For the discontinuous weld specimen, the weld length was modeled as 22.5 mm and the total specimen width was 33.75 mm. The weld was modeled as centered on the specimen. The finite element models near the weld for the continuous and discontinuous welds are shown in Figures 3.9(a) and 3.9(b), respectively.

The contact between the top and bottom sheets was defined in the discontinuous weld model in order to include the effects of the force which separate the top and bottom sheets. Since the contact area will change with the load amplitude, the stress intensity factor solutions are not linearly scalable with the applied load. For the discontinuous weld model, a load large enough for a full contact area was applied. The linear scalability of the stress intensity factor solutions at applied loads large enough for a full contact area was verified by applying a load of 1000 N and comparing the results with those from the model with an applied load of 100 N. There was negligible difference in the normalized results at these two applied loads. However, the reader is cautioned that at lower load levels, the stress intensity factor solutions will be different from those presented here for discontinuous welds.

The stress intensity factor solutions for the continuous and discontinuous weld specimens were obtained from the three-dimensional models. The stress intensity factor solutions are normalized by the K_{II} solution for the continuous weld based on the beam bending theory in equation (12). The normalized mode I and mode II stress intensity factor solutions are plotted in Figures 3.10(a) and 3.10(b), respectively. In the figures, the stress intensity factor solutions are plotted along the crack length where 0 is located at the mid-section of the weld. The average stress intensity factor solutions for the

continuous weld are also shown in the figures as open circles. The average stress intensity factor solutions match the analytical solutions given in Table 3.1 well [19].

Figures 3.10(a) and 3.10(b) show that the distributions of the mode I and mode II stress intensity factor solutions for the discontinuous weld are different from those for the continuous weld. The mode I stress intensity factor solution is highest at the mid-section of the weld for the continuous weld. For the discontinuous weld there is less variation in the mode I stress intensity factor solution. The mode II stress intensity factor solution is highest near the weld ends in the discontinuous weld. For the continuous weld there is less variation in the mode II stress intensity factor solution. The difference in the distribution of the equivalent stress intensity factor solution is shown in Figure 3.10(c).

In order to understand the effect of the contact between the top and bottom sheets on the stress intensity factor solutions, the three-dimensional model of the discontinuous weld was run without the contact defined. As shown in Figure 3.10(a), the distribution of the mode I stress intensity factor solution for the discontinuous weld model without contact is similar to the distribution of the mode I stress intensity factor solution for the continuous weld. The magnitude of the mode I stress intensity factor solution for the discontinuous weld model without contact is slightly lower than that for the continuous weld model. As shown in Figure 3.10(b), the distribution of the mode II stress intensity factor solution for the discontinuous weld model without contact is similar to the distribution of the mode II stress intensity factor solution of the discontinuous weld with the contact modeled. The magnitude of the mode II stress intensity factor solution for the discontinuous weld model without contact is slightly higher than that for the discontinuous weld model with the contact modeled.

For the automotive industry, the performance of discontinuous gas metal arc welded joints is of significant interest. By minimizing the length of the discontinuous welds, significant cost savings can be gained due to reduced cycle time and reduced usage of equipment and consumables. In order to investigate the effect of the weld length on the stress intensity factor solutions, additional three dimensional finite element analyses were run with the weld length reduced to 7.5 mm. For the discontinuous weld specimen, the weld length was modeled as 7.5 mm and the total specimen width was 15 mm. The normalized mode I and mode II stress intensity factor solutions are plotted in Figures 3.11(a) and 3.11(b), respectively. The normalized equivalent stress intensity factor solution is plotted in Figure 3.11(c). The average stress intensity factor solutions for the continuous weld are also shown in the figures as open circles and match the analytical solutions given in Table 3.1 well [19]. As shown in the figures, the trends in the distribution of the stress intensity factor solutions are the same as those for the long welds.

An initial investigation on the trends of the distribution of the stress intensity factor solutions for continuous and discontinuous welds was presented here. Further three-dimensional finite element computations should be conducted in order to assess the stress intensity factor solutions for discontinuous welds of various weld lengths. An examination of the stress intensity factor solutions for discontinuous welds in specimens with various ratios of the weld length to the specimen width is needed in order to minimize the length of the welds required for reliable design.

3.7. Conclusions

The mode I and mode II stress intensity factor solutions for the pre-existing cracks near gas metal arc welds in lap-shear specimens are investigated. Analytical stress intensity factor solutions for the welds in lap-shear specimens with idealized weld geometries were derived based on the beam bending theory. Two-dimensional, plane strain finite element analyses were carried out in order to obtain the computational stress intensity factor solutions for the realistic and idealized weld geometries. The normalized computational stress intensity factor solutions for the idealized weld geometry match the analytical solutions well. The finite element computations indicate that the stress intensity factor solutions for realistic gas metal arc welds are lower than the analytical solutions for the idealized weld geometry. Additional finite element analyses were carried out in order to obtain the computational stress intensity factor solutions for the realistic weld geometries with dissimilar sheet thicknesses. The results can be used for estimation of fatigue lives in a fatigue crack growth model under mixed mode loading conditions for gas metal arc welds with dissimilar sheet thicknesses. Finally, the stress intensity factor solutions for continuous welds and discontinuous welds were obtained by three-dimensional finite element analyses. The computational results indicate that the distributions of the mode I and mode II stress intensity factor solutions for the discontinuous weld are different from those for the continuous weld.

Acknowledgments

The support of this work by Johnson Controls Inc. is greatly appreciated. The encouragement and assistance of W. Randy Tighe and J. David Kotre of Johnson Controls is also appreciated.

References

1. Amodeo, C.M., Lai, W., Lee, J., Pan, J., “Failure Modes of Gas Metal Arc Welds in Lap-Shear Specimens of High Strength Low Alloy (HSLA) Steel,” Engineering Fracture Mechanics, Vol. 131, pp. 74-99, 2014.

2. Yan, B., Lalam, S.H., Zhu, H., "Performance Evaluation of GMAW Welds for Four Advanced High Strength Steels," SAE Technical Paper 2005-01-0904, Warrendale, PA, 2005.

3. Feng, Z., Carpenter, J.A., Sklad, P.S., "Characterization of Thermo-Mechanical Behaviors of Advanced High Strength Steels (AHSS): Task 2 - Weldability and Performance Evaluations of AHSS Parts for Automotive Structures," FY 2006 Progress Report, Automotive Lightweighting Materials, pp i206-i218, 2006.

4. Joaquin, A., Elliott, N.A., Jiang, C., Rajan, V., Hartman, D., and Karas, C., "Gas Metal Arc Welding of Advanced High Strength Steel - Developments for Optimized Welding Control and Weld Quality," SAE Technical Paper 2006-01-0300, Warrendale, PA, 2006.

5. Joaquin, A., Elliott, N.A., Jiang, C., Rajan, V., Hartman, D., and Karas, C., "Gas Metal Arc Welding of Coated Advanced High Strength Steel (AHSS) - Developments for Improved Weld Quality," SAE Technical Paper 2007-01-1360, Warrendale, PA, 2007.

6. Koganti, R., Angotti, S., Joaquin, A., Jiang, C., Karas, C., "Effect of Materials Stack-ups and Microhardness Distribution on Fatigue Performance of DP600 and Boron Steel GMAW Lap Joint," SAE Technical Paper 2007-01-1356, Warrendale, PA, 2007.

7. Koganti, R., Angotti, S., Joaquin, A., Jiang C., "Effect of Weld Geometry and HAZ Softening on Fatigue Performance of DP780 GMAW Lap Joint," SAE Technical Paper 2007-01-0632, Warrendale, PA, 2007.

8. Angotti, S., Koganti, R., Joaquin, A., Jiang, C., "Static and Fatigue Performance of Fusion Welded Uncoated DP780 Coach Joints," SAE Technical Paper 2008-01-0695, Warrendale, PA, 2008.

9. Kapustka, N., Conrardy, C., Babu, S., Albright, C., "Effect of GMAW Process and Material Conditions of DP 780 and TRIP 780 Welds," Supplement to the Welding Journal, Vo. 87, pp. 135-s - 148-s, 2008.

10. Bonnen J.J.F., Mandapati, R., Kang, H., Iyengar, R.M., Khosrovaneh, A.K., Amaya, M. A., Citrin, K., Shih, H. C., "Durability of Advanced High Strength Steel Gas Metal Arc Welds," SAE Technical Paper 2009-01-0257, Warrendale, PA, 2009.

11. Feng, Z., Sang, Y., Jiang, C., Chiang, J., Kuo, M., “Fatigue Performance of Advanced High-Strength Steels (AHSS) GMAW Joints,” SAE Technical Paper 2009-01-0256, Warrendale, PA, 2009.

12. Niu, X., Glinka, G., “The Weld Profile Effect on Stress Intensity Factors in Weldments,” International Journal of Fracture, Vol. 35, pp. 3-20, 1987.

13. Nguyen, T. N., Wahab, M.A., “The effect of Weld Geometry and Residual Stresses on the Fatigue of Welded Joints under Combined Loading,” Journal of Materials Processing Technology, Vol. 77, pp. 201-208, 1998.

14. Cerit, M., Hosgor, K., Ayhan, A.O., “Fracture Mechanics-Based Design and Reliability Assessment of Fillet Welded Cylindrical Joints Under Tension and Torsion Loading,” Engineering Fracture Mechanics, Vol. 116, pp. 69-79, 2014.

15. Sripichai, K., Asim, K., Pan, J., “Stress Intensity Factor Solutions for Estimation of Fatigue Lives of Laser Welds in Lap-Shear Specimens,” Engineering Fracture Mechanics, Vol. 78, pp. 1424-1440, 2010.

16. ABAQUS User's Manual, Dassault Systèmes Simulia Corp., Providence, RI, 2012.

17. Asim, K., Sripichai, K., Pan, J., “Fatigue Behavior of Laser Welds in Lap-Shear Specimens of High Strength Low Alloy Steel Sheets,” International Journal of Fatigue, Vol. 61, pp 283-296, 2013.

18. Lai, W.J., Pan J., “Graphical Stress Intensity Factor Solutions for Welds between Two Dissimilar Sheets with Different Thicknesses under Plane Strain Conditions,” submitted for publication. 2014.

19. Pook, L.P., “Approximate Stress Intensity Factors Obtained from Simple Plate Bending Theory,” Engineering Fracture Mechanics, Vol. 12, pp. 505-522, 1979.

Table 3.1. The normalized stress intensity factor solutions for idealized and realistic weld geometries.

	Analytical Solution	FEA Result Idealized Geometry			FEA Result Realistic Geometry		
t	--	1.50	2.00	2.50	1.50	2.00	2.50
w/t	--	3.53	2.65	2.11	3.53	2.65	2.11
$\overline{K}_I$	0.87	0.87	0.86	0.83	0.74	0.74	0.72
$\overline{K}_{II}$	1.00	1.00	1.00	1.00	0.85	0.88	0.91
$\overline{K}_e$	1.32	1.32	1.32	1.30	1.12	1.15	1.17

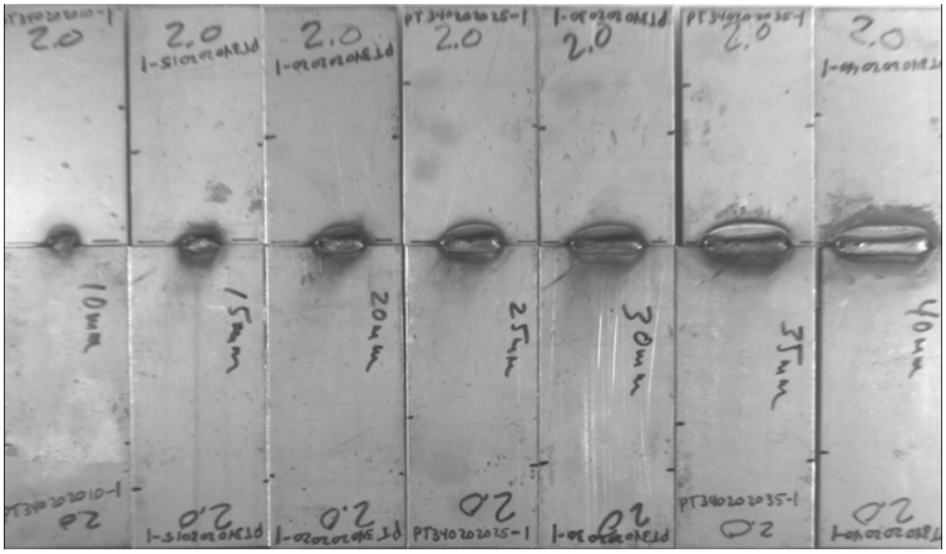

Figure 3.1. Wide lap-shear specimens with the weld length varying from 10 mm to 40 mm.

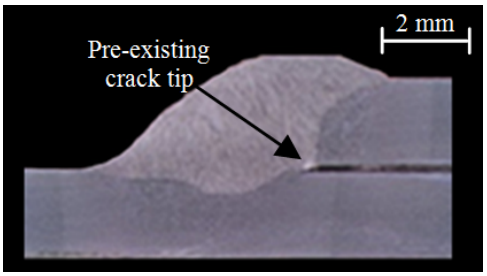

Figure 3.2. The micrograph of the cross section of a specimen with a weld length of 25 mm and a sheet thickness of 2.0 mm.

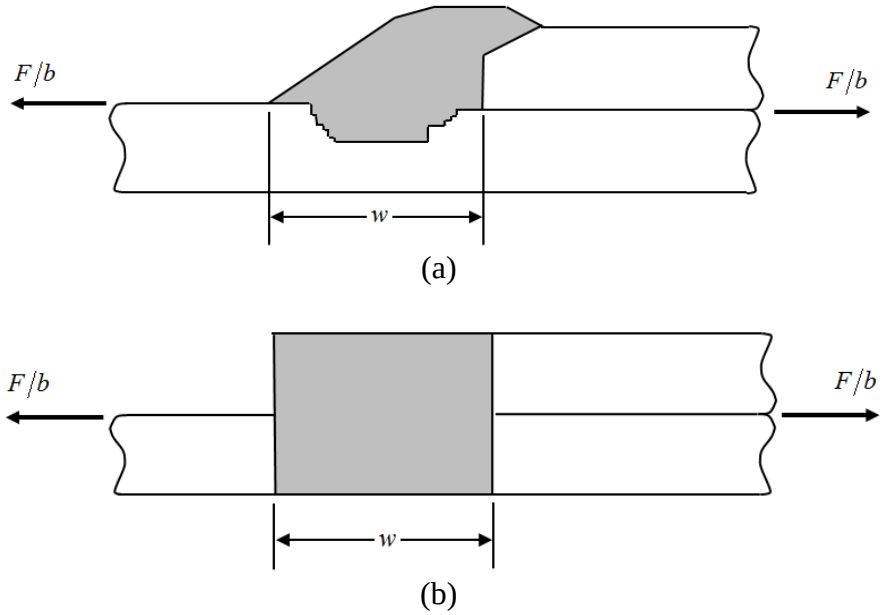

Figure 3.3. A schematic of a lap-shear specimen near (a) a realistic weld and (b) an idealized weld.

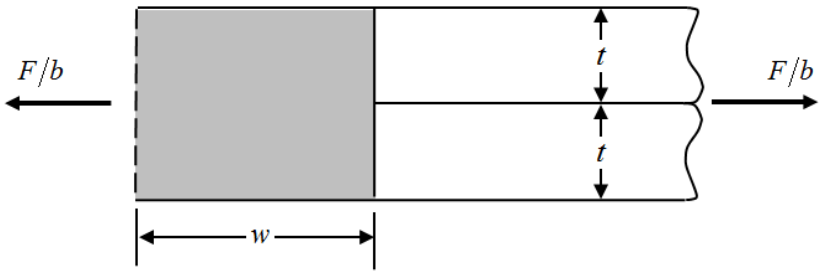

(a)

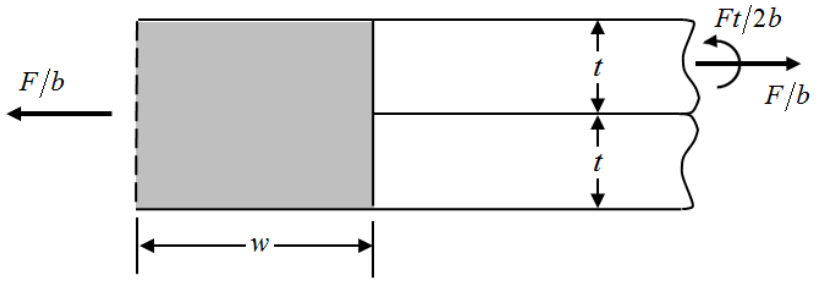

(b)

(c)

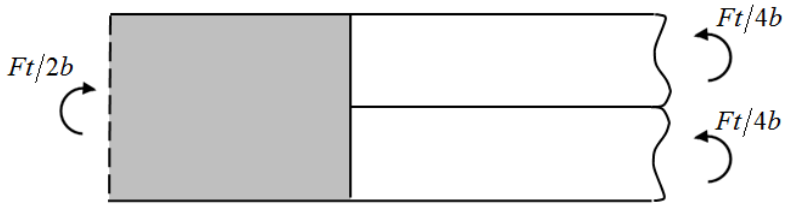

(d)

(e)

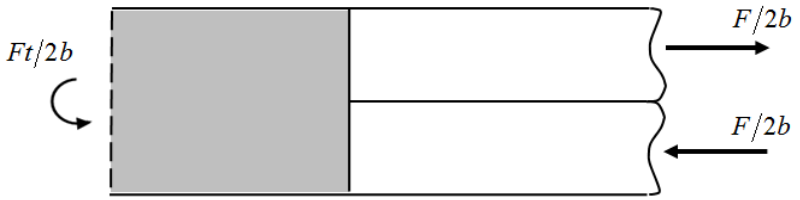

(f)

Figure 3.4. A two beam model is subjected to (a) the lap-shear load and (b) the equivalent lap-shear load. The equivalent lap-shear load shown in (b) is decomposed into (c) counter bending, (d) central bending, (e) tension, and (f) in-plane shear load.

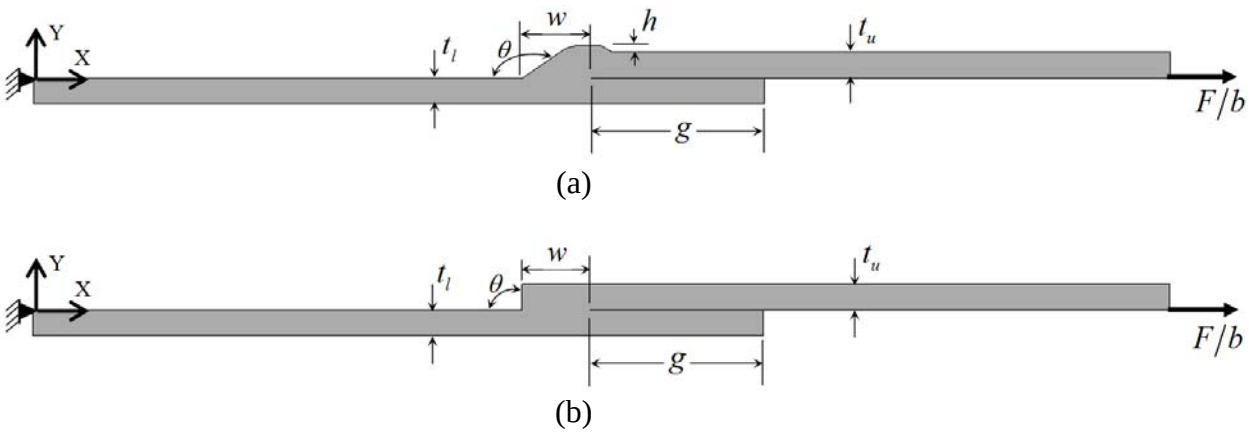

Figure 3.5. (a) A schematic of a two-dimensional finite element model of a lap-shear specimen with a realistic weld and the boundary conditions. (b) A schematic of a two-dimensional finite element model of a lap-shear specimen with an idealized weld and the boundary conditions.

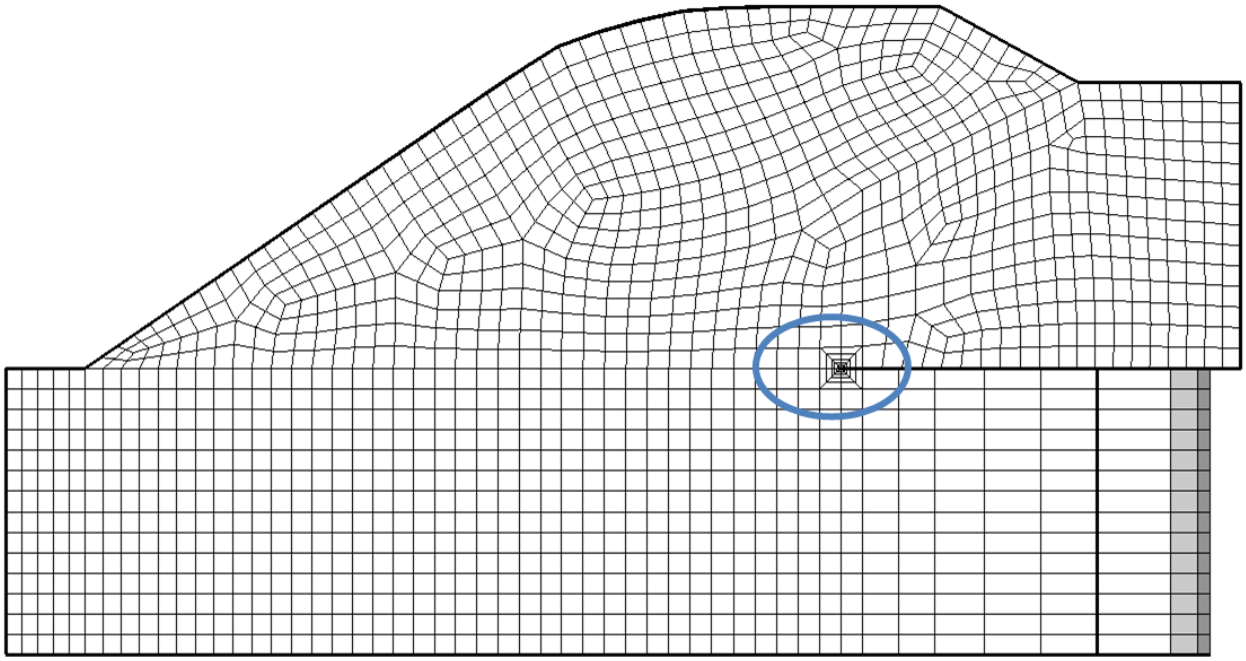

(a)

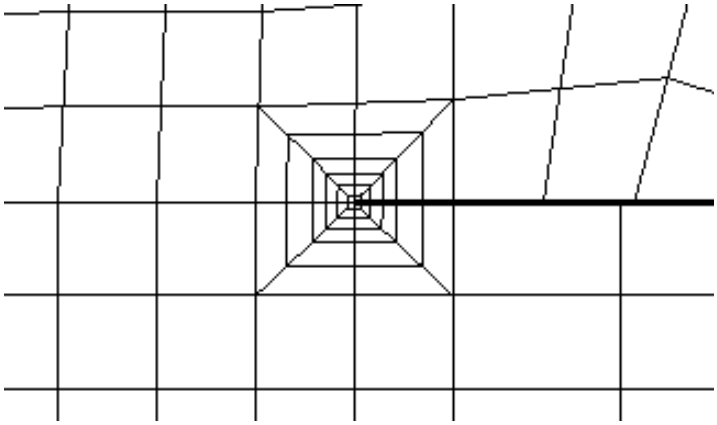

(b)

Figure 3.6. (a) The finite element mesh near the weld. (b) The finite element mesh near the pre-existing crack tip near the root of the weld.

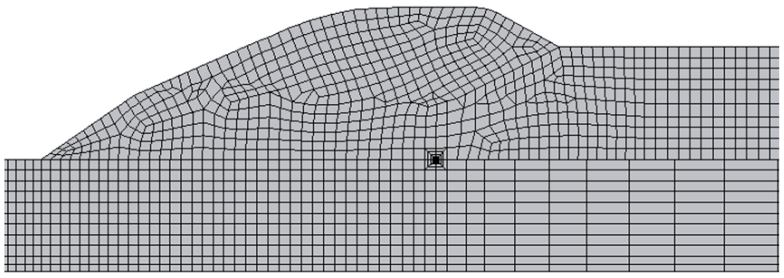

(a)

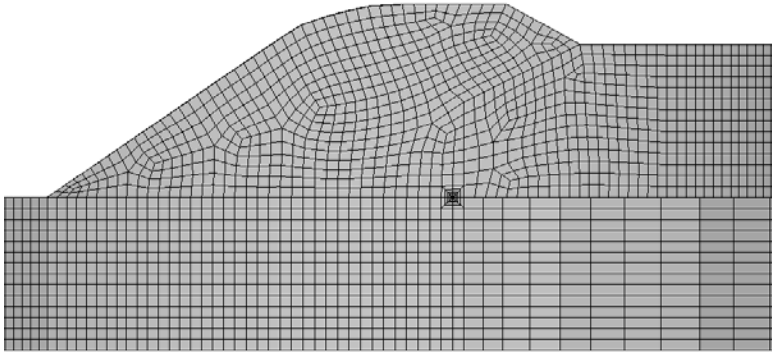

(b)

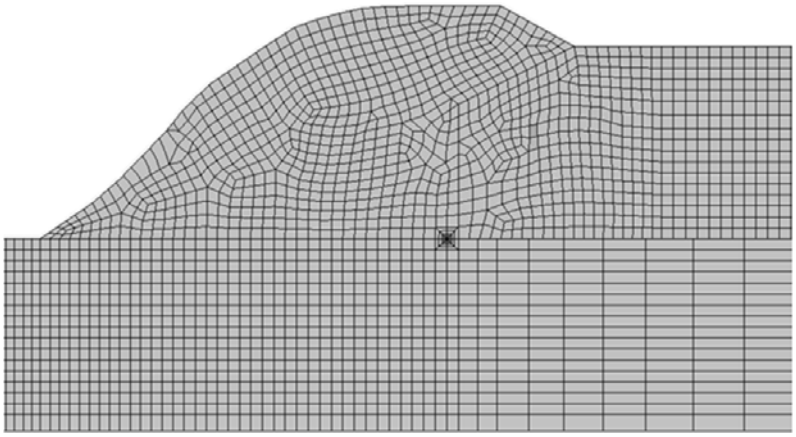

(c)

Figure 3.7. The finite element models for the specimens with the (a) 1.5 mm, (b) 2.0 mm, and (c) 2.5 mm sheet thicknesses.

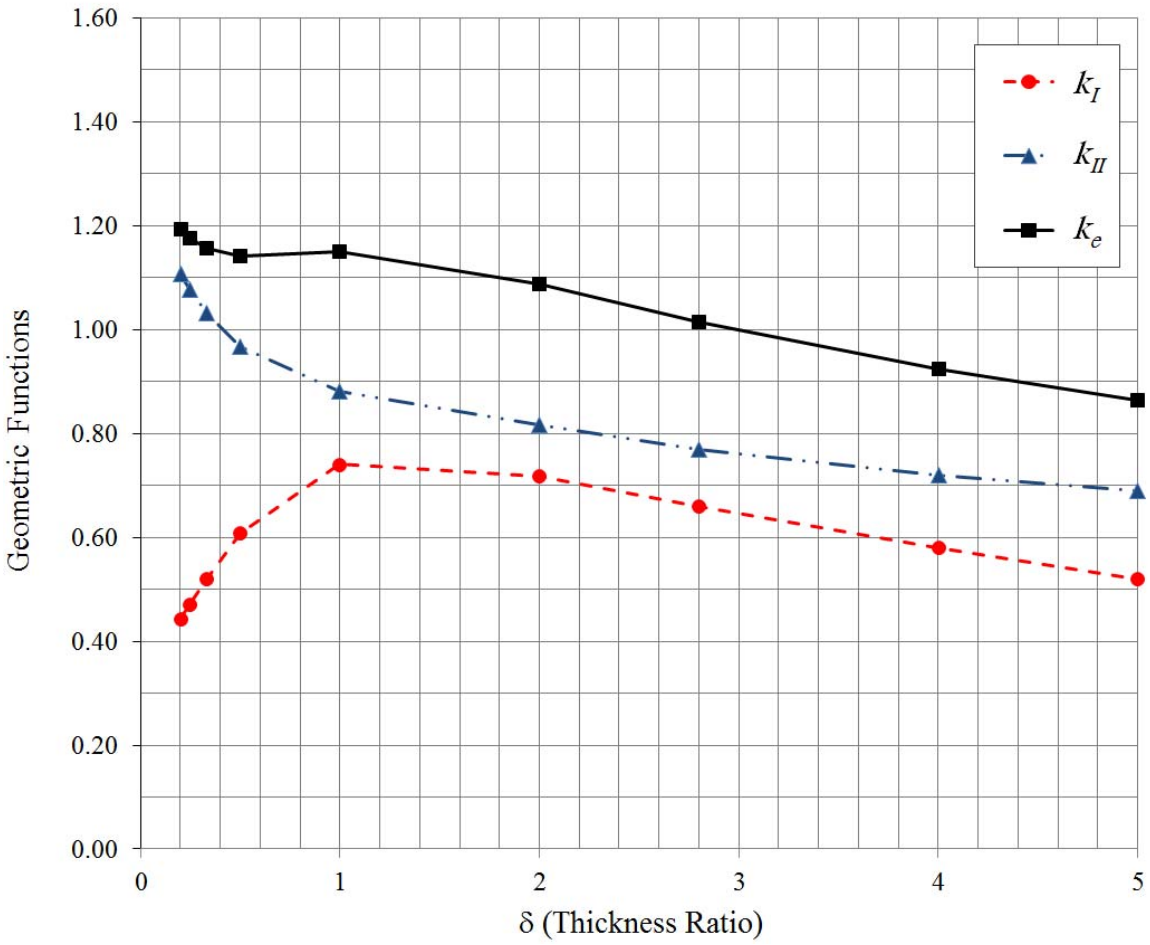

Figure 3.8. The dimensionless geometric functions k_I, k_{II}, and k_e as functions of the thickness ratio δ from the finite element analyses.

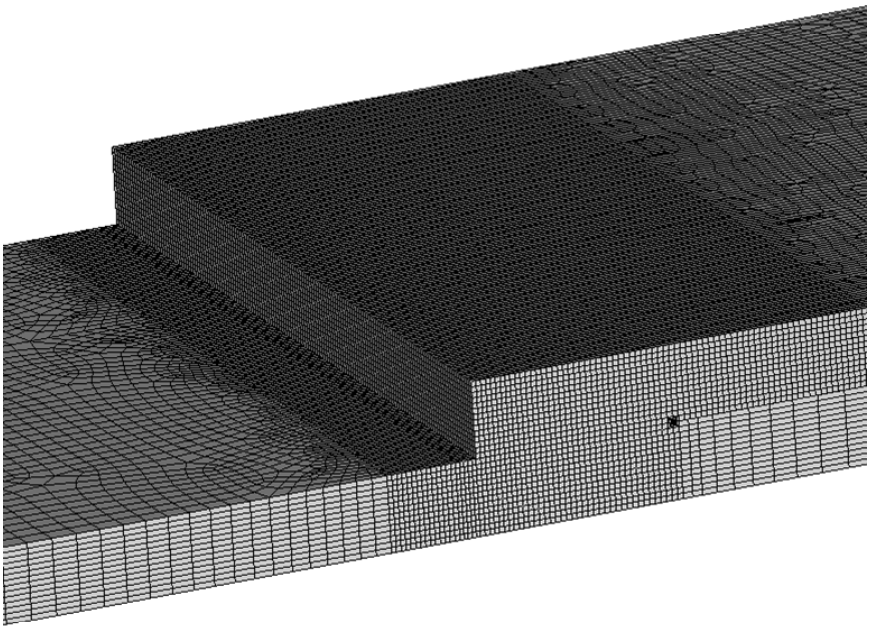

(a)

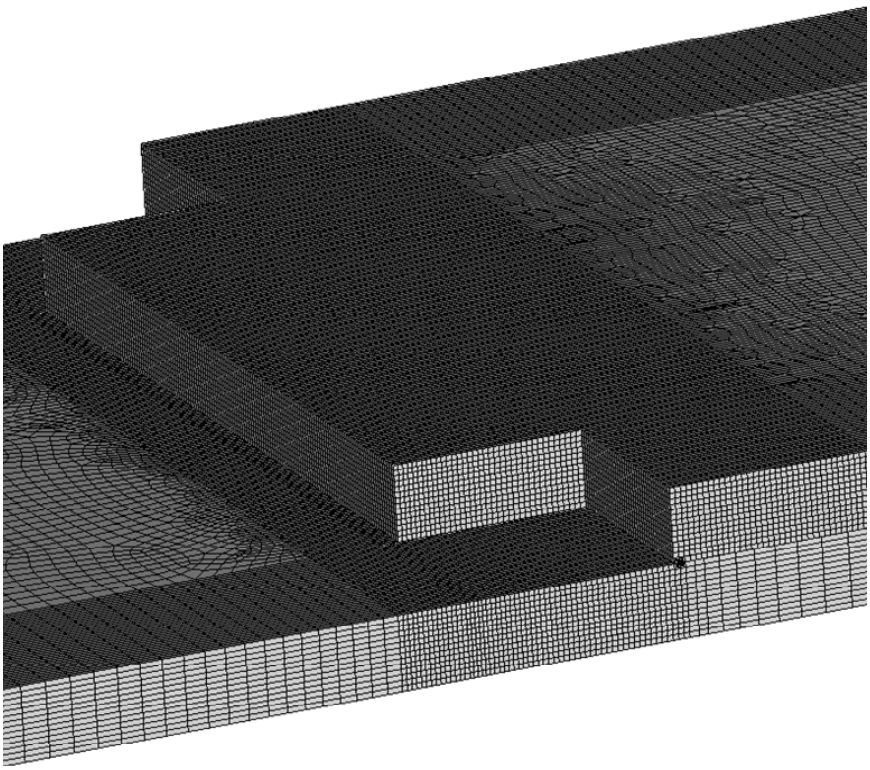

(b)

Figure 3.9. The finite element models near the weld for the (a) continuous and (b) discontinuous welds.

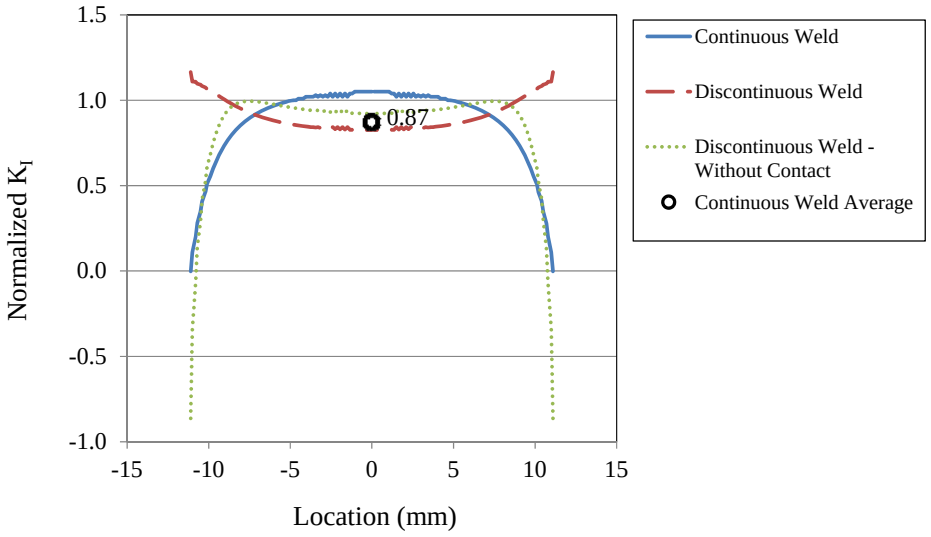
1.5
1.0
0.5
0.0
-0.5
-1.0
-15
-10
-5
0
5
10
15
Normalized K_I
Location (mm)
0.87
Continuous Weld
Discontinuous Weld
Discontinuous Weld - Without Contact
Continuous Weld Average

(a)

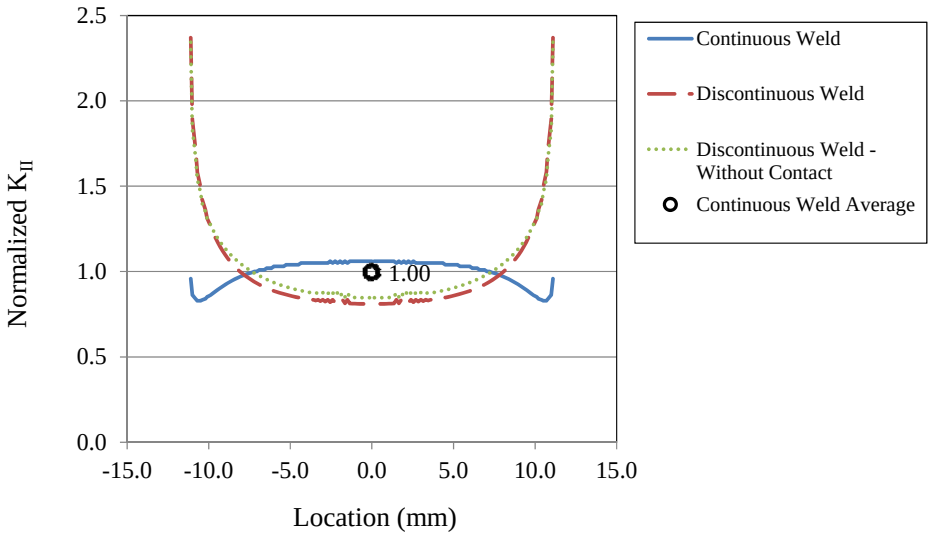
2.5
2.0
1.5
1.0
0.5
0.0
-15.0
-10.0
-5.0
0.0
5.0
10.0
15.0
Normalized K_{II}
Location (mm)
1.00
Continuous Weld
Discontinuous Weld
Discontinuous Weld - Without Contact
Continuous Weld Average

(b)

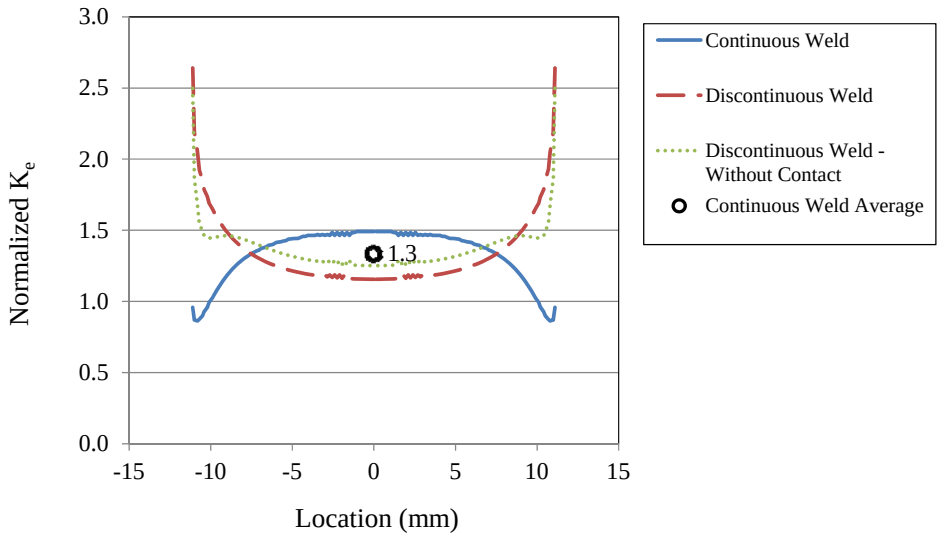

(c)

Figure 3.10. The normalized (a) mode I, (b) mode II, and (c) equivalent stress intensity factor solutions plotted along the 22.5 mm crack length where 0 is located at the mid-section of the weld.

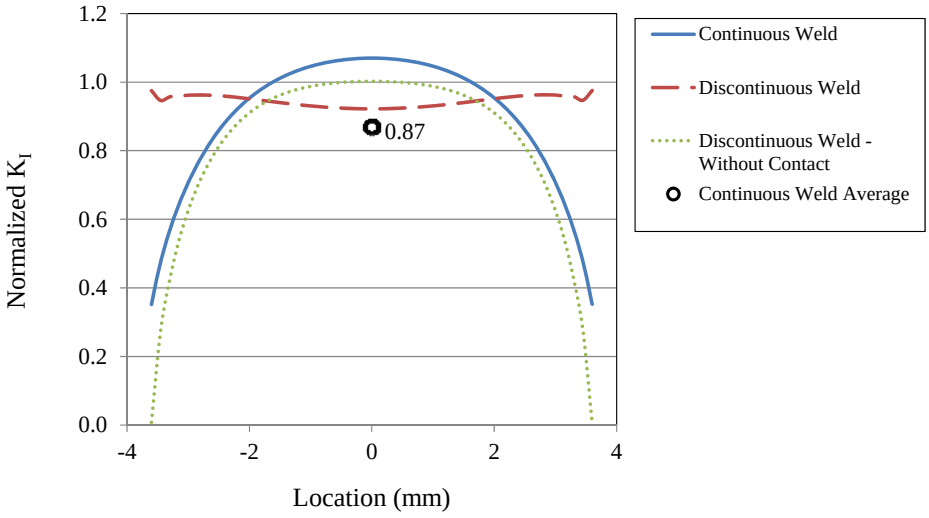
1.2
1.0
0.8
0.6
0.4
0.2
0.0
Normalized K_I
0.87
-4
-2
0
2
4
Location (mm)
Continuous Weld
Discontinuous Weld
Discontinuous Weld - Without Contact
Continuous Weld Average

(a)

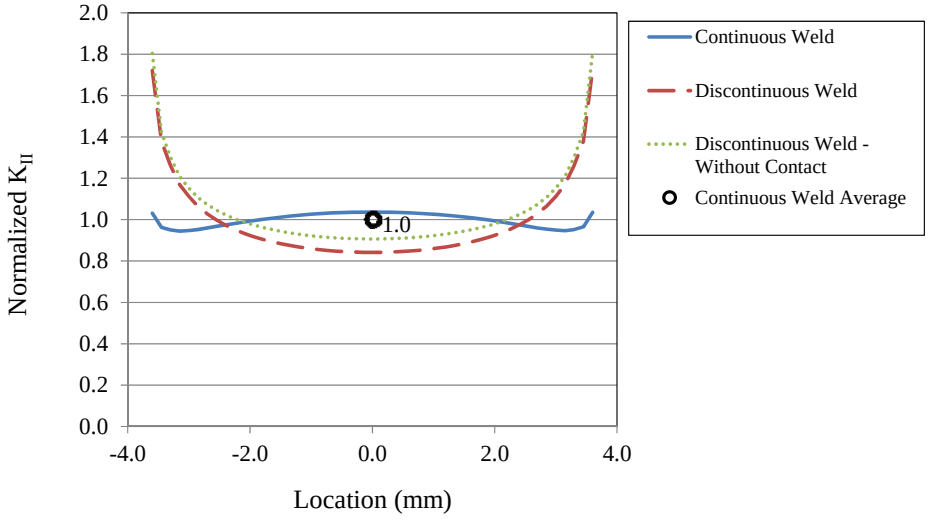
2.0
1.8
1.6
1.4
1.2
1.0
0.8
0.6
0.4
0.2
0.0
Normalized K_{II}
1.0
-4.0
-2.0
0.0
2.0
4.0
Location (mm)
Continuous Weld
Discontinuous Weld
Discontinuous Weld - Without Contact
Continuous Weld Average

(b)

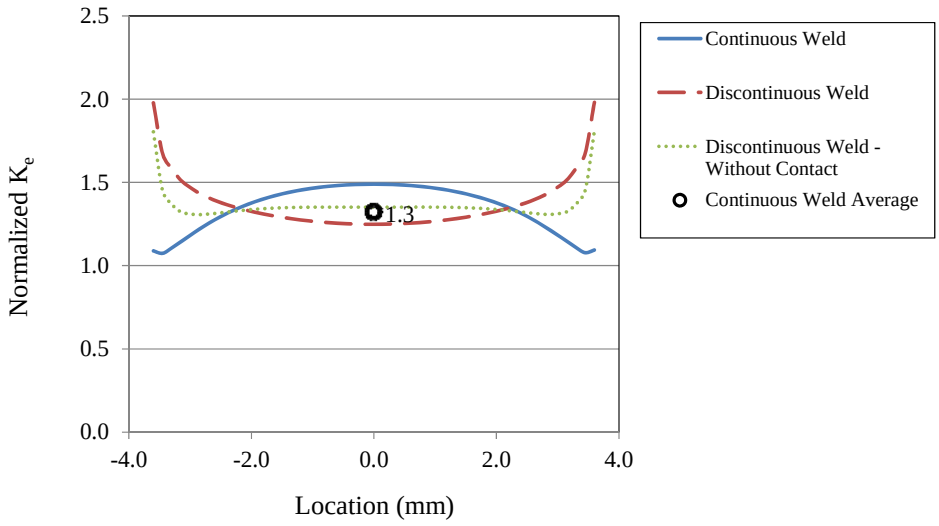

(c)

Figure 3.11. The normalized (a) mode I, (b) mode II, and (c) equivalent stress intensity factor solutions plotted along the 7.5 mm crack length where 0 is located at the mid-section of the weld.

Chapter 4
Computational Models for Simulations of Lithium-Ion Battery Modules under Constrained Compression Tests

4.1. Introduction

Lithium-ion batteries have been considered as the solution for electric vehicles for the automotive industry due to their lightweight and high energy density. For automotive applications, an understanding of the mechanical performance of lithium-ion batteries is of great importance for crashworthiness analyses. Computational models are important tools for the efficient and cost-effective design of battery cells and modules. As indicated by Ali et al. [1, 2], computational models of battery cells and modules can be developed using a detailed (micro) approach or a less detailed (macro) approach. Both approaches are useful in the investigation of the mechanical behavior of lithium-ion battery cells and modules. The detailed approach is important for understanding the micro mechanical behavior of battery cells and modules but is computationally expensive. The less detailed (macro) approach, with homogenized material models representing battery cells or modules, is computationally efficient with sacrifice of the accuracy at the micro scale.

Researchers have adopted the detailed approach and the less detailed approach in order to study the mechanical behavior of lithium-ion cells and modules. Sahraei et al. [3] developed a finite element model with a homogenized material model representing the core matrix of a cylindrical cell battery. Sahraei et al. [4] developed a finite element

model with a homogenized material model representing lithium cobalt dioxide pouch cell batteries in order to predict the behavior observed during lateral compression tests. The authors developed more detailed models in order to predict the properties observed in punch indentation and confined compression tests. Greve and Fehrenbach [5] developed a finite element model for crash simulation with a homogenized material model representing the jellyroll of cylindrical lithium-ion cells. Sahraei et al. [6] developed finite element models with a homogenized material model representing the jellyroll of a cylindrical battery cell in order to predict the load displacement properties of the cells and the deformation levels that lead to internal short circuit. Wierzbicki and Sahraei [7] proposed a procedure to determine the homogenized compressive properties of the jellyroll in cylindrical cells and developed a finite element model for the validation of the proposed procedure.

Ali et al. [1] developed a detailed finite element model in order to simulate the micro buckling behavior of representative volume element specimens of lithium-ion battery cells under in-plane constrained compression. Sahraei et al. [8] developed finite element models with homogenized material models representing three types of pouch cell batteries in order to predict the load displacement properties of the cells and the deformation levels that lead to internal short circuit. Xia et al. [9] adopted a finite element model with a homogenized material model representing a lithium-ion battery pack in order to study the damage due to ground impact. The authors developed a more detailed model of a single battery cell and shell casing in order to study the detailed cell deformation and possible failure modes of the jellyroll. Ali et al. [2] developed a finite element model with a homogenized material model representing a small-scale lithium-

iron phosphate battery module specimen in order to simulate an in-plane constrained punch indentation test.

The mechanical behavior of representative volume elements of lithium-ion battery cells under compressive loading conditions was studied by Lai et al. [10]. The test results suggested that the lithium-ion battery cells can be modeled as anisotropic foams or cellular materials. Quasi-static compression experiments of module RVE specimens were conducted by Lai et al. [11]. The authors showed that the resulting nominal stress-strain curves resemble the typical behavior of cellular materials but with distinct drops in stress. The first stress drop was believed to be caused by a full development of the first buckling mode of the module RVE. The authors presented a buckling analysis for a module RVE specimen under in-plane constrained compression and found that the heat dissipater contributes to more than 90% of the buckling stress. A similar trend in the nominal stress-strain curves was evident under dynamic loading conditions as presented by Lai et al. [12].

Ali et al. [2] adopted the macro approach and developed a homogenized material model for the efficient simulation of lithium-ion battery module specimens under punch indentation based on the experiments of Lai el al. [10-12]. This investigation focuses on the development of a semi-homogenized computational model of the module RVE specimens under in-plane constrained compression tests. The model is based on the properties of the heat dissipater, the foam, and the macro behavior of the cells determined from quasi-static experiments performed by Lai et al. [10, 11]. Since this model is based on the homogenized properties of each component, a modification to one of the components would not require additional testing of the other components in order to

predict the mechanical behavior of the heat dissipater sheet or the overall behavior of the module RVE specimen. This semi-homogenized computational model allows for computational efficiency when compared with a detailed (micro) model with sacrifice of the detail buckling behavior of the battery cells. The detailed modeling of cell RVE specimens under quasi-static in-plane compressive loading conditions was investigated in a companion study [1].

In this chapter, a computational model is developed for simulations of representative volume element (RVE) specimens of lithium-ion battery modules under in-plane constrained compression tests. The computational results from the model under quasi-static and dynamic loading conditions are compared to those from experiments. An additional finite element analysis is performed in order to validate the results of the model under quasi-static loading using the explicit solver. A further finite element analysis is performed in order to investigate whether the computational time of the model under dynamic loading conditions could be reduced further. Lastly, a finite element analysis is performed in order to determine if the increase in the nominal stress at which buckling begins in the heat dissipater under the dynamic loading conditions is due to the different buckling modes observed in the results of the finite element analyses of module RVE specimens under quasi-static loading conditions and under dynamic loading conditions.

4.2. Experiments

4.2.1. Module RVE specimens

A detailed description of the structure of the lithium-ion battery module used for this investigation can be found in Lai et al. [11]. As described by Ali et al. [2], the following definitions are used to describe the components of the battery module: "A *Single unit cell* represents a basic cell containing one cathode, one anode and a separator sheet with two aluminum cover sheets with two accompanying separator sheets. A *Seven unit cell* consists of seven basic cells containing seven cathode, seven anode, fifteen separator and two aluminum cover sheets. This seven unit cell represents a typical assembled pouch cell. A *Module* consists of two pouch cells (seven unit cells) separated by an aluminum heat dissipater sheet. The module also has two foam sheets on both sides."

A schematic of a battery module and a module RVE specimen for the in-plane constrained compression test is shown in Figure 4.1(a). A module RVE specimen is shown in Figure 4.1(b) with two cells (shown in gray), one heat dissipater sheet (shown in light blue), and two foam sheets (shown in black). The dimensions of the specimen are also shown. Figure 4.1(c) shows a side view of the module RVE specimen. As described by Ali et al. [2], the figure shows the "individual components of anodes (shown in orange), cathodes (shown in gray), separators (shown as black lines between anode, cathode, and cover sheet), cover sheets (shown in light blue), aluminum dissipater sheet (shown in light blue in the middle) and foam sheets (shown in black). The large red arrows shown in the figure indicate the in-plane compressive direction." Since the

electrolyte is difficult to handle during assembly due to the safety concern, all the module RVE specimens tested were made without electrolyte at the University of Michigan [11].

4.2.2. Quasi-static and dynamic tests of the module RVE specimens

The experimental results for module RVE specimens under in-plane compression were presented in Lai et al. [11, 12] and are reviewed briefly here. The module RVE specimen is placed in a die cavity which constrains the specimen at the bottom and side surfaces. A punch applies compressive loading to the top surface the specimen. A punch and die cavity is shown in Figure 2.2. Quasi-static compression tests were conducted at a displacement rate of 0.01 mm/s (nominal strain rate of 0.0005 s^{-1}). Figure 2.3(a) shows the deformation of two module RVE specimens due to quasi-static compression at a nominal strain of about 0.50. The figure shows the buckling behavior of the heat dissipater sheet and cells. Dynamic compression tests were conducted at a displacement rate of about 2.2 – 2.9 m/s (nominal strain rate of about 110 to 145 s^{-1}). Figure 2.3(b) shows the deformation of two module RVE specimens due to dynamic compression at a nominal strain of about 0.40. The figure shows that the buckling behavior of the specimens which were subjected to dynamic compression is similar to that of the specimens which were subjected to quasi-static compression.

Figure 2.4(a) shows the nominal stress-strain curves of the module RVE specimens which were subjected to quasi-static and dynamic compression [11, 12]. The curves resemble the typical behavior of cellular materials, which possess an initial linear region, a nearly plateau region, and a final densification region. However, unlike the

typical behavior of cellular materials, the curves show distinct drops in nominal stress. The first drop in nominal stress at the nominal strain of about 0.025 is the most prominent. After a careful examination of the deformation patterns, this drop in nominal stress is believed to be caused by the first buckling mode of the heat dissipater. Figure 4.4(b) shows the nominal stress-strain curves near the first drop in nominal stress. As shown in the figure, the nominal stress at which the heat dissipater begins to buckle under quasi-static loading conditions ranges from about 4.5 MPa to about 5.5 MPa. The nominal stress at which the heat dissipater begins to buckle under dynamic loading conditions ranges from about 9.3 MPa to about 9.7 MPa. After the initial buckling, the curves resulting from the dynamic experiments are generally consistent with the curves resulting from the quasi-static experiments.

The results of the experiments show that the general behavior of the module RVE specimens which were subjected to dynamic compression is similar to the behavior of the module RVE specimens which were subjected to quasi-static compression. The main distinction between the quasi-static and the dynamic experimental results is the nominal stress at which the initial buckling of the heat dissipater occurs. The nominal stress at which the heat dissipater begins to buckle under dynamic loading conditions is about twice as high as the nominal stress at which the heat dissipater begins to buckle under quasi-static loading conditions.

4.3. Finite element analysis

4.3.1. Finite element model

Here, a semi-homogenized computational model of the module RVE specimens under quasi-static and dynamic in-plane constrained compression loading conditions is developed. The model is based on the properties of the heat dissipater, the foam, and the macro behavior of the cells which are determined from experiments for the individual components. Computations are performed using the commercial finite element code LS-Dyna version mpp971s R5.1.1. [13]. First-order, solid elements (ELFORM 2) are used to model each component of the module RVE specimen. Figure 4.5 shows the finite element model of the module RVE specimen with dimensions. The Cartesian coordinate system is also shown in the figure. The dimensions of the each component are modeled to match the dimensions of each component when the module RVE specimen is constrained within the compression test fixture.

As shown in the figure, the width of the heat dissipater is 0.6 mm as measured along the Z-axis. Lai et al. [11] presented a buckling analysis for a module RVE specimen under in-plane constrained compression based on the analytical solution for a beam, the effective compressive moduli of the cell components, and the tensile modulus of the heat dissipater sheet. The authors found that the heat dissipater contributes to more than 90% of the buckling stress. Since the heat dissipater is the main factor influencing the behavior of the module RVE specimen, a fine mesh with three elements across the width of the heat dissipater is used in order to capture the correct buckling behavior of the heat dissipater.

The buckling behavior of the heat dissipater is influenced by the lateral support provided by the cells. There are two components representing the cells in the module RVE specimen. The width of each cell component as measured along the Z-axis is 3.3 mm. For computational efficiency, the detailed structure of the cells is not modeled. Instead the cells are modeled with a homogenized material which models the lateral support provided to the heat dissipater. The mesh density of the homogenized cells was chosen to be between the mesh density of the heat dissipater and the mesh density of the foam in order to reduce the risk of contact penetrations in the analyses.

There are two foam components included in the module RVE specimen. The width of each foam component when the module RVE specimen is constrained within the compression test fixture is 1.4 mm. The element size used to model the foam is coarser for computational efficiency. It should be noted that the width of each of the foam components when the module RVE specimen is not constrained in the compression test fixture is 1.5 mm. The battery module is usually held together by two stainless steel bands with a specified tension. The compression test fixture was designed to account for the compression condition where a pre-compressive load is applied to the battery module by the two stainless steel bands [11]. As shown later in this chapter, the foam shows very low stress at low strains and therefore the pre-compression of the foam is negligible in the computations. The element dimensions used to model each component of the module RVE specimen are listed in Table 1.

4.3.2. Boundary and loading conditions

Figure 2.6 shows the finite element model setup for a module RVE specimen in-plane constrained compression test. The coordinate system is also shown. The compression test fixture is made of steel that has a very high stiffness compared to the module RVE specimen. Therefore, the confinement surfaces are assumed to be rigid and modeled by planar rigid surfaces. As in the compression test fixture, there is zero clearance modeled between the module RVE specimen and the confinement surfaces at the bottom and sides of the specimen. The confinement surfaces at the bottom and sides of the module RVE specimen are constrained in all six degrees of freedom. The top confinement surface represents the compression test fixture punch and can only move in the vertical -Y direction by the defined velocity boundary condition. A gap is modeled between the top of the module RVE specimen and the top rigid surface in order to ensure that the rigid surface is moving at a constant velocity while compressing the module RVE specimen.

The compression test speed of 0.01 mm/s is considered as a quasi-static condition. As discussed by Ali et al. [1], using the explicit dynamics solver to model a quasi-static event requires some special considerations. It is computationally impractical to model the quasi-static loading process by a time step to satisfy the Courant-Friedrich-Lewy condition of numerical stability. A solution is typically obtained either by artificially increasing the loading rate or increasing the mass of the system, or both. A general recommendation is to limit the impact velocity to less than 1% of the wave speed of the specimen, and a mass scaling of 5 to 10% is typical to achieve a desirable stable time

increment. Also the kinetic energy of the deforming specimen should not exceed a small fraction (1 to 5%) of the internal energy throughout the quasi-static analysis [1].

For explicit analyses, the critical time step is the maximum time step which will result in numerical stability without adding mass to the system. For a three-dimensional continuum finite element, the critical time step Δt_c is given by the equation

$$\Delta t_c = \frac{l_C}{C} \tag{4.1}$$

where C is the wave speed and l_C is the characteristic length of the finite element. The wave speed C for a three-dimensional continuum finite element is given by the equation

$$C = \sqrt{\frac{E(1-\nu)}{\rho(1+\nu)(1-2\nu)}} \tag{4.2}$$

where E is Young's modulus, ν is Poisson's ratio, and ρ is the density. The characteristic length for a three-dimensional continuum finite element is given by the equation

$$l_C = \frac{V_e}{A_{e,\max}} \tag{4.3}$$

where V_e is the volume of the finite element and $A_{e,\max}$ is the surface area of largest side of the finite element [14]. The wave speed and critical time step of each component in the model are listed in Table 1.

For a reasonable computational time, the finite element analysis for the quasi-static loading condition is conducted at a speed of 200 mm/s using a time step of 6.0×10^{-8} s. Mass is added to the system since the time step exceeds the critical time step for the components. The percent added mass of the system was about 80% at the start of the

analysis and increased to about 98% as the module RVE specimen deformed. The percent added mass is similar to that used for the detailed modeling of a cell RVE specimen investigated by Ali et al. in a companion study [1]. The maximum ratio of the kinetic energy to the internal energy of the module RVE specimen was about 0.1%. Loading velocities of 45 mm/s and 100 mm/s were also examined. The results showed that the nominal stress at which the heat dissipater begins to buckle was reduced by about 3% with the loading velocity of 45 mm/s. There was negligible change in the nominal stress at which the heat dissipater began to buckle with the loading velocity of 100 mm/s.

The compression test speed of 2200 - 2900 mm/s is considered as the dynamic loading condition. The finite element analysis for the dynamic loading condition is conducted at a speed of 2500 mm/s. Since the loading rate for the dynamic loading condition is much larger than the loading rate for the quasi-static loading condition the computational time step was reduced to 3.0×10^{-8} s with reasonable computational time. This time step is less than the critical time step listed in Table 1, therefore, there is no added mass at the start of the analysis. However, at large nominal strains, as the module RVE specimen deformed, the percent added mass of the system increased to about 1.9%. The maximum ratio of the kinetic energy to the internal energy of the module RVE specimen was about 2% which occurred at the start of the specimen deformation and reduced to near 0% at nominal strains above 0.1.

4.3.3. Contact modeling

The confinement surfaces representing the compression test fixture and the top surface representing the compression test fixture punch are modeled with rigidwalls in LS-Dyna, (also referred to as stonewalls.) The constraint method is used to define the contact behavior between the nodes of the module RVE specimen and the rigidwalls. For nodes that come into contact with the rigidwall, the constraint method sets the velocity and acceleration in the direction normal to the rigidwall to zero [15]. The nodes are therefore prevented from penetrating through the rigidwall but can still move tangential to the rigidwall, depending on the coefficient of friction.

The surface to surface contact algorithm of LS-Dyna is used to model the contact interaction between the surfaces of each component of the module RVE specimen [16]. The surface to surface contact algorithm is a two-way contact type which checks the slave nodes for penetration through the master segments and then checks the master nodes for penetration through the slave segments. The smooth option is applied to the contact algorithm so that a surface is automatically fit from the mesh allowing the contact to be calculated on the smooth surface rather than on the linear element [17].

Shell elements which are assigned the null material are used on the surface of each component in order to overcome the difference in stiffness between the contacting surfaces of each component due to the dissimilar materials of the components. The nodes of the null shell elements are equivalent to the nodes of the solid elements. The shell elements assigned to the null material are not part of the structure and are completely bypassed in the element processing [13]. The Young's modulus and Poisson's ratio are used only for setting the contact interface stiffness. A Young's modulus of 5000 MPa, a

Poisson's ratio of 0, and a thickness of 0.01 mm are assigned to the null shell elements in the model. The non-automatic contact option is applied such that the thickness of the null shells is not considered in the contact algorithm.

All of the contact surfaces are assumed to be in friction contact with each other. A coefficient of friction of 0.1 is applied between the heat dissipater and the homogenized cells and between the homogenized cells and the foam. This coefficient of friction is adopted from Ali et al. [1] and was shown to give reasonable results for the micro buckling behavior of representative volume element specimens of lithium-ion battery cells under in-plane constrained compression. The coefficients of friction between the module RVE specimen and the confinement surfaces at the sides and the top of the module RVE specimen are adopted from Ali et al. [2]. A coefficient of friction of 0 is applied between the module RVE specimen and the confinement surfaces at the sides of the module RVE specimen. Between the module RVE specimen and the top confinement surface, which represents the compression fixture punch, a coefficient of friction of 0.2 is applied. The coefficient of friction between the module RVE specimen and the confinement surface at the bottom of the module RVE specimen is selected in order to match the sliding behavior of the heat dissipater observed in the experimental results at the bottom confinement surface. A coefficient of friction of 1 is applied between the module RVE specimen and the confinement surface at the bottom of the module RVE specimen.

4.3.4. Material modeling of the heat dissipater

The mechanical behaviors of the individual components of the battery modules were examined and discussed in detail in Lai et al. [11]. For the current investigation, the elastic-plastic tensile stress-strain data for the heat dissipater obtained in [11] is used to define the strain hardening behavior due to the difficulties in obtaining such data under uniaxial 'unconstrained' compression tests. Lai et al. [11] performed tensile tests on three heat dissipater sheets according to the ASTM E8/E8M-11 tensile specimen standard for thin sheet materials. The nominal stress-strain curves of the heat dissipater sheets are shown in Figure 2.7 along with an image of the failed region of one of the specimens. A finite element model replicating the tensile tests was developed using the same element type and mesh density as used in the module RVE model. The finite element analysis of the tensile test was used to verify the material properties of the heat dissipater prior to running the finite element analyses of the module RVE.

The initial part of the tensile stress-strain curve of the heat dissipater in the finite element model is modeled as elastic with the Young's modulus E. For the LS-Dyna solver, the nominal stress-strain data must be converted to true stress-true plastic strain for elastic-plastic finite element analyses. When the stress is larger than the initial yield stress σ_0, the conversion to the true stress-true plastic strain curve is based on the assumption of plastic incompressibility for metal plasticity. For the heat dissipater, σ_0 and E are estimated as 65 MPa and 47 GPa, respectively, from the experimental data. Since there is little necking, as shown in the image of the failed region of a specimen in Figure 2.7, the assumption of plastic incompressibility was used beyond the ultimate stress in the conversion to the true stress-true plastic strain. Figure 2.7 shows the nominal

stress-strain curves for the heat dissipater from three sheet specimens and the resulting curve from the finite element analysis.

4.3.5. Material modeling of the homogenized cells

Lai et al. [12] performed quasi-static in-plane constrained and quasi-static out-of-plane compression tests on cell RVE specimens. The results of the compression tests showed anisotropic behavior of the cell RVE and that the layers of the cell RVE specimens are deformed by multi-scale buckling phenomenon - both layer micro buckling and global macro buckling. For computational efficiency it is not practical to model the detail buckling behavior of the cell RVE specimens. Since the heat dissipater is the main factor influencing the behavior of the module RVE specimen, a macro homogenized material model is adopted in order to simulate the out-of-plane behavior of the cell RVE specimens which provides lateral support to the heat dissipater.

The nominal compressive stress-strain curves of the cell RVE specimens under out-of-plane compression are shown in Figure 2.8. The in-plane nominal compressive stress-strain curves are also shown for comparison. A finite element model replicating the out-of-plane compression test was developed using the same element type and mesh density as used in the module RVE specimen model. The finite element analysis of the compression test was used to verify the material properties of the homogenized cells prior to running the finite element analyses of the module RVE.

The crushable foam model in LS-Dyna is used to model the homogenized cells. For the crushable foam model, the stress-volumetric strain data is needed for the finite

element analyses. Since the Poisson ratio of the cells as tested in Lai et al. [12] is nearly zero, the nominal stress-strain curve from the out-of-plane compression test is used directly in the model. The nominal stress-strain curve resulting from the finite element analysis is shown in Figure 2.8.

4.3.6. Material modeling of the foam

Lai et al. [11] performed a quasi-static, out-of-plane compression test on foam layers typically used in battery modules. The specimen was made by stacking four pieces of 20 mm × 20 mm × 1.5 mm foam for a total specimen thickness of 6 mm. The nominal compressive stress-strain curve of the foam is shown in Figure 2.9. A finite element model replicating the foam compression test was developed using the same element type and similar mesh density as used in the module RVE model. The finite element analysis of the compression test was used to verify the material properties of the foam prior to running the finite element analyses of the module RVE.

The crushable foam model in LS-Dyna is used to model the module RVE specimen foam. For the crushable foam model, the stress-volumetric strain data is needed for the finite element analyses. Since the Poisson ratio of the foam as tested in Lai et al. [11] is nearly zero, the nominal stress-strain curve from the compression test is used directly in the model. Figure 2.9 shows the nominal stress-strain curve for the layered foam specimen and the resulting curve from the finite element analysis.

4.4. Computational results

4.4.1. Results of the quasi-static finite element analysis

In the following, the nominal stress-strain responses of the tested module RVE specimens are compared to those of the finite element analyses. The nominal stress-nominal strain curve obtained from the results of the quasi-static finite element analysis is plotted in Figure 2.10(a) along with the experimental results. In general, the results of the finite element analysis agree with the experimental results. The results of the finite element analysis show that the nominal stress at which the heat dissipater begins to buckling is 6.4 MPa. This nominal buckling stress compares well with the experimental results but occurs at lower nominal strain when compared with the experimental results.

Figure 2.10(b) shows the deformation of the module RVE specimen from the finite element analysis at the start of buckling at a nominal strain of about 0.005. After the initial buckling, the resulting curve from the finite element analysis resembles the typical behavior of cellular materials but with distinct drops in nominal stress. A small peak in the nominal stress occurs at a nominal strain of about 0.04. As shown in Figure 2.10(c), at this nominal strain, the foam on the right side of the module RVE specimen is fully compressed and the cells contact the rigidwall. The nominal stress continues to increase until a nominal strain of about 0.07 when the heat dissipater is flattening near the top. The nominal stress-strain curve begins to plateau at this nominal strain until a nominal strain of about 0.1 when the nominal stress begins to drop due to the flattening of the heat dissipater. The deformation of the module RVE specimen during the flattening process is shown in Figure 2.10(d) at nominal strain of about 0.09. During this

flattening stage, the heat dissipater is not deforming at the location of initial buckling. The nominal stress begins to increase at a nominal strain of about 0.11 when the heat dissipater continues to deform at the location of initial buckling and begins to compress the cells on the left side of the module RVE specimen laterally. The deformation of the module RVE specimen at the nominal strain of about 0.11 is shown in Figure 2.10(e). The nominal stress continues to increase as the heat dissipater continues to flatten, compress the cells on the left side of the module RVE specimen laterally, and as the cells on the right side of the module RVE specimen continue to bend and more of the cell elements contact the rigid wall as shown at a nominal strain of about 0.23 in Figure 2.10(f). The heat dissipater is nearly flat at the nominal strain of about 0.30 as shown in Figure 2.10(g). Finally, a second buckling occurs near the bottom of the heat dissipater at a nominal strain of about 0.34 as shown in Figure 2.10(h). The deformation in the module RVE specimen as the stress drops due to the second buckling is shown in Figure 2.10(i) at a nominal strain of about 0.35. The deformation in the module RVE specimen at the end of the analysis is shown in Figure 2.10(j) at a nominal strain of about 0.43, when some of the elements in the cells begin to show negative volume. As shown in Figure 2.10(j), the deformation of the module RVE specimen from the quasi-static finite element analysis shows two half-waves. This compares well with the experimental results which showed two half-waves in one specimen and three half-waves in another specimen as shown in Figure 2.3(a).

4.4.2. Results of the dynamic finite element analysis

The nominal stress-strain curve obtained from the results of the dynamic finite element analysis is plotted in Figure 2.11(a) along with the experimental results. In general, the results of the finite element analysis agree with the experimental results. The initial nominal buckling stress from the finite element analysis is 9.5 MPa. This nominal buckling stress compares well with the experimental results. As observed in the experimental results, the results of the finite element analyses show that the nominal stress at which the heat dissipater begins to buckle under dynamic loading conditions is about twice as high as the nominal stress at which the heat dissipater begins to buckle under quasi-static loading conditions.

Figure 2.11(b) shows the deformation of the module RVE specimen from the finite element analysis at the start of buckling at the nominal strain of about 0.033. After the first buckling stress, the resulting curve from the finite element analysis resembles the typical behavior of cellular materials but with distinct drops in nominal stress. A small peak in stress occurs at a nominal strain of about 0.070. As shown in Figure 2.11(c), at this nominal strain, the foam on the right side of the module RVE specimen is fully compressed and the cells contact the rigidwall. The nominal stress continues to increase as the heat dissipater continues to deform and compress the cells on the left side and right side of the module RVE specimen laterally as shown at a nominal strain of about 0.25 in Figure 2.11(d). The deformation in the module RVE specimen at the end of the analysis is shown in Figure 2.11(e) at a nominal strain of about 0.40, when some of the elements in the heat dissipater begin to show negative volume. As shown in Figure 2.11(e), the deformation of the module RVE specimen from the dynamic finite element analysis

shows two half-waves. This compares well with the experimental results which showed two half-waves in the two specimens shown in Figure 2.3(b).

4.5. Discussion

Based on the experimental observations of the module RVE specimens under in-plane constrained compression, the nominal stress at which the heat dissipater begins to buckle under dynamic loading conditions is about twice as high as the nominal stress at which the heat dissipater begins to buckle under quasi-static loading conditions. The results from the finite element analyses show initial nominal buckling stresses similar to those observed in the experiments even though there are no strain rate dependencies defined in the material models of the module RVE specimen components. In explicit analyses, nodal displacements are calculated from the nodal velocities and nodal accelerations. From the displacements, the strains and then the stresses are calculated. The solution is advanced for each time step by integrating the equation of motion with respect to time. For explicit analyses the equation of motion can be written as:

$$ma^{\Delta t} + cv^{\Delta t} + f_{\text{int}}^{\Delta t} = f_{ext}^{\Delta t} \tag{4.4}$$

where Δt indicates the time step, m is the mass matrix, a is the nodal acceleration, c is the damping matrix, v is the nodal velocity, f_{int} is the summation of the internal forces acting on each node, and f_{ext} is the summation of the external forces acting on each node [18]. For quasi-static analyses, the nodal accelerations are small and the inertia term $ma^{\Delta t}$ can be neglected. However, for dynamic analyses, the inertia term can have a significant effect on the solution.

As discussed earlier in this chapter, using the explicit dynamics solver to model a quasi-static event requires some special considerations. For a reasonable computational time, the finite element analysis for the quasi-static loading condition was conducted at a speed of 200 mm/s using a time step of $6.0x10^{-8}$ s. Mass is added to the system since the time step exceeds the critical time step for the components. In order to check the validity of the model with the added mass, the model was run with the time step reduced to $3.0x10^{-8}$ s. This time step is less than the critical time step listed in Table 1, therefore there is no added mass at the beginning of the analysis. The results showed that the initial nominal buckling stress was reduced by about 1% with the reduced time step.

Since the loading rate for the dynamic loading condition is much larger than the loading rate for the quasi-static loading condition the computational time step was reduced to $3.0x10^{-8}$ s with reasonable computational time. In order to investigate whether the computational time for the dynamic loading condition could be reduced further, the model was run with the time step of $6.0x10^{-8}$ s as in the quasi-static analysis. The added mass with the increased time step was similar to that of the quasi-static analysis. The results showed a negligible change in the initial nominal buckling stress and deformation of the module RVE specimen up to a nominal strain of about 0.2. After the nominal strain of about 0.2 the kinetic energy of the module RVE specimen exceeded 5% of the internal energy.

A further finite element analysis was conducted in order to determine if the increase in the nominal stress at which buckling begins in the heat dissipater under the dynamic loading conditions is due to the different buckling modes observed in the results of the finite element analyses of the module RVE specimens under quasi-static loading

conditions and under dynamic loading conditions. As shown in Figures 4.10(b)-4.10(j), under quasi-static loading conditions the results from the finite element analysis show that as the module RVE specimen is compressed, the heat dissipater slides along the surface of the punch. However, as shown in Figures 4.11(b)-4.11(e), the results from the finite element analysis under dynamic loading conditions show little to no sliding of the heat dissipater along the surface of the punch. A coefficient of friction of 0.2 was applied between the module RVE specimen and the punch for both simulations. In order to investigate the effects of the buckling mode, the finite element analysis for the module RVE specimen under quasi-static loading conditions was run with the coefficient of friction between the module RVE specimen and the punch increased to 1. The results showed a similar buckling mode of the module RVE specimen as under dynamic loading conditions however, there was negligible change in the first buckling stress from the results of the module RVE specimen under quasi-static loading conditions. Therefore, the increase in the nominal stress at which buckling begins in the heat dissipater under the dynamic loading conditions is not due to the different buckling modes observed in the results of the finite element analyses of the module RVE specimens under quasi-static loading conditions and under dynamic loading conditions.

4.6. Conclusions

In this chapter, a computational model is developed for simulations of representative volume element (RVE) specimens of lithium-ion battery modules under in-plane constrained compression tests. The model is based on the properties of the heat

dissipater, the foam, and the macro behavior of the cells. This semi-homogenized computational model allows for computational efficiency with sacrifice of the detail buckling behavior of the battery cells. Since the model is based on the homogenized properties of each component, a modification to one of the components would not require additional testing of the other components in order to predict the overall behavior the module RVE specimen. The computational results from the model under quasi-static and dynamic loading conditions were compared to those from experiments. The results show that the nominal stress-strain responses and the deformation patterns of the heat dissipater obtained from the semi-homogenized module model compare fairly well with experimental results.

An additional finite element analysis was performed which showed that the results of the model under quasi-static loading conditions are valid using the explicit solver. A further finite element analysis was performed in order to investigate whether the computational time of the model under dynamic loading conditions could be reduced further. The results indicate that the computational time can be decreased with a negligible change in the initial nominal buckling stress and deformation of the module RVE specimen; however, after the nominal strain of 0.2 the kinetic energy of the module RVE specimen exceeded 5% of the internal energy. Lastly, a finite element analysis was performed in order to determine if the increase in the nominal stress at which buckling begins in the heat dissipater under the dynamic loading conditions is due to the different buckling modes observed in the results of the finite element analyses of the module RVE specimens under quasi-static loading conditions and under dynamic loading conditions.

The results indicate that the increase in the initial nominal buckling stress under dynamic loading conditions is not due to a difference in the buckling mode.

References

1. Ali, M.Y., Lai, W., Pan, J., “Computational Models for Simulation of a Lithium-Ion Battery Cells under Constrained Compression Tests,” Journal of Power Sources, 242 (2013) 325-340.

2. Ali, M.Y., Lai W., Pan, J., “Computational Models for Simulation of a Lithium-Ion Battery Module Specimen under Punch Indentation,” Journal of Power Sources, 273 (2015) 448-459.

3. Sahraei, E., Wierzbicki, T., Hill, Luo, R., “Crash Safety of Lithium-Ion Batteries Towards Development of a Computational Model,” SAE Technical Paper 2010-01-1078 (2010), doi:10.4271/2010-01-1078.

4. Sahraei, E., Hill, R., Wierzbicki, T., “Calibration and Finite Element Simulation of Pouch Lithium-Ion Batteries for Mechanical Integrity,” Journal of Power Sources 201 (2012) 307– 321, doi:10.1016/j.jpowsour.2011.10.094.

5. Greve, L., Fehrenbach, C., “Mechanical Testing and Macro-Mechanical Finite Element Simulation of the Deformation, Fracture, and Short Circuit Initiation of Cylindrical Lithium Ion Battery Cells,” Journal of Power Sources 214 (2012) 377–385, doi:10.1016/j.jpowsour.2012.04.055.

6. Sahraei, E., Campbell, J., Wierzbicki, T., “Modeling and Short Circuit Detection of 18650 Li-Ion Cells under Mechanical Abuse Conditions,” Journal of Power Sources 220 (2012) 360– 372, doi:10.1016/j.jpowsour.2012.07.057.

7. Wierzbicki, T., Sahraei, E., “Homogenized Mechanical Properties for the Jellyroll of Cylindrical Lithium-Ion Cells,” Journal of Power Sources 241 (2013) 467– 476, doi:10.1016/j.jpowsour.2013.04.13.

8. Sahraei, E., Meier, J., Wierzbicki, T., “Characterizing and Modeling Mechanical Properties and Onset of Short Circuit for Three Types of Lithium-Ion Pouch Cells,” Journal of Power Sources 247 (2014) 503– 516, doi:10.1016/j.jpowsour.2013.08.056.

9. Xia, Y., Wierzbicki, T., Sahraei, E., Zhang, X., “Damage of Cells and Battery Packs Due to Ground Impact,” Journal of Power Sources 267 (2014) 78– 98, doi:10.1016/j.jpowsour.2014.05.078.

10. Lai, W., Ali, M.Y., Pan, J., “Mechanical Behavior of Representative Volume Elements of Lithium-Ion Battery Cells under Compressive Loading Conditions,” Journal of Power Sources, 245 (2014) 609-623.

11. Lai, W., Ali, M.Y., Pan, J., “Mechanical Behavior of Representative Volume Elements of Lithium-Ion Battery Modules under Various Loading Conditions,” Journal of Power Sources, 248 (2014) 789-808.

12. Lai, W., Ali, M.Y., Pan, J., “Effects of Impact Velocity on Compressive Behavior of Representative Volume Element Specimens of Lithium-Ion Battery Cells,” Presented at the 2014 SAE International Congress and Exposition, Detroit, Michigan, (2014).

13. LS-Dyna User’s Manuals, Livermore Software Technology Corporation, Livermore, CA, (2012).

14. LS-Dyna Support, “Time step size,” Retrieved from http://www.dynasupport.com/tutorial/ls-dyna-users-guide/time-step-size, (2012).

15. Jensen, M.R., “Introduction to LS-Dyna - Chapter 5: Contact Modeling” [Course Handout], Livermore Software Technology Corporation, (2003-2010).

16. LS-Dyna Support, “Contact Modeling in LS-Dyna,” Retrieved from http://www.dynasupport.com/tutorial/contact-modeling-in-ls-dyna, (2012).

17. LS-Dyna Support, “SMOOTH Option,” Retrieved from http://www.dynasupport.com/howtos/contact/smooth-option/?searchter, (2012).

18. Jensen, M.R., “Introduction to LS-Dyna Implicit – Version 3.0” [Course Handout], Livermore Software Technology Corporation, (2006-2010).

Table 4.1. The element dimensions, the wave speed, and the critical time step of each component of the module RVE specimen model.

Component	Element Dimensions [mm]			Wave Speed C [m/s]	Critical Time Step Δt_c [s]
	Δx	Δy	Δz		
Heat Dissipater	0.25	0.25	0.20	4933	4.05×10^{-8}
Cells	0.33	0.50	0.47	2066	1.61×10^{-7}
Foam	1.67	2.00	0.70	833	8.41×10^{-7}

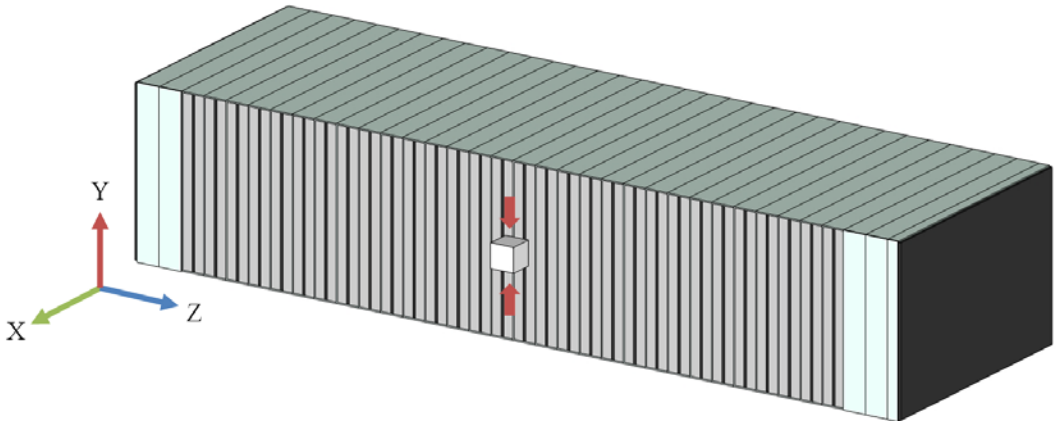

(a)

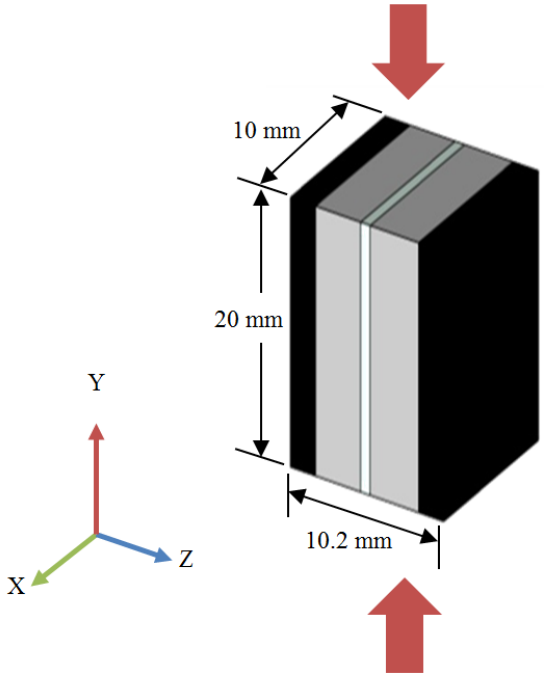

(b)

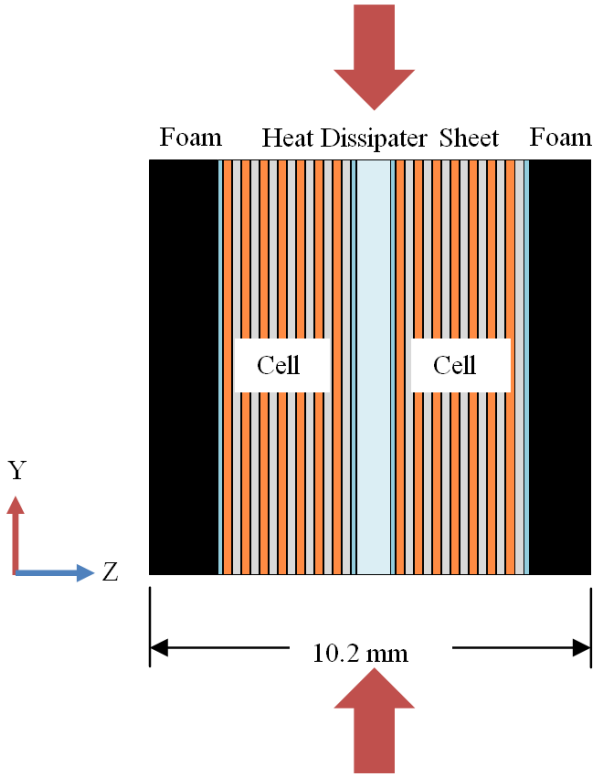

(c)

Figure 4.1. Schematics of (a) a battery module and a module RVE specimen for the in-plane constrained compression test, (b) a module RVE specimen with the dimensions, and (c) a side view of the module RVE specimen showing the individual components. The large red arrows indicate the compressive direction.

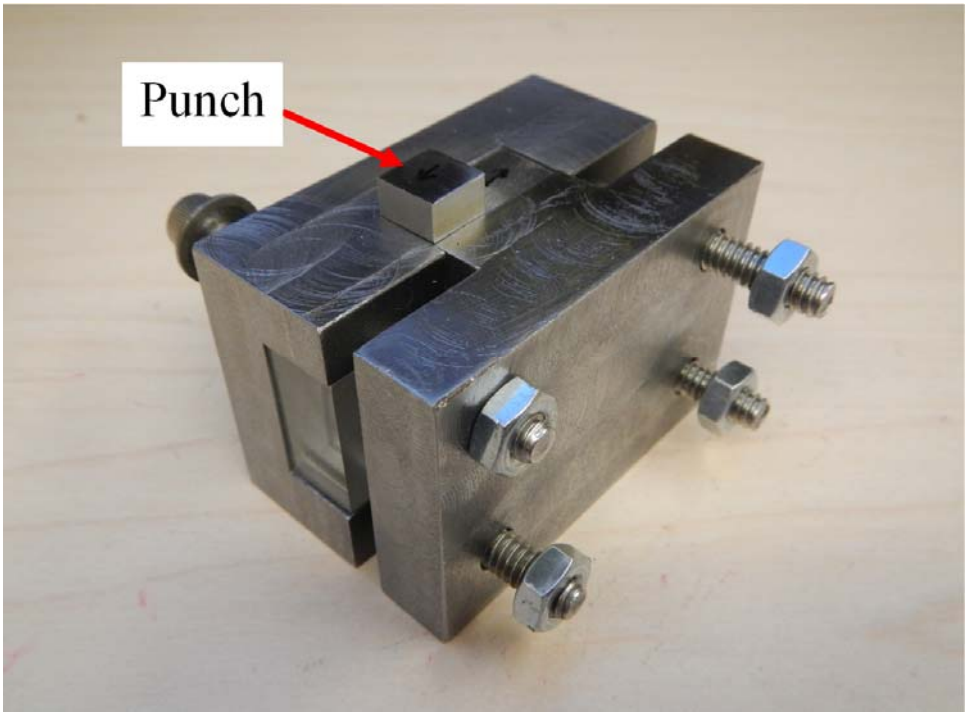

Figure 4.2. A punch and die setup for the in-plane compression tests of module RVE specimens.

(a)

(b)

Figure 4.3. The deformation of two module RVE specimens due to (a) quasi-static compression at a nominal strain of about 0.50 and (b) dynamic compression at nominal strain of about 0.40

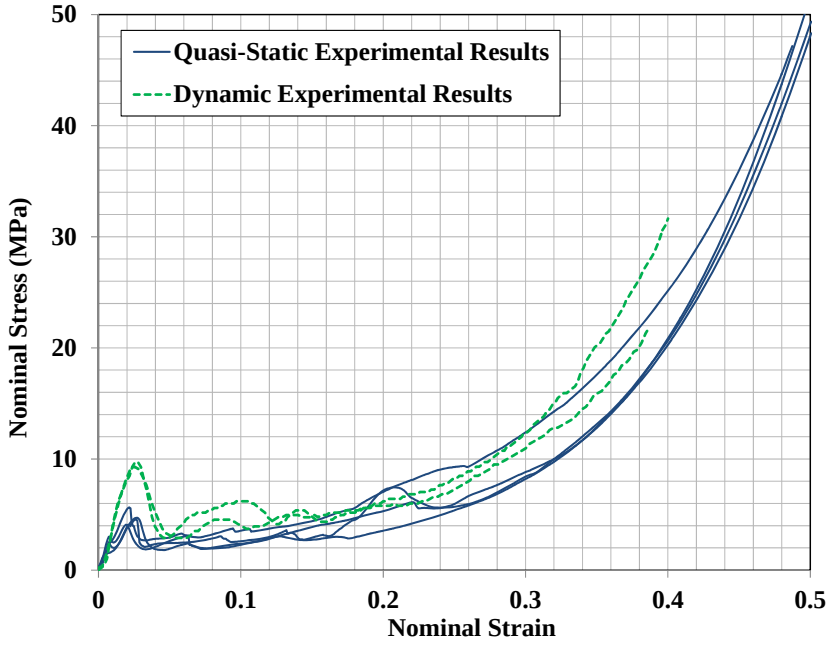

(a)

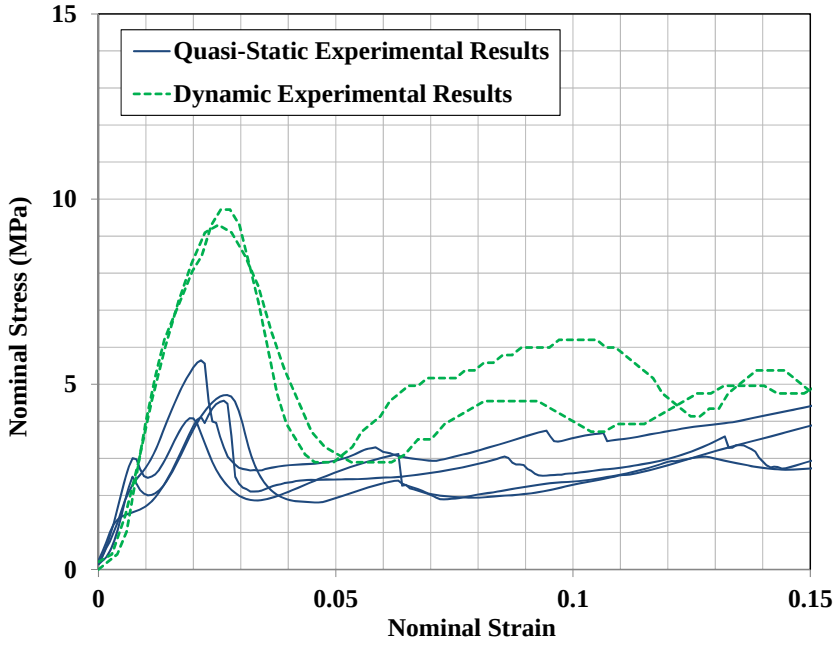

(b)

Figure 4.4. (a) The nominal stress-strain curves of the module RVE specimens which were subjected to quasi-static and dynamic compression and (b) the nominal stress-strain curves near the first drop in nominal stress.

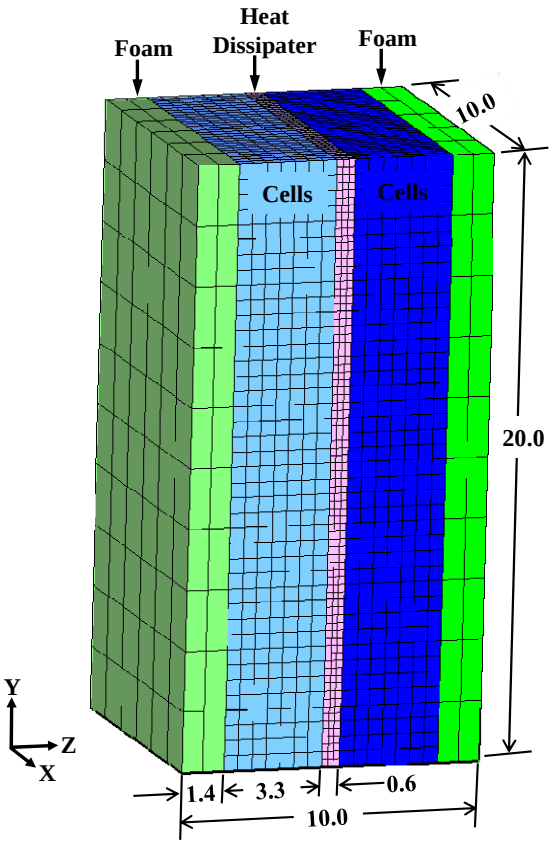

Figure 4.5. The finite element model of the module RVE specimen with dimensions shown in millimeters.

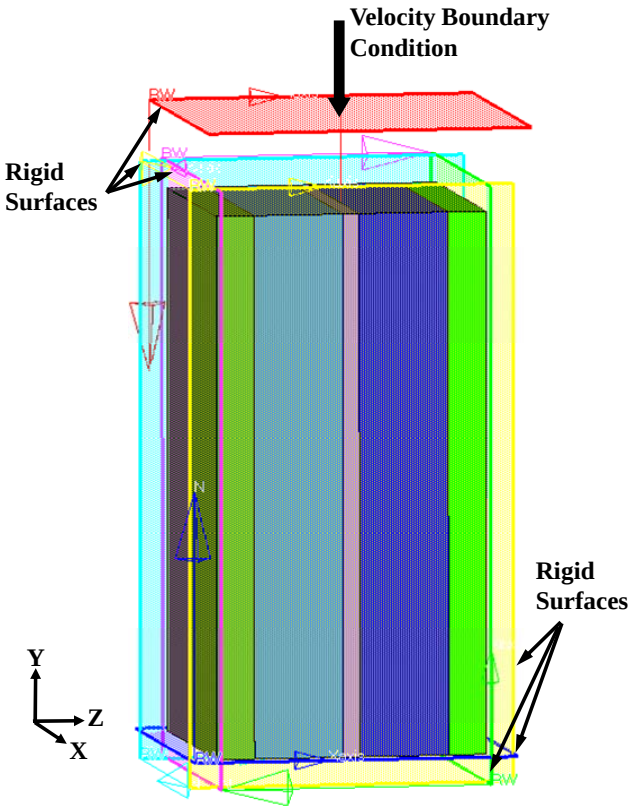

Figure 4.6. The finite element model setup for a module RVE specimen in-plane constrained compression test.

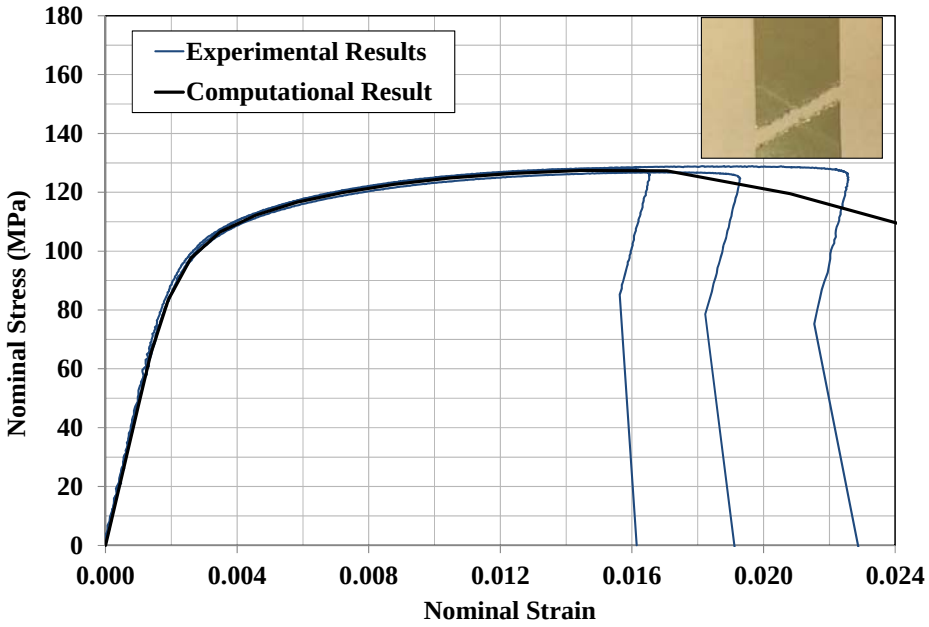

Figure 4.7. The nominal stress-strain curves for the heat dissipater from three sheet specimens along with an image of the failed region of one of the specimens and the resulting curve from the finite element analysis.

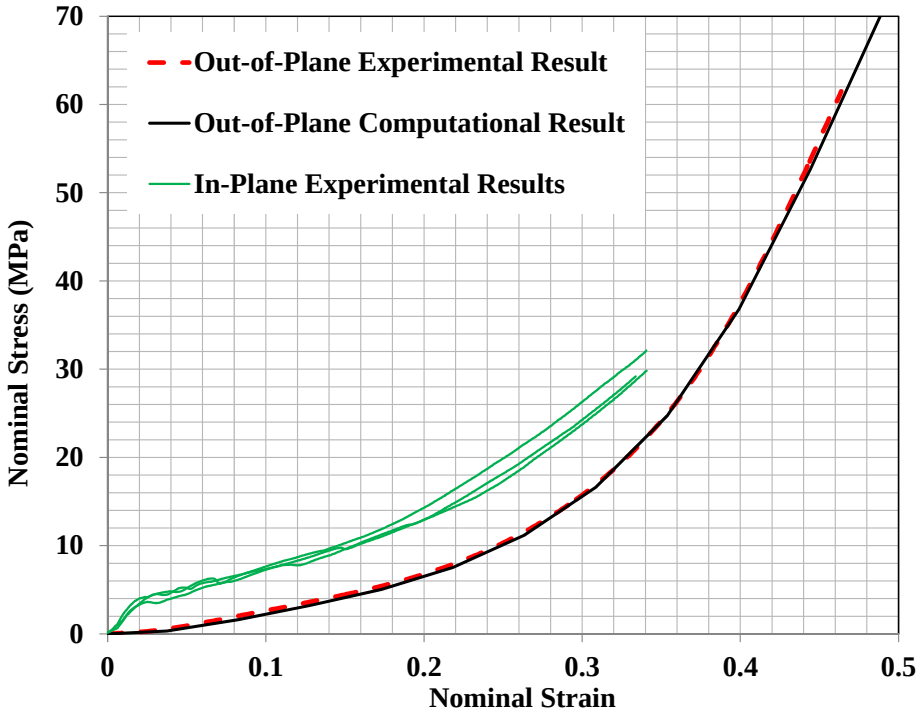

Figure 4.8. The nominal compressive stress-strain curves of the cell RVE specimens and the resulting curve from the finite element analysis.

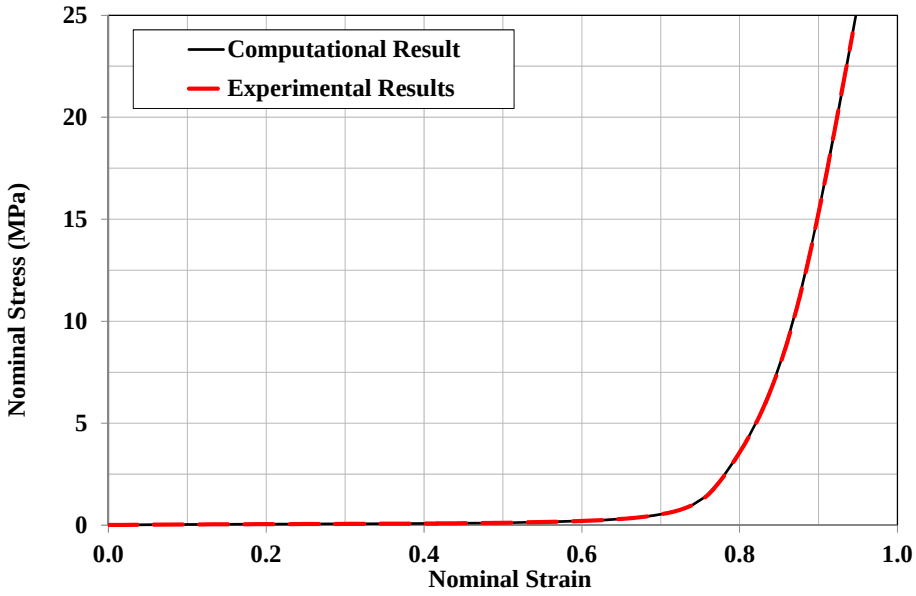

Figure 4.9. The nominal stress-strain curve for the layered foam specimen and the resulting curve from the finite element analysis.

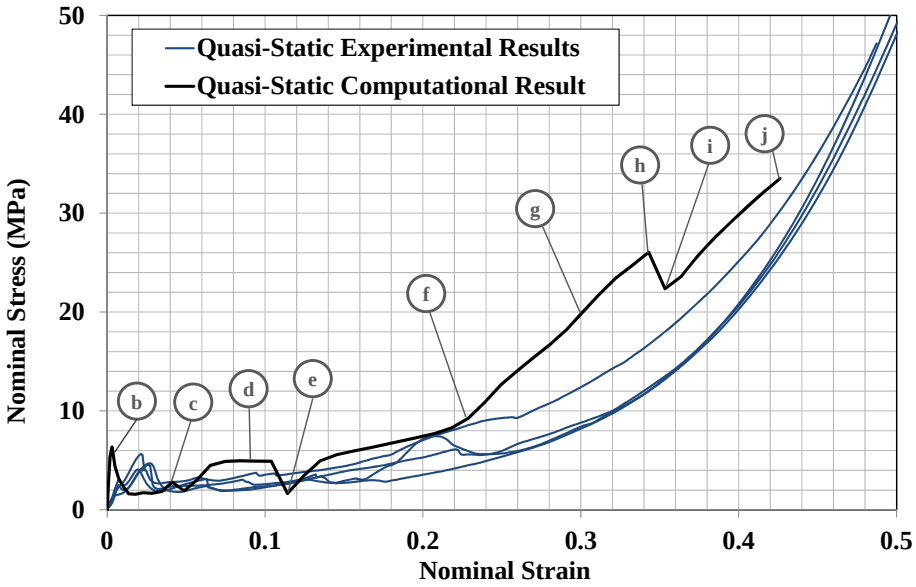
Quasi-Static Experimental Results
Quasi-Static Computational Result
Nominal Stress (MPa)
Nominal Strain
0
10
20
30
40
50
0
0.1
0.2
0.3
0.4
0.5
b
c
d
e
f
g
h
i
j

(a)

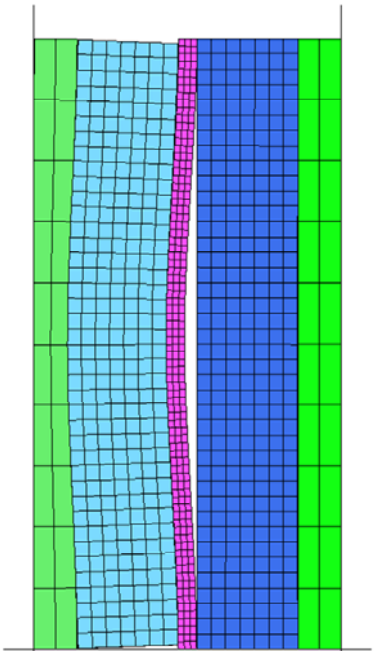

(b)

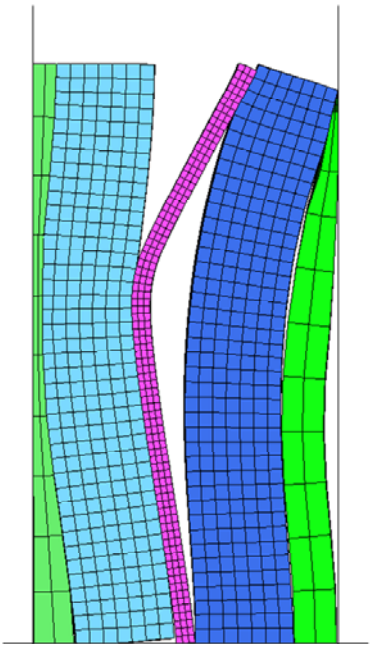

(c)

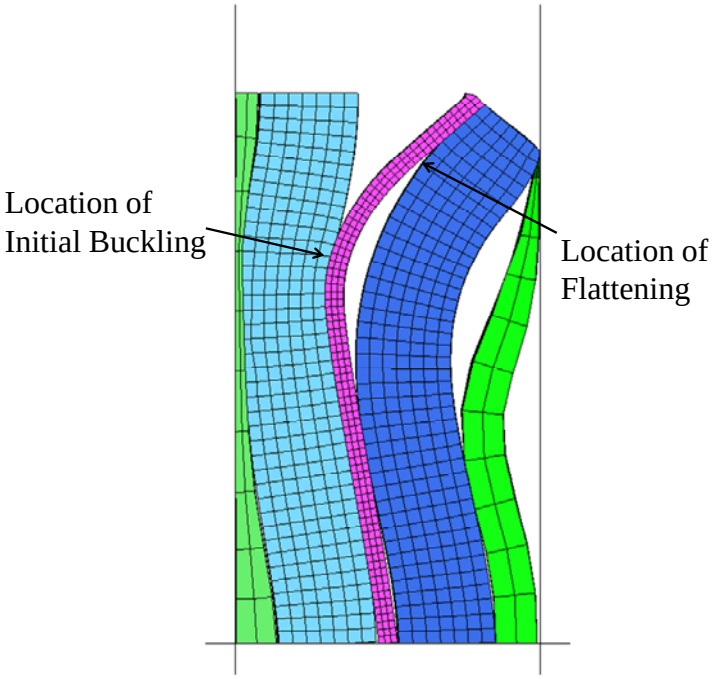

(d)

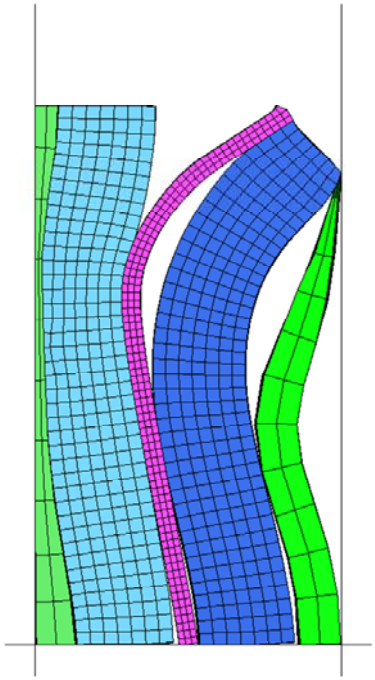

(e)

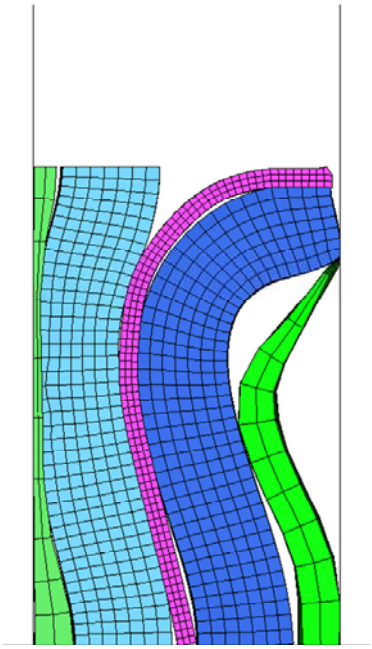

(f)

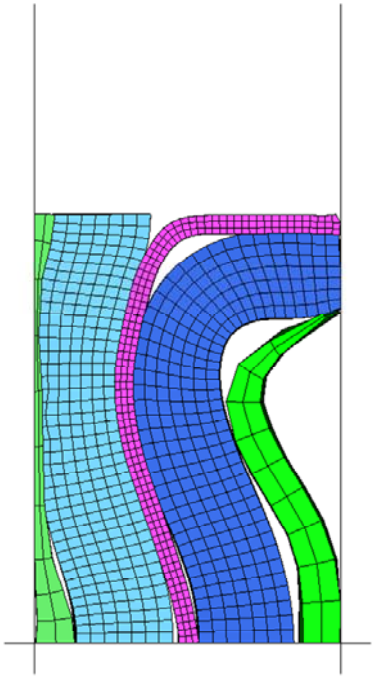

(g)

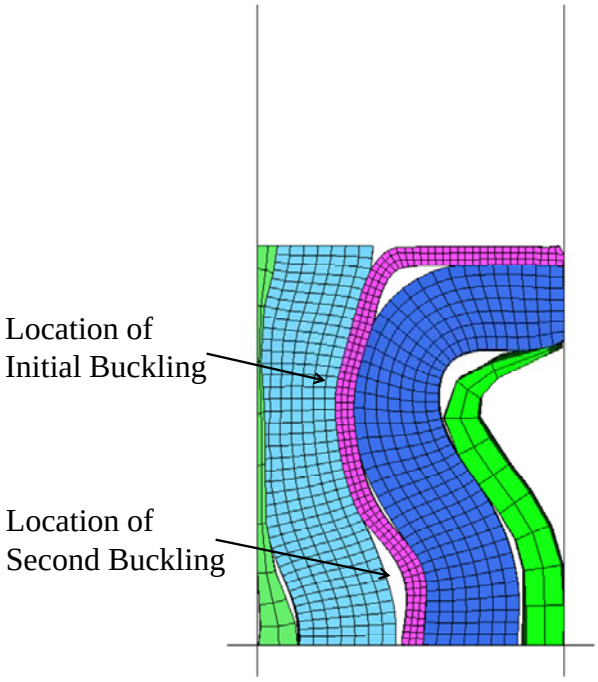

(h)

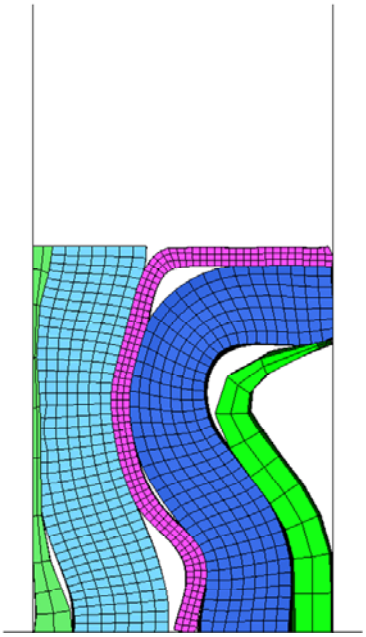

(i)

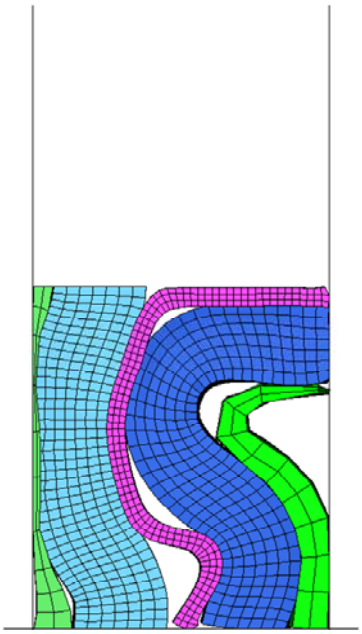

(j)

Figure 4.10. (a) The nominal stress-strain curve obtained from the finite element analysis of the module RVE specimen under quasi-static loading conditions along with the experimental results. (b)-(j) The deformed module RVE specimen from the finite element analysis at the nominal strains shown in (a).

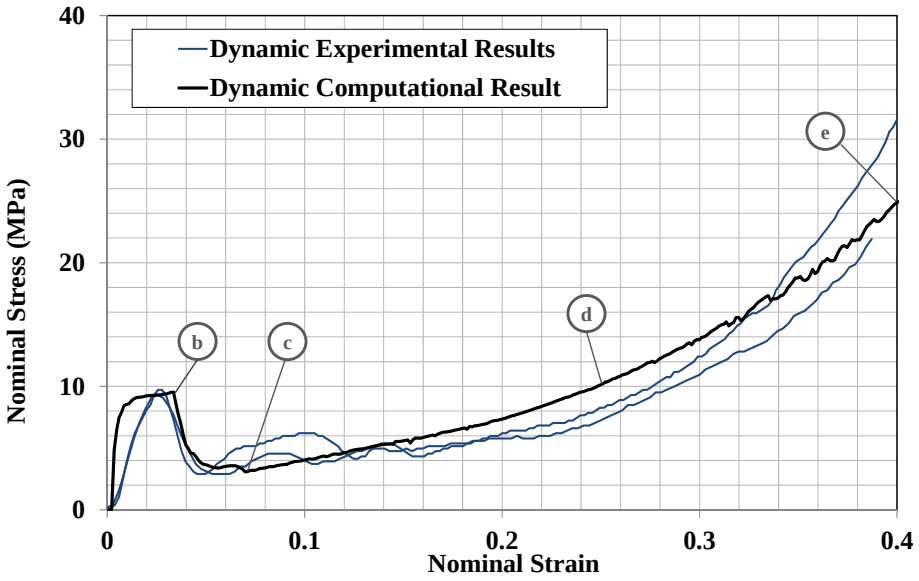
Dynamic Experimental Results
Dynamic Computational Result
Nominal Stress (MPa)
Nominal Strain
0
10
20
30
40
0
0.1
0.2
0.3
0.4
b
c
d
e

(a)

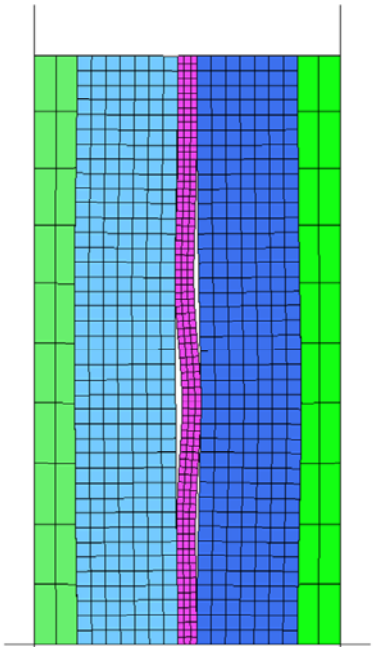

(b)

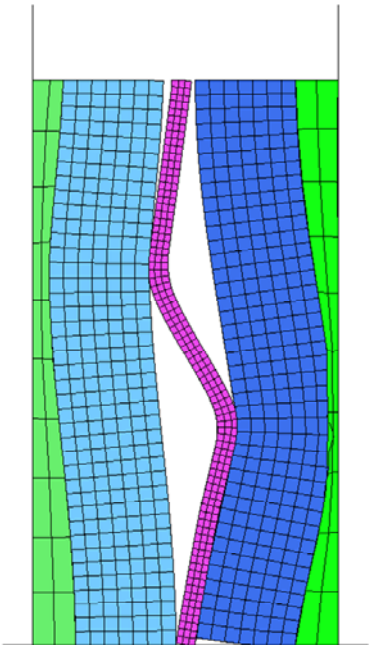

(c)

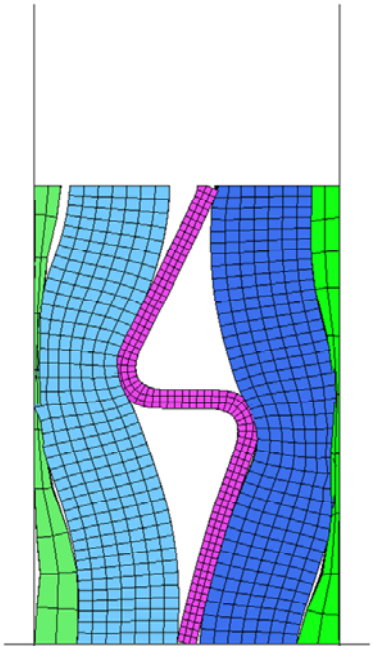

(d)

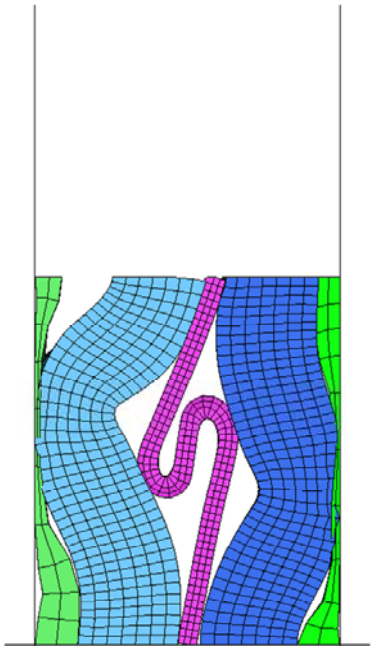

(e)

Figure 4.11. (a) The nominal stress-strain curve obtained from the finite element analysis of the module RVE specimen under dynamic loading conditions along with the experimental results. (b)-(j) The deformed module RVE specimen from the finite element analysis at the nominal strains shown in (a).

Chapter 5
Conclusions

The strengths and the fatigue lives of gas metal arc welded joints were investigated by many researchers. Investigators reported quasi-static and fatigue failure locations sometimes near the weld root and sometimes near the weld toe. In chapter 2, the failure modes of gas metal arc welds in single lap-shear specimens of high strength low alloy (HSLA) steel are investigated. Notched lap-shear specimens of HSLA steel sheets with a thickness of 2.0 mm were robot welded together using the gas metal arc welding process. Quasi-static test results showed two failure locations for the welds. The specimens cut from wide lap-shear specimens with shorter weld lengths failed near the weld root whereas the specimens cut from those with longer weld lengths failed near the weld toe. Scanning electron and optical microscope images of the failure surfaces and cross sections showed that the gas metal arc welds failed in a ductile necking/shear failure mode. Micro-hardness tests were conducted to provide an assessment of the mechanical properties of the base metal, the heat affected zone, and the weld metal. In order to understand the failure modes of short welds and long welds, two finite element models were developed. In these models, the size and shape of the heat affected zones were designed to match the micrographs of the cross sections for a 10 mm weld and a 40 mm weld. Three-dimensional finite element analyses were conducted with consideration

of micro void nucleation and growth. The distributions of the void volume fraction near the welds shown from the finite element analyses are consistent with the failure modes observed in the experimental results.

Further finite element analyses were conducted in order to understand the effects of the geometric characteristics of the heat affected zone on the load-displacement responses and the predicted failure locations of the lap-shear joints. The results showed that the heat affected zones and the weld metal, with higher effective stress-plastic strain curves, significantly affects the load-displacement response and the predicted failure locations of the lap-shear specimens. The results also showed that the geometric characteristics of the heat affected zone have negligible effect on the load-displacement results; however, the geometric characteristics of the heat affected zone are key factors for the resulting failure locations. Finally, finite element analyses were conducted in order to understand the effect of the weld geometry. A parametric study was conducted to give some insight on the effect of the weld metal penetration and the weld toe angle on the quasi-static strength of the lap-shear joints. The results indicate that the weld penetration and the weld toe angle have negligible effects on the load-displacement response and the predicted failure locations of the lap-shear specimens.

In chapter 3, the mode I and mode II stress intensity factor solutions for the pre-existing cracks near gas metal arc welds in lap-shear specimens are investigated. Analytical stress intensity factor solutions for the welds in lap-shear specimens with idealized weld geometries were derived based on the beam bending theory. Two-dimensional, plane strain finite element analyses were carried out in order to obtain the computational stress intensity factor solutions for the realistic and idealized weld

geometries. The normalized computational stress intensity factor solutions for the idealized weld geometry match the analytical solutions well. The finite element computations indicate that the stress intensity factor solutions for realistic gas metal arc welds are lower than the analytical solutions for the idealized weld geometry. Additional finite element analyses were carried out in order to obtain the computational stress intensity factor solutions for the realistic weld geometries with dissimilar sheet thicknesses. The results can be used for estimation of fatigue lives in a fatigue crack growth model under mixed mode loading conditions for gas metal arc welds with dissimilar sheet thicknesses. Finally, the stress intensity factor solutions for continuous welds and discontinuous welds were obtained by three-dimensional finite element analyses. The computational results indicate that the distributions of the mode I and mode II stress intensity factor solutions for the discontinuous weld are different from those for the continuous weld.

In chapter 4, a computational model is developed for simulations of representative volume element (RVE) specimens of lithium-ion battery modules under in-plane constrained compression tests. The model is based on the properties of the heat dissipater, the foam, and the macro behavior of the cells. This semi-homogenized computational model allows for computational efficiency with sacrifice of the detail buckling behavior of the battery cells. Since the model is based on the homogenized properties of each component, a modification to one of the components would not require additional testing of the other components in order to predict the overall behavior the module RVE specimen. The computational results from the model under quasi-static and dynamic loading conditions were compared to those from experiments. The results show

that the nominal stress-strain responses and the deformation patterns of the heat dissipater obtained from the semi-homogenized module model compare fairly well with experimental results.

An additional finite element analysis was performed which showed that the results of the model under quasi-static loading conditions are valid using the explicit solver. A further finite element analysis was performed in order to investigate whether the computational time of the model under dynamic loading conditions could be reduced further. The results indicate that the computational time can be decreased with a negligible change in the initial nominal buckling stress and deformation of the module RVE specimen however, after the nominal strain of 0.2 the kinetic energy of the module RVE specimen exceeded 5% of the internal energy. Lastly, a finite element analysis was performed in order to determine if the increase in the nominal stress at which buckling begins in the heat dissipater under the dynamic loading conditions is due to the different buckling modes observed in the results of the finite element analyses of the module RVE specimens under quasi-static loading conditions and under dynamic loading conditions. The results indicate that the increase in the initial nominal buckling stress under dynamic loading conditions is not due a difference in the buckling mode.